UNIVERSITÀ
DEGLI STUDI
DI PADOVA

UNIVERSITA' DEGLI STUDI DI PADOVA

Dipartimento di Ingegneria Industriale DII

Corso di Laurea Magistrale in Ingegneria dei Materiali

TRANSPARENT GLASSES OBTAINED BY UNCONVENTIONAL SINTERING

Relatore: Prof. Alessandro Martucci

Correlatori: Prof. Sylvie Le Floch

Dr. Elena Colusso

Laureanda: Benedetta Matani 2007048

Anno Accademico 2022/2023

TABLE OF CONTENTS

CHAPTER 1

Introduction

1.1.Origins and Glass Manufacturing Processes

Glass, with its transparency and incredible versatility, has consistently captured the human imagination throughout the centuries. For millennia, humanity has experimented with glass, transforming it from a simple natural curiosity into a fundamental material for technological innovation and human creative expression.

Thanks to its amorphous structure and its ability to assume complex shapes, glass has played a pivotal role in countless scientific discoveries and extraordinary works of art. Since ancient times, civilizations have honed their skills in glass production, highlighting remarkable technical mastery. The art of glass has contributed to the creation of timeless works and has furthered the progress of astronomy through the manufacture of telescopes. However, glass has not been confined to the realms of art and culture. Its transparency has made it indispensable for industrial and scientific applications. It has become, for example, the cornerstone for crafting precision laboratory instruments, revolutionizing how it is possible to explore the natural world and conduct scientific experiments.

Throughout ancient times, the most common glass production technique has been casting. This process demands strict attention to temperature, chemical composition, and controlled cooling to yield high-quality glass pieces with desired characteristics. The procedure involves preparing a mixture of raw materials, including silica sand, sodium carbonate, and calcium carbonate, followed by melting at temperatures exceeding 1300°C. At this temperature, the components meld to form a homogeneous liquid known as "molten glass"; this is then poured onto a ceramic surface, where it begins to gradually cool down. Controlled cooling is essential to avoid internal stresses in the glass, which could lead to fracture phenomena. After cutting and decorating, the produced glass is often subjected to tempering heat treatments to enhance its mechanical strength.

However, in an era where environmental sustainability and energy efficiency have become top global priorities, the production of transparent glass takes on fundamental significance. Therefore, alternative production techniques have been explored that, while reducing the temperature slightly, result in longer production times due to the diffusion mechanisms involved in liquid and solid-phase sintering. Energy efficiency remains a critical challenge; nonetheless, new sintering techniques developed in the last three decades are emerging.

1.2. Problem Statement

Unconventional sintering processes encompass approaches distinct from traditional solid and liquid sintering. In these processes, temperature is not the unique influential parameter for the diffusive phenomena leading to particle sintering and densification in the studied material. Some of these procedures introduce additional parameters such as pressure and electrical current, often in conjunction with liquid phases, which play a crucial role. The combination of these factors with temperature allows for densification at lower temperatures, making the process more environmentally friendly and sustainable in reducing the environmental impact.

Among the unconventional sintering processes, two stand out: cold sintering (CSP) and Spark Plasma Sintering (SPS). In the former case, sintering occurs at temperatures below 350°C, with the application of pressures on the order of magnitude of MPa and the use of a liquid phase to facilitate diffusion. In the latter case, pressure and electrical current, in addition to temperature, play a key role. Here, pressures can reach the order of GPa, while temperatures may exceed those used in cold sintering.

These processes, developed since the latter half of the last century, have primarily been applied to ceramic materials. The cold sintering process has been developed in specific modes, as reported in Tab. 1, which provides parameters used for sintering specific material powders. Note that the table only lists research outcomes for materials of significant relevance.

Table 1 Cold sintering parameters to produce corresponding materials.

Material	**Initial powder's dimensions**	**Chemical Structure**	**Liquid phase**	**P [MPa]**	**T [°C]**	**Dwell Time [min]**	**Relative density [%]**	**Reference**
ZnO	0,5 in	Wurtzite crystal structure	Acetic Acid 1M	387	126	60	>90%	*[1]*
BZCY72	Not evaluated	Different on base of composition initial powders	5% wt. deionized H_2O	400	350	5	>90% after calcination step	*[2]*
$BaTiO_3$	0,4 µm	perovskite structure	Suspension $Ba(OH)_2/TiO_2$	430	180	30	x	*[3]*
$(SiO_2)(Al2O_3)$ $(CaO)(Na_2O)$	Not evaluated	Amorphous structure	NaOH solution 40%w/w	250	250	20	95,20%	*[4]*
SiO_2	1,00 ± 0,34 µm	Amorphous structure	NaOH solution 2M	500	200	15	95%	*[5]*
SiO_2	0,15 µm	Amorphous structure	20 wt.% NaOH 5M	430	270	60	98%	*[6]*

The table highlights materials such as zinc oxide and barium titanate, along with unspecified specialized ceramics, obtained through cold sintering by applying both pressure and temperature to achieve the desired structure. An intriguing case pertains to silica: silicon oxide particles underwent cold sintering at temperatures below 270°C, with maximum pressures of 500MPa, employing a basic nature liquid phase. Various concentrations of the liquid phase and variable quantities of powder relative to the liquid phase were investigated. These experiments led to the creation of silica glass with relative densities remarkably close to 100%, achieving complete densification. The table not only demonstrates the diverse range of parameters influencing the cold sintering process but also emphasizes the significance of initial particle sizes. On the other hand, scientific literature reports that silica nanoparticles

have been subjected to cold sintering processes [*5,6*], as well as Ultra-High Sintering processes [*8*], but so far, the Spark Plasma Sintering process has not been investigated.

1.3 Experimental activity

The experimental goal is to produce glass with a low glass transition temperature (Tg) using these processes. Lower Tg enhances molecular mobility, improving alignment at lower temperatures and reducing defects. This results in more precise sintering and enhanced optical properties, crucial for achieving maximum glass transparency. The experimental work is based on a thorough analysis of scientific literature and prior research, which laid the groundwork for optimization and addressing unexpected conditions.

Various chemical synthesis methods were explored to create glass nanoparticles with a low glass transition temperature by incorporating oxides into the silica structure. The Stober synthesis served as a reference point, but notable alterations were made to incorporate the researched oxides into the silica network. Subsequently, comprehensive characterization of the resulting particles was undertaken to gain insights into their chemical composition, structure, size, and glass transition temperature.

Unconventional sintering methods, CSP and SPS, were developed for borosilicate glass particles at sub-micrometre scale. The primary objective was to achieve transparent glass, and the investigation involved the examination of process parameters, including liquid phase molarity and quantity, temperature, and dwell time in the mould.

A similar approach was adopted for silica nanoparticles, with initial characterization and the exploration of optimal treatment conditions for the Spark Plasma Process; in this case, the Spark Plasma process was conducted, at a fixed temperature to assess the impact of pressure on the sintering process. These experiments were personally conducted at the University of Lyon 1 (FR), in collaboration with the laboratories of CNRS, the French National Centre for Scientific Research.

In the forthcoming chapters, a comprehensive examination of each phase of the experimentation will be undertaken, with particular attention given to the materials involved: borosilicate glass, silica glass, and chemical synthesis. Each chapter will initiate with a concise introduction, followed by a thorough exposition of the experimental processes and an intricate analysis and interpretation of the characterization findings. The broad coverage of glass and unconventional sintering methodologies will establish a robust framework for gaining a comprehensive understanding of the developments and outcomes realized in this study.

CHAPTER 2

Glass: properties and manufacturing methods

This chapter aims to provide an overview of the material under study in the thesis and the processes through which it can be produced. The fundamental chemical, physical, and mechanical properties of glass will be presented comprehensively, with a particular emphasis on those essential to sintering processes, a production technique for glass that stands as a viable alternative to the traditional high-temperature fusion of silica or silica-based compounds. With the goal of achieving transparent glass, the analysis of properties, with a specific focus on transparency, will be followed by a description of the most significant experimental efforts that have led to the production of ceramic and/or glass material through sintering. The review of scientific literature will be conducted with attention to temperature as a key parameter, to which pressure, a fundamental parameter for non-conventional sintering processes, will be added.

2.1 Glass: structural, mechanical, and optical properties

Glass is an amorphous, non-crystalline material obtained through the rapid cooling of a melt composed primarily of silica (SiO_2) along with other components such as sodium (Na_2O), calcium (CaO), aluminium (Al_2O_3), and other oxides, which impart unique physical and chemical properties to glass. It is a material that exhibits the glass transition phenomenon, and the corresponding physical state is referred to as the "glassy state."

Its amorphous structure, lacking long-range periodicity, is one of the primary distinguishing features of glass, setting it apart from crystalline materials and influencing its mechanical, thermal, and optical properties.

2.1.1 Glass transition phenomenon

In the case of a crystal, the molar volume undergoes a sudden change at the crystallization temperature, known as Tc. However, in the case of glass, as the temperature of the liquid decreases, it transitions into a metastable state known as a supercooled liquid, and

thermodynamic equilibrium is no longer present. Instead, there is a gradual transition from the supercooled liquid to the vitreous state, a process known as the glass transition of glass.

As the temperature decreases, the supercooled liquid becomes increasingly viscous, and atomic rearrangements occur with progressively longer relaxation times. Unlike a crystal, the change in molar volume between the two states occurs continuously over a specific temperature range. The glass transformation range is defined as the temperature range over which a melt becomes a rigid solid (glass) upon cooling; it's expressed as "range" because cooling rate will affect the temperature at which a melt becomes a glass and so cooling rate will affect macroscopic glass properties. As Fig. 1 shows, from a practical standpoint, the glass transition temperature, denoted as Tg, is defined as the point where the properties of the liquid and glass intersect in the extrapolation.

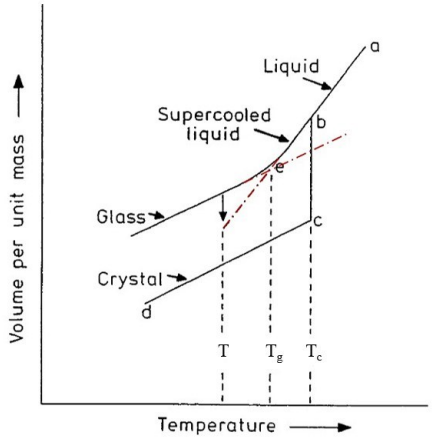

Figure 1 Thermal variations of specific volume during the transition from the liquid state to the solid state (glassy or crystalline). [8]

Fig. 2 shows that the glass transition temperature is influenced by the cooling rate.

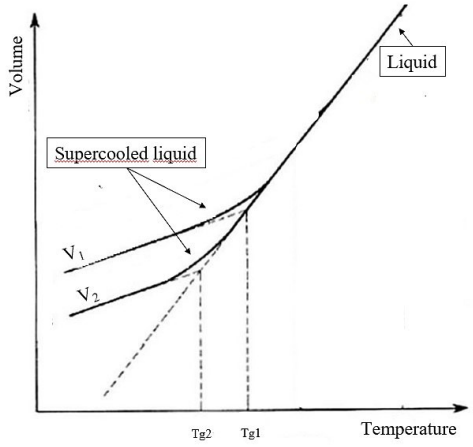

Figure 2 Influence of cooling rate on the glass transition temperature [9]

If the supercooled liquid is cooled at a faster rate v_1 compared to v_2, the glass transition temperature will be higher (T_{g1}). Conversely, if cooling occurs more slowly, atomic rearrangements have time to occur, leading to a frozen structure at a lower temperature, T_{g2}, compared to T_{g1}. The range of all possible transformation temperatures obtainable by varying the $v_{cooling}$ of the liquid and associated with a particular composition is called "*transformation range*" of the glass; Equation (1) describes the relationship between the glass transition temperature (Tg) and the cooling rate (v).

$$v = v_0 \exp\left(-\frac{E_a}{RT_g}\right) \qquad (1)$$

where E_a represents the activation energy required for the phenomenon, and T_g is the glass transition temperature.

Furthermore, it is observed that the molar volume of glass is larger than that of a crystal, resulting in a lower density for glass. In summary, glass cooled rapidly will have a higher glass transition temperature and therefore a larger molar volume, resulting in a less dense structure.

2.1.2 Structural characteristics

The glass structure is based on the Zachariasen model [*10*], which is based on the concept of a continuous random network of SiO_4 tetrahedral elementary units for pure silica, interconnected through the Si-O-Si bond (Fig. 3).

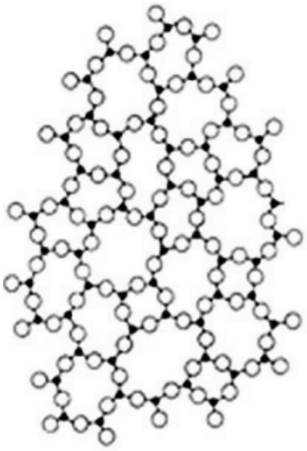

Figure 3 Three-dimensional random network of silica glass. [11]

It can be experimentally determined through the interaction of a beam with the material, using techniques such as light scattering, X-ray diffraction, or neutron scattering. As Fig. 4 illustrates, the structure of an amorphous pure silica glass consists of randomly oriented SiO_4 tetrahedra, linked to an oxygen atom through one of their vertices.

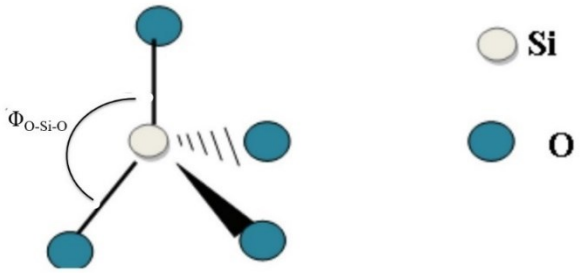

Figure 4 The basic building block of pure silica glass: the SiO4 tetrahedron [12]

Being an amorphous material, pure silica glass exhibits "short-range order," which is characterized by the following parameters: the distance between the silicon and oxygen

atoms, denoted as R_{ij}, and the bond angle, denoted as Φ_{jik}. For silica, these values are as follows:

- R_{Si-O} = 1.62 Ångström (Å), which can be evaluated through X-ray diffraction measurements.
- Φ_{O-Si-O} = 109.7°.

However, due to the random nature of Si-O-Si tetrahedra orientation, the angles θ between tetrahedra can fluctuate between 120° and 180°, with the most probable value being around 144°; Fig. 5 illustrates the inter-tetrahedral connection and better clarifies what angle θ refers to.

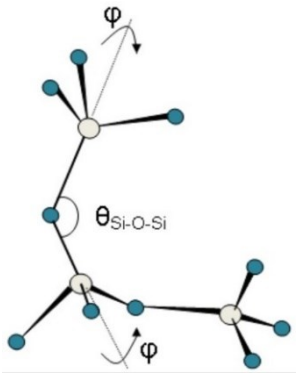

Figure 5 The connection between tetrahedra in silica is defined by the inter-tetrahedral angle $\theta_{Si-O-Si}$ and the dihedral angle φ [13]

This intra-tetrahedral angle represents an average that considers angles within isolated tetrahedra and angles between tetrahedra within a cycle. This angle strongly depends on both the number of tetrahedra enclosed within the cycle and the flexibility of the tetrahedra since not all tetrahedra are planar.

The concept of "short-range order" implies that the distance between the central atom "i" and nearby atoms of the same species remains constant. In the case of a glass, this short-range order is preserved, contributing to the understanding of the atomic structure of these materials.

As mentioned earlier, it is possible to introduce oxides into the glass lattice. They are a class of transparent materials that hold significant relevance in engineering and industrial applications. These glasses are renowned for their purity, characterized by the absence of impurities, and their distinctive chemical properties. They exhibit high resistance to corrosion from chemical agents, with exceptions being hydrofluoric acid (HF) and certain bases. Additionally, owing to their low coefficient of thermal expansion, these materials serve as efficient thermal and electrical insulators.

Understanding the chemical composition of oxide glasses is crucial to comprehend their properties. The oxides present in these glasses can be categorized into three primary groups based on their function within the glass structure: forming oxides, modifying oxides, and intermediate oxides. Forming oxides constitute the three-dimensional network of the glass, contributing to the creation of an amorphous structure through cooling and solidification of the molten material. The predominant forming oxide is silica (SiO_2), with other forming oxides including GeO_2, B_2O_3, As_2O_3, and TeO_2. In a glass composed exclusively of forming oxides, every oxygen atom acts as a bridge between oxide atoms. It is important to note that the presence of oxides such as B_2O_3, which will be the subject of study in this research, affects the glass's glass transition temperature (T_g) due to its intrinsic properties. Fig. 6 clearly shows a glassy lattice of borosilicate glass; it distinctly reveals the formation of a well-structured glass characterized by the presence of Si-O-B bonds.

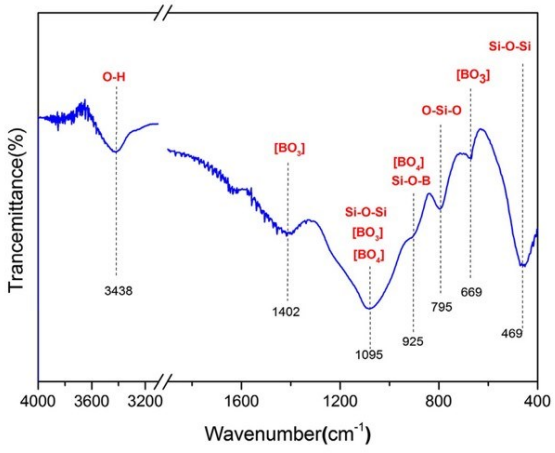

Figure 4 Borosilicate structure: its FT-IR spectrum [14]

Modifying oxides, including alkali oxides (Li_2O, Na_2O, K_2O, Cs_2O) and alkaline-earth oxides (MgO, CaO, BaO), introduce variations in the glass structure. These oxides cause the disruption of Si-O-Si bonds within the silica network, leading to the formation of non-bridging oxygen atoms. Consequently, the glass structure becomes less viscous, T_g decreases, and the coefficient of thermal expansion increases compared to pure silica glass.

Intermediate oxides, on the other hand, can function as forming or modifier oxides in certain scenarios; common examples of modifying oxides include Al_2O_3, Fe_2O_3, ZnO, TiO_2, and ZrO_2.

Below, in Fig. 7, an example is provided of how the glass structure is altered following the addition of an oxide, in this case, sodium oxide, being a modifying oxide that disrupts the bonds between oxygen and silica, resulting in an open structure and altering that kind of structural "regularity".

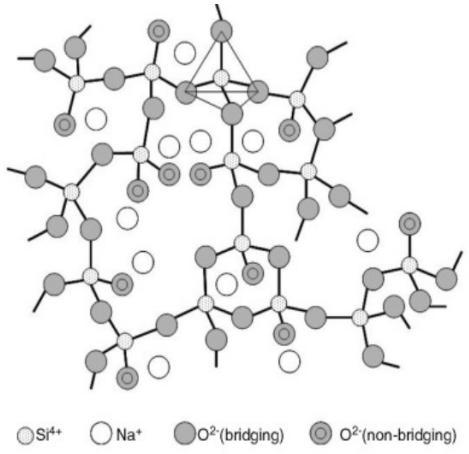

Figure 7 Structure of alkali-silicate glasses [15]

2.1.3 Glass mechanics: elastic-plastic properties

Glassy materials, despite their inherent brittleness, can undergo plastic deformation under conditions of high stress, such as high hydrostatic pressures or through processes like indentation [*16*]. Within this plastic deformation, two distinct mechanisms come into play:

one that conserves volume, known as shear flow, and another that results in permanent densification [*17*]. This densification can vary significantly based on the atomic packing density of the starting material, i.e., the amount of empty space between atoms [*18*]. Studies conducted by Greaves and colleagues have demonstrated that the Poisson's ratio of an amorphous material (which is related to its atomic packing density) serves as an excellent indicator of its capacity for permanent densification [*19*]. In contrast, strong oxide glasses such as amorphous GeO_2 or amorphous SiO_2, with their open, tetrahedrally connected networks, can undergo significant densification, up to 15% and 21%, respectively.

For fused silica, it's worth noting that the elastic yield under hydrostatic pressure at room temperature is approximately 9 GPa [*20*]. Below this elastic yield, any deformation is entirely reversible. However, beyond 9 GPa, permanent structural changes occur, and the treated sample undergoes densification. This densification process is gradual and continues until it reaches a saturation pressure of 25 GPa, where it stops, with a maximum densification level of 21%. Importantly, both the elastic yield and saturation pressure can be reduced if the sample is heated during compression or if shear stresses are applied [*21*].

Furthermore, between these two pressure thresholds (which determine the onset of densification and its saturation), the densification ratio steadily increases [*21*]. However, despite numerous experimental and simulation studies on amorphous SiO_2 under high pressures [*22*], the structural alterations and elastic properties of mildly densified glasses are not yet fully understood. This knowledge gap presents a limitation in modelling plastic deformation.

2.1.3.1 Permanent densification phenomenon in compression

Plastic deformation in glasses manifests as a densification phenomenon. There are various pathways to reach the irreversible deformation zone. Initially, the application of hydrostatic compression through a diamond anvil cell [*23*] results in irreversible structural changes in glasses. The structural origins of this densification process are still the subject of active

research [*24, 25, 26*]. Studies using a diamond anvil cell have enabled the characterization of the densification phenomenon and structural changes in silica glass under high hydrostatic pressure in-situ [*27, 28*]. As highlighted in Tab. 1, the authors observed a progressive Increase in elastic moduli and densification ratio; in the table, please consider that the compression process was conducted at the ambient temperature (Tamb) with a holding period of 24 hours at the maximum pressure (Pmax).

Table 2 Maximum pressure reached in the DAC and densification ratio [28]

Pmax (Gpa)	**0**	**9,8**	**12,0**	**13,6**	**14,6**	**15,5**	**18,1**	**26,2**
Δρ/ρ (%)	0	1.4	4.4	8.6	11.7	14.3	19.1	21.0
Elastic moduli								
L (Gpa)	77.3	77.3	78.4	85.6	92.2	102.8	123.2	132.2
G (Gpa)	30.4	30.4	30.7	32.8	34.8	38.0	44.0	46.7
K (Gpa)	36.8	36.8	37.5	41.8	45.8	52.1	64.5	69.9
E (Gpa)	71.5	71.5	72.4	78.1	83.3	91.7	107.6	114.6
ν	0,176	0,176	0,178	0,188	0,197	0,207	0,222	0,227

Fig. 8 also illustrates the correlation between elastic modulus and densification ratio that the authors have identified; in the picture full black circles are the data calculated from Brillouin scattering results and the black line represents a polynomial fit.

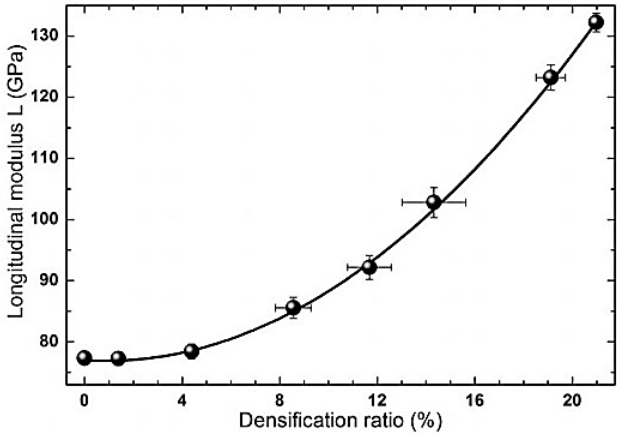

Figure 8 Longitudinal modulus of silica glass as a function of densification ratio

Shockwaves, furthermore, allow for the densification of glasses [*29*]. Finally, various types of irradiations, such as pulsed IR laser irradiation [*30*], induce plastic deformation in glasses. It has been observed that silica glass can achieve an irreversible densification rate of approximately 21% [*31, 32*]. Brillouin light scattering studies conducted by *Grimsdith et al.* have demonstrated that silica glass undergoes irreversible structural changes during compression up to 16 GPa [*33*]. This irreversible deformation begins around 7-10 GPa, as indicated by the authors, and stabilizes at 20% densification around 25 GPa at room temperature [*34*]. This phenomenon has also been successfully simulated [*35*]. Experiments have shown a correlation between indentation and densification in silica. *Neely and Mackenzie* [*36*] were the first to propose this densification phenomenon, and *Peter et al.* [37] emphasized that this phenomenon is also present in silicate glasses. The ability of oxide glasses to permanently deform through Vickers indentation has been confirmed by *Arora et al* [*38*].

In summary, the elastoplastic behaviour of silicates and glasses in general remains poorly understood. Despite being commonly regarded as essentially brittle materials at the macroscopic level, it has been demonstrated that they undergo plastic deformations at the microscopic scale. The analysis of glass behaviour under high pressures is essential in the context of this thesis to compare the above findings with what occurs for nanostructured silica glass. Silica, which is a fundamental subject in materials science research, may not

exhibit the same properties when considered as bulk glass or in nanostructured form, as the size scale can significantly influence material properties.

In the upcoming chapters, particularly in Chapter 4 of this research, the results will be examined when nanoscale silica is subjected to high pressures using a diamond anvil cell. The conclusions drawn will allow for a comparison between the developments presented here and the discussion regarding silica glass.

2.1.4 Optical properties

In the realm of glass, a diverse range of optical properties unfolds, each meticulously governed by well-defined physical laws. The comprehension of these optical attributes and their inherent principles assumes an indisputable significance in the comprehensive analysis of glass. This comprehension bears paramount importance across multiple domains, spanning materials science, architecture, the optical industry, and electronics. Within this section, an in-depth exploration of the pivotal optical properties of glass will be systematically conducted, elucidating the fundamental laws orchestrating their behaviour. Additionally, strategic incorporation of illustrative images will be proposed to enhance the clarity and comprehensibility of these optical phenomena.

Refractivity is a fundamental attribute of glass, regulated by Snell's Law, also known as the Law of Refraction. Snell's Law stipulates that when a light ray transitions between different media, its change in direction is contingent upon the respective refractive indices of the media involved. This fundamental relationship can be expressed as Equation (2):

$$n_1 \sin(\theta_1) = n_2 \sin(\theta_2) \qquad (2)$$

where n_1 and n_2 are the refractive indices of the two media, while θ_1 and θ_2 represent the angles of incidence and refraction, respectively. The image in Fig. 9 visually represents refraction, where light changes direction when transitioning from air to glass with different refractive indices, following Snell's law.

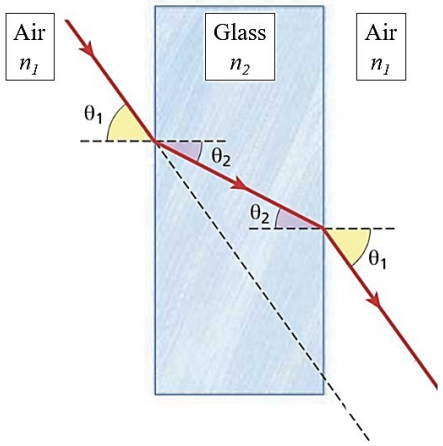

Figure 9 Representation of the refraction phenomenon [39]

Furthermore, it's important to mention the phenomenon of total internal reflection that can occur when the angle of incidence is greater than the critical angle, which typically happens in glass at an angle of around 42 degrees. Total internal reflection is a fascinating optical phenomenon, especially relevant in applications like optical fibres and prisms, where light is completely reflected within the glass medium, without any transmission.

Dispersion within glass, responsible for decomposing white light into its constituent colours, arises due to variations in refractive index with respect to wavelength. This optical behaviour adheres to Cauchy's Law of Dispersion (Equation 2.3), a mathematical expression that relates the refractive index n to the wavelength λ of light:

$$n(\lambda) = A + \frac{B}{\lambda^2} + \frac{C}{x^4} + \cdots \qquad (3)$$

where *A, B, C* and so forth represent material-specific coefficients.

Fig. 10 illustrates the described phenomenon.

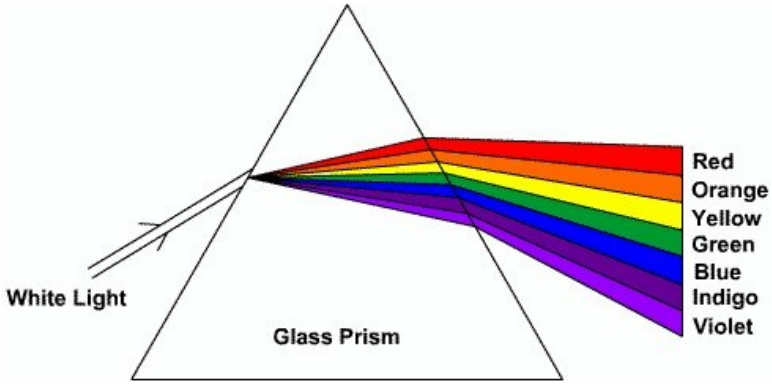

Figure 10 Representation of the dispersion phenomenon [40]

The reflection of light upon the surface of glass complies with Fresnel's Law of Reflection. This fundamental principle dictates that the angle of incidence equals the angle of reflection, with the angle of transmission determined through the application of Snell's Law. The intensity of reflection is also contingent upon the angle of incidence and the refractive indices of the media involved. The surface of the glass exhibits a certain reflectivity R, which, in the case of vertical incidence, can be measured using Equation 4:

$$R = \left(\frac{n-1}{n+1}\right)^2 \qquad (4)$$

It holds true for Equation 5:

$$I_R = RI_0 \qquad (5)$$

where I_0 is the intensity of incident light, I_R is the intensity of reflected light, and R is the reflectivity.

Birefringence, a distinctive optical property of certain types of glass, involves the variation of light speed with polarization direction. The governing principles underlying birefringence are encapsulated within Maxwell's equations, which intricately describe the behaviour of light within anisotropic mediums, such as birefringent glass.

2.1.4.1 Transparency

In general, there are four ways in which light can interact with a solid material, and these four modes, including reflection, are illustrated in Fig. 11.

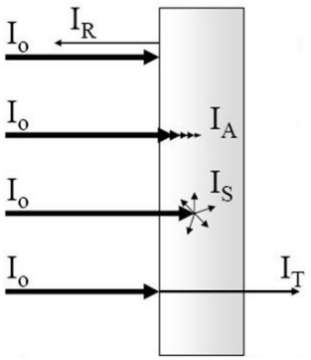

Figure 11 Optical properties of solids [41]

Light can be reflected from the surface of the solid (Reflection); a portion of it can be absorbed within the solid (Absorption) through the coupling process, it can be transmitted through the solid (Transmission), or it can be scattered by the atoms and defects within the solid (Scattering). To comprehend the behaviour of an incident light ray with intensity I_0 entering the material, it's possible to refer to Equation 6:

$$I_0 = I_R + I_A + I_S + I_T \qquad (6)$$

In this equation, the intensity of light represents the number of photons passing through a cross-sectional area of the material per unit of time.

The phenomenon of material transparency is closely related to the above. A material will be transparent if it satisfies the following conditions:

- It does not absorb light in the visible range, meaning it does not contain elements with electronic energy transition wavelengths in the visible spectrum.
- It must be homogeneous: if conditions are those illustrated in Fig. 12, the material has interfaces between different regions (with different refractive indices, n) or

impurities, multiple refraction and absorption phenomena will occur, rendering the material opaque.

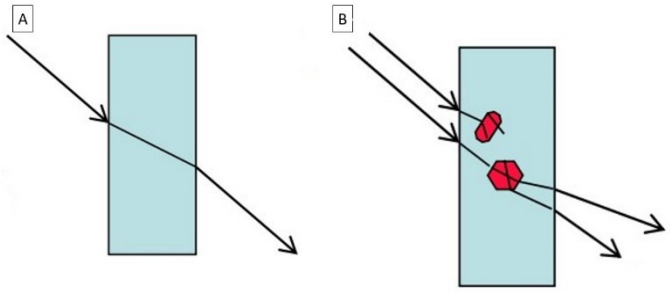

Figure 12 Type material's effect on transparency: (A)Homogeneous and transparent material; (B) Non-homogeneous material with multiple refractions [42]

The regions within the material where there are variations in refractive index, leading to refraction, can originate from sources such as crystals incorporated into the glass structure or the presence of small voids like bubbles or porosity. To enable electromagnetic radiation to perceive that it's traversing a material with distinct refractive indices (n), it's crucial that the dimensions of these distinct regions are comparable to the wavelength of the incident radiation.

- The material must not completely reflect the incident radiation to be considered transparent.

Glass transparency, for instance, is guaranteed for very small constituent structures, less than 300 nm in size; visible light, in fact, covers wavelengths between 380 and 750 nm.

2.2 Obtaining ceramics by sintering

Sintering of ceramic materials is a topic of significant interest in the field of Materials Engineering. Ceramic materials are solid substances primarily characterized by ionic and covalent bonds, composed mainly of metallic atoms. These materials are known for their excellent mechanical properties, thermal stability, and chemical resistance. One of the main similarities between ceramic materials and glass lies in their amorphous atomic structure.

However, the fundamental differences between the two lies in crystallinity, with ceramic materials exhibiting a well-defined crystalline structure compared to glass.

Sintering, both in solid and liquid forms, is a crucial process in the production of ceramic materials. These processes enable the production of compact ceramic materials, reducing the process temperature compared to the traditional sand melting of silica compounds. However, it should be noted that these processes require heat treatments, which can lead to prolonged times required to achieve particle densification.

In recent decades, scientific research has focused on developing more sustainable sintering techniques with the aim of reducing environmental impact, energy requirements, process temperatures, and costs associated with traditional sintering methods. These new techniques, known as "non-conventional sintering techniques," include cold sintering, Spark Plasma Sintering, and Flash sintering. These advancements aim to promote the formation of interparticle bonds and the densification of ceramic powder compacts in a more efficient and cost-effective manner.

2.2.1 Influence of temperature

Temperature in sintering processes is paramount and plays a pivotal role. The increase in temperature can significantly impact the properties of the resulting material. As the temperature rises, powder particles begin to heat up, and at elevated temperatures, they may partially or fully melt. This fusion phase allows the powder particles to agglomerate and compact, leading to the formation of a solid material. The temperature increase provides the particles with an excess of energy, enabling them to move and diffuse at the atomic level. This phenomenon facilitates particle migration and their fusion, contributing to the creation of a denser and more compact material.

It is important to note that the application of high temperatures in powder material sintering is an essential practice to achieve effective results. The specific temperature required varies depending on the starting material and the desired characteristics of the final product. The

use of high temperatures can significantly enhance the mechanical properties of the sintered material, such as strength and hardness, thanks to the increased density of the resulting material and the reduction of porosity.

High temperature plays a crucial role in sintering processes, both in the solid and liquid states, analysed in the following paragraphs.

2.2.1.1. Solid sintering

Solid-state sintering is a process that involves the melting and compaction of material particles by applying heat at temperatures below the material's melting point. During this process, there is a reduction in the surface area of the compacted material, typically accompanied by an increase in its density. However, it is important to note that in some cases, the compacted material may reduce its surface area and increase its cohesion without a significant increase in density.

Sintering is usually divided into three distinctive phases: the initial phase, the intermediate phase, and the final phase. These phases represent transitions in the material's microstructure during the sintering process. In each of these phases, there is a well-defined change in the shape of the pores present in the material, and pore contraction occurs while maintaining a nearly constant shape.

A clear explanation of the initial phase can be provided using the model known as the "two-sphere model" (see Fig. 13).

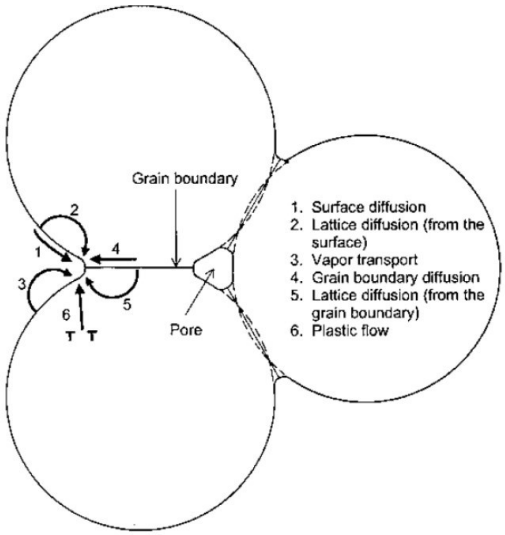

Figure 13 Two-particle model for initial-stage sintering [43]

During sintering, the transport of matter occurs from regions with a high chemical potential to regions with a lower chemical potential. In the context of this model, the areas with high chemical potential are located at the contact region between the particles (also known as the grain boundary) and along the convex surface of each particle. In contrast, the concave region between the particles has a lower chemical potential compared to these areas. Matter can move from the convex surface toward the neck region in several ways, including evaporation from the convex surface and condensation on the concave surface through the gas phase, surface diffusion from the convex surface to the concave surface, lattice diffusion from the convex surface or grain boundary, or diffusion through the grain boundary itself. When the source of matter is the grain boundary, densification occurs as the centres of the two particles approach each other during the sintering process. On the other hand, when the source of matter is the convex surfaces of the particles themselves, the particles undergo a shape change without their centres approaching each other (this phenomenon is known as "coarsening"). The driving force that guides the transport of matter during sintering is the difference in concentration between the source of matter (i.e., the particle's surface or the grain boundary) and the point where matter accumulates (the neck region). These concentrations differ due to variations in chemical potential resulting from curvature differences [*44*]. This concentration difference induces the transport of matter from the grain boundary region to the neck region

through grain boundary diffusion and lattice diffusion. In this situation, densification of the compacted material is observed because the difference in vapor pressure tends to push matter through the gas phase toward the neck region.

During the intermediate phase of the sintering process, there is a progressive narrowing of the pore channels' diameter until the geometry becomes susceptible to surface fluctuations, a phenomenon known as "Rayleigh instability." While pore channels can narrow through surface diffusion, the transport path length becomes significantly extended. Therefore, the narrowing process is predominantly influenced by lattice diffusion or diffusion through the grain boundary [*45*].

During the final phase of the sintering process, the desired properties are achieved in the compacted material. In this phase, the pores, once they have narrowed to the point of instability, fragment into small, isolated pores located at grain junctions. The driving force responsible for pore narrowing is the difference in concentration between the atoms on the curved surfaces of the pores themselves and those located along the grain boundaries. The pore narrowing process is primarily governed by diffusion occurring through the grain boundary and lattice diffusion.

It's important to note that one of the key concepts within the theory of sintering argues that reducing particle size leads to an increase in the sintering rate. Numerous experiments have confirmed this correlation between sintering rate and particle size.[*46*] This relationship results from both an increase in the driving force (through changes in curvature) and kinetics (through variations in path length) of the particles. For smaller-sized particles, it is possible to achieve equivalent density in a shorter period at lower sintering temperatures compared to what is required for larger-sized particles at higher temperatures. A schematic example of how sintering temperature varies to achieve the same relative density in response to a change in particle size is illustrated in Fig. 14.

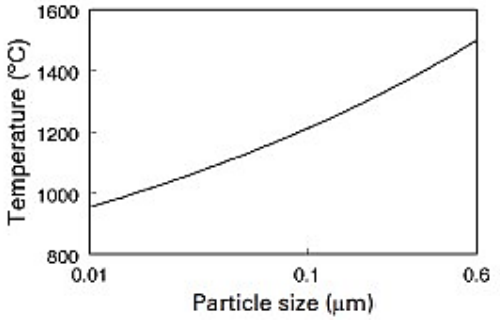

Figure 14 Effect of particle size on the temperature necessary to achieve a given density in a specific time.

Specifically, for a sintering process controlled by diffusion through the grain boundary, reducing particle size from 0.6 μm to 0.01 μm results in a significant reduction in the sintering temperature, by over 500°C. This reduction in particle size, therefore, allows for more efficient sintering at lower temperatures.

2.2.1.2 Liquid sintering

Liquid Phase Sintering (LPS) is a process employed in the production of high-performance multiphase components from powders. This procedure involves sintering under conditions where solid grains coexist with a liquid phase that wets these solids.

Liquid-phase sintering is a process composed of three main phases, as illustrated in Fig. 15, that relate the volumetric contraction associated with densification and time.

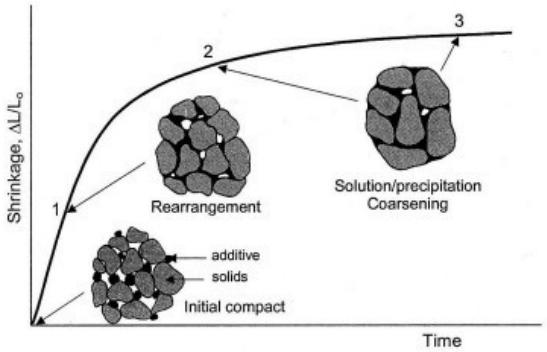

Figure 15 LPS process explained on the base of shrinkage in function of time [47]

The liquid phase allows for the redistribution of particles, which are typically soluble in the liquid. This condition enables the liquid to wet the solid material, generating capillary forces. Elevated temperatures make the particles more malleable, facilitating the solution-precipitation process, known as the flattening contact and pore filling phenomenon associated with densification. In the third and final phase, the "coarsening" phenomenon (Ostwald ripening phenomenon) occurs, during which particle coalescence or grain growth takes place, leading to the densification of the material. It's important to consider that the temperature increase also promotes interaction between the various compositions of the mixed particles, as there is diffusion driven by liquid composition gradients between the particles. This interaction can significantly influence the liquid-phase sintering process, adding to its complexity, and impacting the final properties of the material obtained.

In the process of liquid-phase sintering, several key phases occur that influence the microstructure and properties of the resulting material. When the liquid phase forms within LPS, the system's microstructure comprises solid, liquid, and vapor phases. During this process, the diffusion of the liquid on the solid replaces solid-vapor interfaces with liquid-solid and liquid-vapor interfaces.

A crucial aspect is the contact angle (θ) between the solid and the liquid, which plays a decisive role in particle interactions. This contact angle is influenced by the solubility of solid particles in the liquid and the chemical characteristics of the surfaces, as explained by Equation 7, where γ is the interfacial energy and *S, L, V* represent solid, liquid and vapour.

$$\gamma_{SV} = \gamma_{SL} + \gamma_{LV} cos\vartheta \qquad (7)$$

For instance, if the ratio of solid-solid surface energy to solid-liquid surface energy is high (>1.8), the contact angle tends to approach 0°, allowing the liquid to effectively separate the contacting grains. In Fig. 16 [*48*] a comparison is shown between effective and ineffective wetting, evaluated based on the contact angle between the involved phases; it explains that densification requires a low-contact angle to ensure that particles are pulled together.

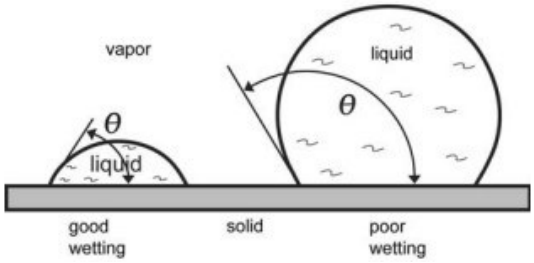

Figure 16 Contrast of a wetting behaviour for a liquid on a horizontal plane

However, in amorphous materials where grain boundaries do not exist, particles will fuse since there is no resistance to contact.

Initially, pores may be present as voids between particles or result from the uneven packing of the particles themselves. Capillarity drives the liquid to preferentially fill smaller pores. As these smaller pores saturate, the average pore size increases, while the overall porosity and the number of pores decrease. However, pores larger than the solid grains are more challenging to eliminate and, in some cases, can even cause material swelling due to pore formation at the previous particle sites during heating.

The presence of a liquid that wets the particles is responsible for establishing contact between them due to capillary attraction. In the case of amorphous particles, they tend to fuse because there are no grain boundaries to hinder this process [*49*]. Regarding crystalline solids, there is a 5-10% chance that, randomly, contact between grains with a low-angle grain boundary may occur, facilitating fusion. The curvature of the grain boundary plays a crucial role as a driving force in the grain fusion process, contributing to densification and coarsening, which is the process of grain growth [*50*]. As illustrated in Figure 17 [*51*], there are four possible transport mechanisms in this phase: (1) grain boundary migration through solid-state diffusion, (2) grain boundary migration through diffusion across a thin liquid layer on the boundary, (3) solution-precipitation from smaller to larger adjacent grains, and (4) grain rotation in a coincidence condition.

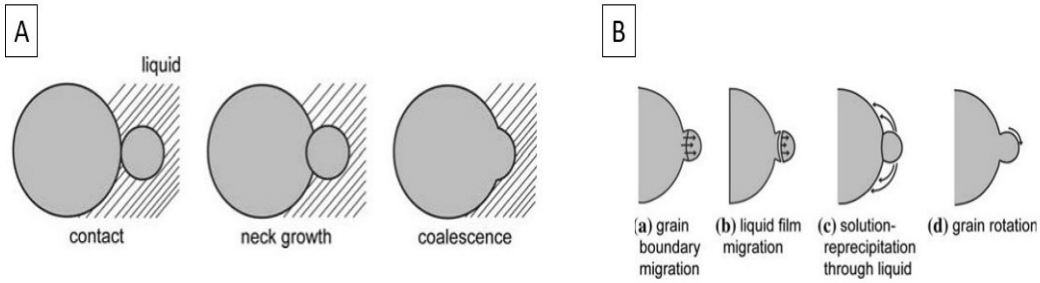

Figure 17 Coalescence mechanism: (A) different grain size necessity; (B) steps

Experiments have confirmed grain boundary migration with a thin liquid layer, while grain rotation is favoured by high liquid contents as there are fewer bonds to hinder it. With high solid contents, grain boundary migration represents the predominant mechanism. As smaller-sized grains are incorporated, the fusion process decreases.

Chemical reactions, diffusional homogenization, and solid-state sintering are events that occur during the heating cycle. Slower heating may incur a higher cost but contributes to greater impurity removal, although it can simultaneously produce a coarser microstructure. In the transient phase of LPS, heating rate shows a notable influence [*52*]. Slow heating favours pore formation in reactive and transient liquid systems. In other variations of LPS, heating rate has a lesser impact since most densification and microstructure formation occur after the appearance of the liquid phase. Densification, however, is not sensitive to cooling rate. However, during cooling, the liquid undergoes a contraction like what is observed in castings, which can lead to the formation of shrinkage pores within the liquid. Additionally, solid may precipitate from the solution during cooling.

2.3 Influence of isostatic pressure: new ways of producing glass

In its most general form, a conventional ceramic material production process can be summarized through a process flowchart depicted in Fig. 18. This flowchart not only

outlines the various processing stages involved but also underscores that the sintering stage is the one requiring the most energy.

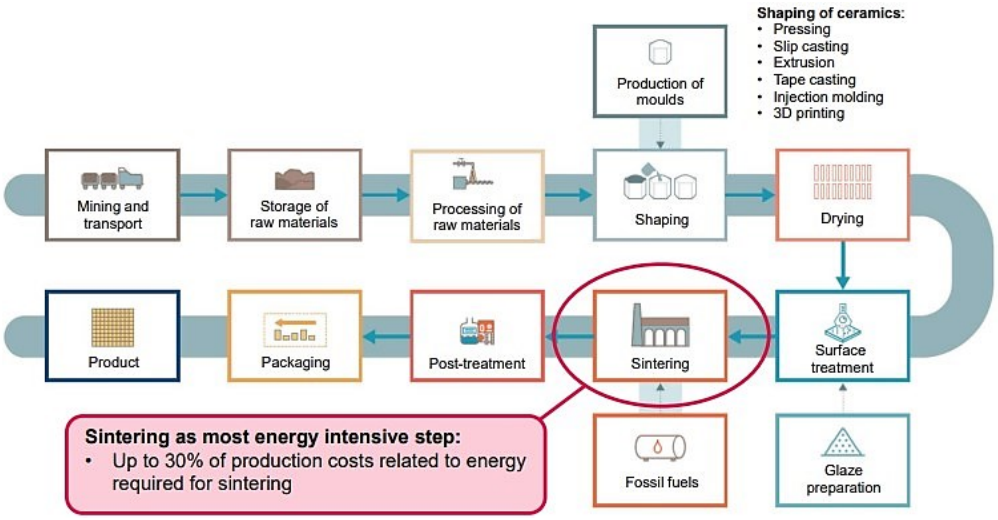

Figure 185 Conventional processes of ceramic materials [53]

This, in turn, is closely related to the energy costs associated with such a process. The significant energy consumption, as discussed in the preceding paragraphs, is often due to the use of very high temperatures, which constitute a key element in traditional sintering processes.

In order to mitigate the impact of high temperatures, new techniques have been developed, giving rise to what is termed "unconventional sintering techniques." This term refers to all processes that produce ceramic materials through sintering without relying solely on temperature as the primary parameter. Instead, they introduce new parameters such as pressure, electric field, and electric current, both in the presence and absence of a liquid phase.

An explanatory diagram of the above is presented in Fig. 19.

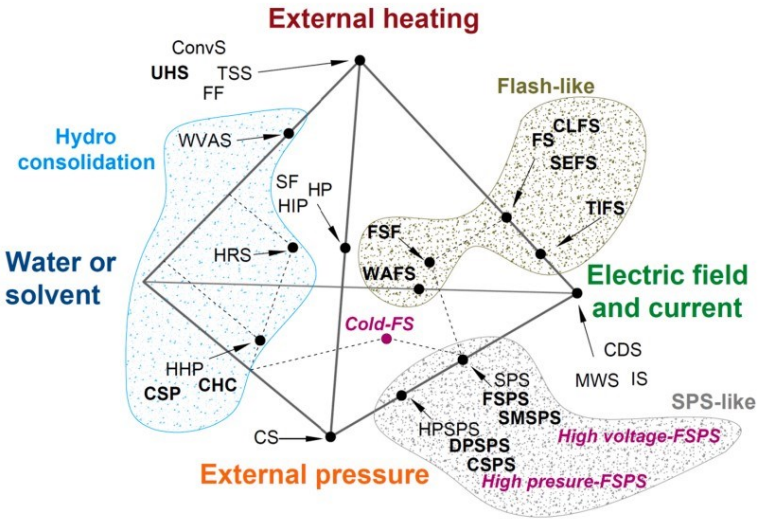

Figure 19 Quaternary diagram of sintering [54]

The "*Quaternary diagram of sintering*" represents an essential tool for evaluating the newly developed processes, based on the four vertices of the pyramid constituting the diagram: liquid phase, external pressure, electric current, and temperature. As one moves away from each vertex, the influence of the represented parameter on that vertex within the process diminishes. Processes that fall within the common spaces between the vertices are characterized by a combination of these parameters.

In the quaternary diagram, it is evident that in Cold Sintering Process (CSP), the liquid phase and external pressure play a fundamental role, while the effect of external temperature is considered of lesser importance. In the case of Spark Plasma Sintering (SPS), a combined action of electric field and external pressure is anticipated, with temperature not playing as crucial a role. Finally, the Flash Sintering (FS) process is strongly influenced by temperature but also by electric current, while external pressure does not have a significant role.

Unconventional sintering techniques such as CSP, FS, and SPS will now be explored in terms of theoretical process analysis, execution modes, and key research findings. This exploration will provide a solid foundation for understanding the experimentation presented in this thesis.

2.3.1 Cold sintering process

The term "Cold Sintering Process" denotes a highly energy-efficient sintering technique [*55*]. In this methodology, powder, mixed with a solvent, is subjected to significant pressures in the range of hundreds of megapascals while being simultaneously heated, without exceeding 300°C [55,*56,57,58*]. Figure 20 [*59*] illustrates the key parameters of this process. In addition to temperature and pressure, as mentioned earlier, the liquid phase plays a fundamental role and requires accurate evaluation in terms of the chemical composition of the compound used, the molarity of the solution, the residence time of the ceramic paste in the mould, and the characteristics of the powder, including particle size and solubility.

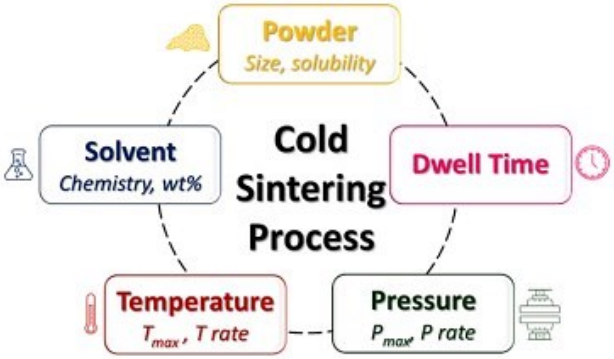

Figure 20 Cold sintering process parameters [59]

This process exhibits notable similarities with the liquid-phase sintering process, as reported in Paragraph 2.2.1.2. The presence of a liquid phase acting as a solvent and the simultaneous application of pressure and temperature make the densification mechanism a process of dissolution and precipitation. However, the use of lower temperatures, higher pressures, longer process times, lower energy requirements, and lower costs are the key elements that distinguish cold sintering in the field of materials engineering. It is important to note that the densification process is the result of a series of phenomena, including dissolution, particle reorganization, and plastic deformation through dislocations and grain boundary sliding.

There is no standard protocol for the practical development of the cold sintering process; however, a general procedure can be outlined as a basis. Initially, the solvent is mixed with the ceramic powder to promote contact between the liquid and solid phases. Subsequently,

the ceramic paste is poured into a steel mould and subjected to pressure using a hydraulic or mechanical press. The heating phase is facilitated through a heating system incorporated into the mould itself, for example, a metal jacket surrounding the mould, as schematically illustrated in Figure 21.

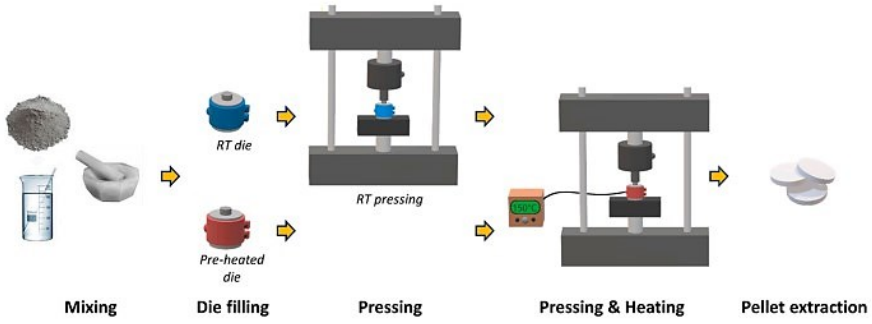

Figure 21 Cold sintering process schematical stages [59]

The mould can be filled with the ceramic paste at room temperature or after preliminary preheating. Studies conducted by *Guo et al*. [*59*] compared sintering ceramic pellets at room temperature and after preheating and found no significant differences in dielectric properties and density, which depend on the microstructure. Furthermore, the two-stage compression of the ceramic paste (first at room temperature and then at the process temperature), as developed by *Funahashi et al.* [*60*], did not demonstrate significant differences compared to the direct application of pressure at the process temperature.

Fig. 22 examines cold sintering process from a mechanical perspective, considering that the primary driving forces for densification are temperature, pressure, and the liquid phase.

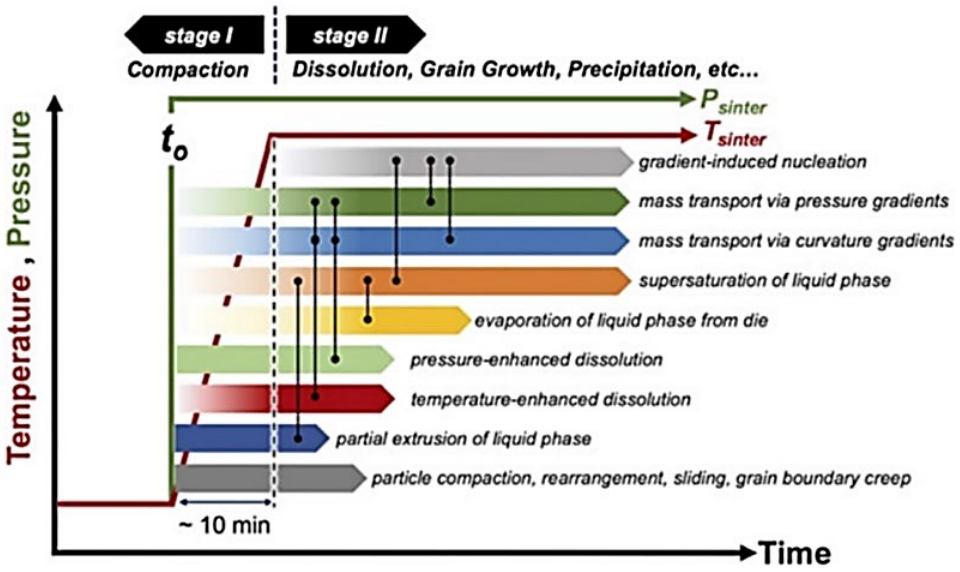

Figure 22 Schematic representation of Cold Sintering Process [62]

As it is a liquid-assisted sintering process, the initial densification step involves the rearrangement of powders and the compaction of solid particles, depending on the chemical affinity between the liquid and solid. In a subsequent step, dissolution and precipitation are the main mechanisms through which densification occurs.

The liquid phase, which typically accounts for about 2-20 wt.% of the total mass [*60*], promotes particle rearrangement and the dissolution/precipitation mechanism. At room temperature, it acts as a lubricant, reducing friction between particles and improving particle packing. The final compaction achieved at the end of the densification process is the result of a combined action between external pressure and capillary forces.

From a thermodynamic perspective, the dissolution-precipitation mechanism is governed by the chemical potential P, which depends on contributions expressed in Equation 8:

$$\mu = \mu_{sp} + \mu_{el} + \mu_d + \mu_\gamma + \mu_{sc} \qquad (8)$$

Here, μ_{sp} represents the work related to the volume change caused by normal stress at the surface, μ_{el} is the non-hydrostatic deformation energy (very low for ceramic materials), μ_d is the energy of plastic deformation of defects, μ_γ is the Helmholtz surface energy, and μ_{sc} is associated with the chemical environment (solubility, etc.).

As introduced earlier, the cold sintering process (CSP) is developed based on fundamental parameters that deserve a more detailed presentation to provide a comprehensive assessment of the CSP. While in conventional sintering, the driving force for powder consolidation is the thermal energy generated by reaching high temperatures, in CSP, the driving force is mechanical energy applied at pressures not exceeding about 700 MPa. *Leng et al.* [*63*] investigated the effect of pressure on PP and found a change of approximately 15% in density values when transitioning from 300 MPa to 760 MPa.

Temperature changes, however, do not have effects of the same magnitude as pressure. Nevertheless, temperature plays an important role in the densification phenomenon. *Charoonsuk et al.* [*64*], for instance, demonstrated that increasing the temperature from 25°C to 160°C leads to higher density values, increasing from 63% to 79%, with greater compaction, respectively.

The cold sintering process is generally quite rapid, typically not exceeding 1 hour. This is because densification mainly occurs through dissolution and diffusion mechanisms, facilitated by the solvent. However, it is also true that once the solvent is completely evaporated, the dissolution mechanism ceases.

Funahashi et al. [*65*] demonstrated that effective densification of zinc oxide (ZnO) could be achieved through the judicious addition of acetic acid in an aqueous solution. Specifically, one gram of ZnO particles with dimensions of 0.24 µm, mixed with a 1M acetic acid solution, reached a relative density exceeding 90% under the following conditions: pressure (P) of 385 MPa, temperature (T) of 126°C, and a time (t) of 60 minutes. Furthermore, by extending the cold sintering process to a temperature of 300°C, the samples achieved conductivity values comparable to those obtained through conventional sintering at 1400°C.

On the other hand, barium titanate ($BaTiO_3$) is known to require prolonged sintering at temperatures ranging from 1300 to 1400°C (slightly lower for nanometric particles*). Guo et al.* [*66*] successfully developed the cold sintering process using 50 nm diameter $BaTiO_3$ particles. They employed a suspension of $Ba(OH)_2/TiO_2$ in deionized water with a $Ba(OH)_2$ concentration of 0.1M. Through this process, by applying a pressure of 430 MPa first at room

temperature (25°C) for 10 minutes, followed by a temperature increase to 180°C with a development time of 30 minutes, they achieved a relative density of approximately 95%. This value remained stable even when varying the development time up to a maximum of 180 minutes. Additionally, by subjecting the obtained samples to an annealing heat treatment, the relative density increased to around 98%.

These results highlight the effectiveness of the cold sintering process in densifying ceramic materials, offering significant advantages in terms of temperature and processing time compared to conventional techniques. Building upon these promising findings and considering the achieved results, the scientific community has embarked on similar experiments involving glassy materials, which, as mentioned earlier, possess unique characteristics.

L. Karakasulu et al. [*67*] conducted a densification process on recycled soda-lime glass powder, characterized by particles with sizes smaller than 25 μm and a weight percentage composition as follows: SiO_2 (71.59%), Al_2O_3 (1.23%), CaO (8.73%), MgO (4.17%), Na_2O (13.63%). This process was developed under various conditions, varying the concentration of NaOH from 5 to 15M and the temperature from 125 to 250°C, while keeping the pressure constant at 250 MPa. The maximum achieved relative density was 95.2%, obtained with the following combination of parameters: [NaOH]=15M, P=250 MPa, T=250°C, t=20 minutes.

B. Santhosh et al. [*68*] achieved interesting results using colloidal silica particles with dimensions of 1±0.34 μm. Cold sintering process was developed at a constant temperature of 200°C, with a dwell time in the mould of 15 minutes. They varied the pressure values from 200 to 600 MPa and used a liquid phase with a concentration of 2M, testing various hydroxides, including sodium hydroxide (NaOH), potassium hydroxide (KOH), and lithium hydroxide (LiOH), to evaluate which of them provided the best performance in terms of relative density. The results demonstrated that the best performance was achieved using sodium hydroxide (NaOH). With a pressure of 500 MPa, a relative density of 95% was attained. It is interesting to note that, although KOH produced similar results, significantly lower densities were obtained using LiOH.

This research highlights the importance of a better understanding of process parameters and their optimization in glass production using the cold sintering process. Therefore, the final bibliographic reference cited will be a fundamental source of inspiration for future experiments in the field.

2.3.2 Flash Sintering process

The term "Flash Sintering" (FS) is used to describe a "*materials sintering technique that involves the simultaneous exposure of the material to an electric field and heat. In this process, the material undergoes sintering within an electric field range of 7.5 V/cm to 1000 V/cm. The onset of sintering is characterized by a power dissipation ranging from 10 to 1000 mW/mm^3, accompanied by a nonlinear increase in the material's conductivity. The time required to complete the sintering process is less than one minute*". This definition, as formulated by *Cologna et al.* [*69*], identifies a phenomenon known as the "flash event" within the FS process. This phenomenon occurs when a critical combination of electric field and temperature, defined as T_{onset}, is reached, leading to rapid and instantaneous densification of the material.

In the scientific literature, various experimental approaches have been proposed to develop the FS process. However, they all agree on the need to prepare the sample using techniques for uniform mixing of ceramic powders with the addition of binders and dispersants. Subsequently, the prepared material is shaped into a specific geometry to be ready for compression. Fig. 23 *[70]* illustrates different experimental configurations used for the development of this process.

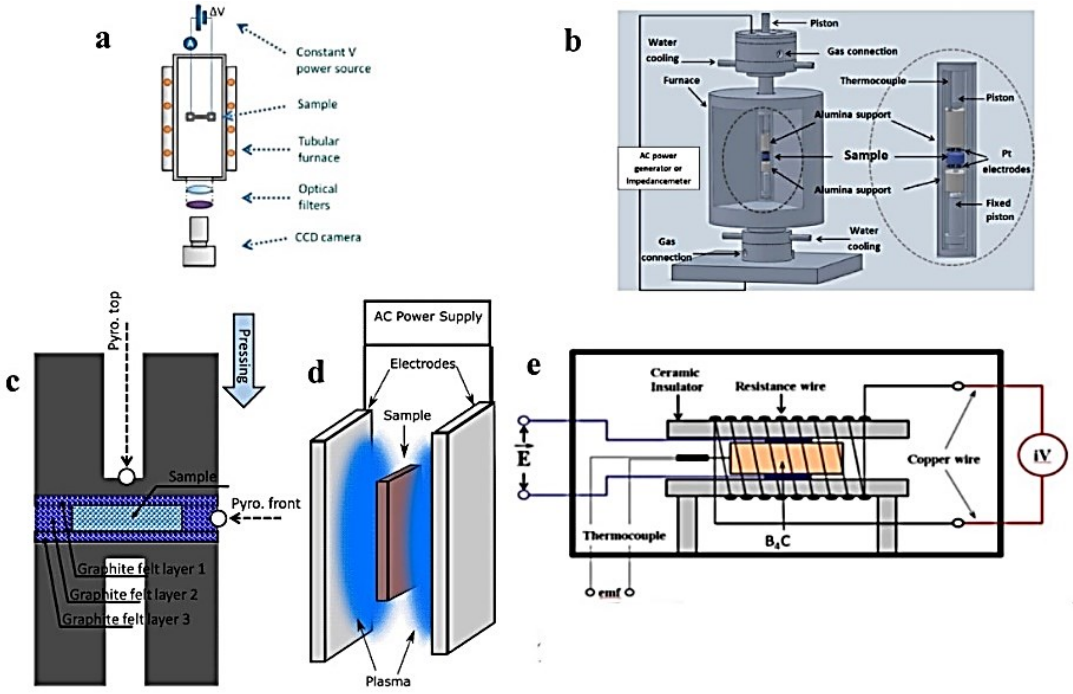

Figure 23 Schematic configuration schemes of FS process [70]

The configurations represented in *a, d*, and *e* are configurations developed without the application of pressure, while those in *b* and *c* are process schemes that also utilize the effect of pressure to promote densification. The diversity of these configuration schemes immediately suggests that pressure is not an essential condition in this type of process. In configurations without pressure, silver or platinum pastes are used to achieve good electrical contact, thereby minimizing contact resistance between the sample and electrodes. However, this configuration, despite not employing pressure, has limitations in electrode removal, as the electrodes could potentially be co-sintered with the ceramic powder. Pressure-assisted sintering, on the other hand, promotes electrical contact between electrodes and the sample, with graphite punches used as electrodes.

The sintering of ceramic powders occurs through six material transport mechanisms: lattice diffusion from particle edges to the neck junction, grain boundary diffusion, viscous flow, surface diffusion, and gas-phase transport. According to research conducted so far, the most significant contribution to sintering is attributed to the electric field. Many researchers [*71*]

use direct current by applying an electrical potential in the range of 10-5000V and a current of 0.5-1.5A. The choice may be influenced by economic considerations, as DC current development equipment is generally less expensive than AC equipment. However, it is difficult to definitively state how alternating current or direct current may influence the FS process. What is certain is that under the influence of an electric field, the sintering behaviour can be divided into two regimes [*72*]: below a critical electric field (E_{crit}), there is a moderate increase in the sintering rate, which increases significantly (reaching timescales of seconds) above E_{crit}. *Park J. et al* [*53*] have concluded that the transition from the first regime to the second occurs more rapidly as the electric field decreases.

As mentioned earlier, pressure plays a significant role in increasing the material's compaction level, facilitating particle rearrangement, and accelerating diffusion, resulting in reduced porosity. However, establishing a direct comparison between pressure-assisted and non-pressure-assisted systems is complex due to the various configurations used, highlighting how pressure is just one of the parameters influencing the process.

Particle size plays a crucial role in this context. *Francis et al.* [*74*] conducted a study on 3YSZ powders with particle sizes of 1, 2, 5, and 10 microns in a Flash Sintering process developed in continuous current mode, with heating temperatures ranging from 920°C to 1040°C. They demonstrated that the onset of sintering (T_{onset}) increases with increasing particle size. This phenomenon is attributed to lower resistivity in smaller particles, promoting the formation of conductive junctions during heating. However, the relationship between particle size and T_{onset} may require further investigation in future research.

The Flash Sintering process can be carried out in various controlled environments. The atmosphere in contact with the sample can be highly oxidizing if rich in oxygen or highly reducing in the presence of hydrogen. In equilibrium conditions, the atmosphere affects the concentration of defects within the material, thus influencing conductivity. For example, in p-type conductors (such as ZrO_2), conductivity varies directly with the partial pressure of oxygen, while in n-type conductors (such as SnO_2), the opposite occurs.

Temperature is a critical parameter that must be carefully controlled during the process to avoid thermal gradients that could damage the material. Temperature measurement techniques reported by *Thomas RA* [75] highlight that the average temperature of species controls densification rates. These measurements contribute to a better understanding of the kinetics of the Flash Sintering process, which is still an ongoing area of research.

In conclusion, it is essential to emphasize that input parameters need to be carefully configured to specific values, while output data can be recorded and monitored throughout the process. Tab. 2 provides the physical principles of each temperature measurement method used in the literature, explaining the underlying principle and the location of the measurement device.

Table 3 Physical principle and probing position for the different temperature measurement methods used in the literature [76]

Method	Principle	Probing position, local or averaged, *Source of error*
Thermocouple	Heat transferred to an electrically insulated metals junction	Surface, Local *Thermal contact and thermal insulation of the thermocouple*
Pyrometer/ thermo-cameras	Spectral radiation intensity of samples at given wavelengths	Surface, Local *Uncertain emissivity and electroluminescence*
Optical emission spectroscopy	The spectral emission from the sample	Surface, Local *Blackbody radiation fitting*
Impedance analysis	The relationship between impedance and temperature	Bulk, Averaged *Change in sample shape/ dimensions and characteristics**
Thermal expansion	The relationship between thermal expansion and XRD peak positions of Pt placed on samples	Bulk, averaged, Change in material shape (e.g. softening)

Many research studies [*76*] have been conducted to produce materials through the Flash Sintering (FS) process, with particular emphasis on materials possessing remarkable electrical properties. In particular, the FS process has been successfully applied to the production of ionic conductors, including yttria-stabilized zirconia (YSZ) in both cubic and tetragonal forms, as well as insulating materials such as alumina (Al_2O_3), barium titanate

($BaTiO_3$), potassium niobate ($KNbO_3$), titanium oxide (TiO_2), and silicon carbide (SiC). In addition to the production of materials with remarkable electrical properties, the FS process has proven to be highly versatile and has found application in a wide range of advanced materials. These encompass not only ionic conductors and insulators but also ferric materials, dielectrics, advanced ceramics, and even multifunctional composites.

The primary appeal of FS lies in its ability to significantly reduce sintering times compared to conventional methods, enabling the production of advanced materials with improved properties in terms of density, conductivity, and microstructure. This innovative technique is, therefore, a rapidly growing area of research, with the goal of fully harnessing its potential across a wide spectrum of applications, from electronics to energy, materials science, and beyond. Research continues to play a pivotal role in optimizing the FS process and exploring new avenues of application.

2.3.3 Spark Plasma Sintering process

The "Spark Plasma Sintering" (SPS) is a sintering technique that operates under moderate pressure, often exceeding 150 MPa, and at high temperatures, reaching temperatures up to 2500°C [*77*]. The key innovation of this technique lies in the use of high-density, low voltage pulsed electrical current that passes through a graphite mould containing the material powder to be sintered. The heating generated by the Joule effect can occur extremely rapidly, with heating rates exceeding 1000°C per minute. This combination of high heating rates and high uniaxial pressure allows for densification of materials in significantly shorter times and at lower process temperatures than conventional sintering processes. The SPS technique is commonly adopted for materials that pose challenges in densification, such as highly refractory materials, nanocrystalline materials, or metastable materials. It is often used to produce highly porous materials or multilayered structures. There is no universal protocol for the development of the SPS process; different variations and optimizations of the original techniques have been developed over time, leading to the creation of a standard format for the equipment used in Spark Plasma Sintering. The following Fig. 24 [*78*] represents the

general experimental setup used in this technique and identifies each part of the process, which will be analysed in detail below.

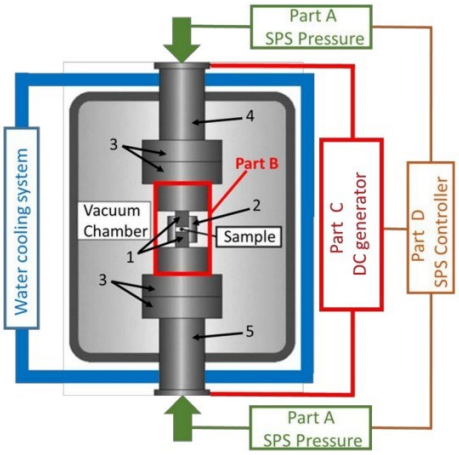

Figure 24 Schematic of a SPS apparatus

The Spark Plasma Sintering (SPS) apparatus consists of several key components:

A. Hydraulic Pressure Application Device: this part of the apparatus is responsible for generating and applying the hydraulic pressure required for the SPS process. Typically, the device has a vertical pressurization axis.

B. Reaction Chamber: the reaction chamber is where the sintering process takes place under high pressure and temperature conditions. This chamber is often placed in a controlled environment, such as a protective atmosphere or vacuum, to prevent material oxidation during the process. Inside the reaction chamber, there are two cylindrical steel elements, known as pistons, which move vertically. Within these pistons, there is a cylindrical graphite mould designed to contain the powder of the sample to be sintered.

C. Direct Electric Current Device: this part of the apparatus is responsible for applying direct electric current to the material inside the graphite mould. The current is supplied through two cylindrical branches connected to the graphite mould, where the current flow occurs. The direct current is pulsed, with each pulse being of short duration. The duration of each pulse does not exceed 3.3 milliseconds (ms). The number of pulses per unit of time can vary, but

commonly follows a pulsation pattern of 12:2, meaning that twelve pulses are followed by a pause of two pulses, resulting in a total duration of 6.6 ms during which no current is applied.

Part D: Control and Monitoring Computer: the computer serves as the brain of the apparatus and is responsible for controlling and monitoring all the components of the setup. It manages the hydraulic press, the vacuum system, and the electric current generator, ensuring that the process proceeds accurately and in a controlled manner. It also collects important data during the process for monitoring and recording purposes.

Undoubtedly, the Spark Plasma Sintering (SPS) process is subject to the influence of a complex set of parameters, each of which plays a crucial role in engineering advanced materials. Among these parameters, it is necessary to mention the intrinsic nature of the sample, encompassing both its microstructure and chemical composition. Electric current, temperature, heating rate, dwell time of the powder in the mould, and, above all, pressure are critical aspects governing the SPS process. Among these, pressure stands out as a key factor because it is widely known to be capable of drastically altering the mechanical, chemical, physical, and structural properties of the material under examination [*78*].

In particular, the applied pressure acts as a reducer of interparticle distances, facilitating contact between individual particles. This, in turn, leads to an increase in the speed of atomic diffusion processes, consequently reducing the time required to complete the sintering cycle. However, it should be noted that time is not the only parameter subject to reduction under pressure.

Temperature, a key element for material densification, can be significantly reduced through pressure application, as pressure amplifies the driving force of densification processes and influences mass transfer within the material. For example, *D. Vallauri et al.* [*79*] experimentally demonstrated that to achieve densified nanocrystalline zirconia by applying a pressure of 800 MPa, higher than the norm, it is necessary to work at a temperature below 800°C, approximately 600°C lower than conventional conditions. Based on these observations, the possibility arises that the application of high pressures to nanostructured

materials may pave the way for the creation of new materials with unique properties and significant engineering applications.

Another critical parameter to consider is electric current. The application of current between the two electrodes inside the SPS equipment generates an electric arc, fuelled by the significant current density concentrated in a confined contact area between the material particles. This phenomenon produces a sudden local increase in temperature, reaching values on the order of ten thousand degrees Celsius. This thermal elevation causes the evaporation and fusion of surface powder particles in the SPS process, resulting in the formation of junctions between the particles themselves. The illustration in Fig. 25 schematically represents this role of the current [*80*].

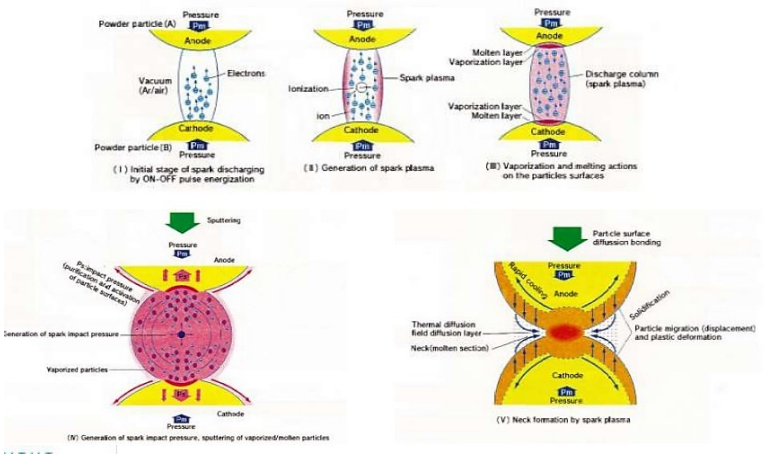

Figure 25 Schematic representation of current's role in SPS process

C. W. Wang et al. [*81*] conducted a significant study, highlighting that temperature is an important parameter as it promotes diffusion mechanisms. However, the impact of temperature is lower compared to that of pressure. Unlike what was observed earlier for pressure, temperature alone does not fully explain the significant abbreviation of process times in the case of Spark Plasma Sintering compared to conventional processes.

Furthermore, *G. Bernard-Granger et al*. [*82*] worth emphasizing that the internal parameters of the material, including aspects such as physical, chemical, and mechanical properties, play a fundamental role in the SPS process. This underscores the importance of the overall nature

of the sample, encompassing all these properties, as they significantly influence the sintering process through Spark Plasma Sintering. In its most general form, to provide an overview of the complexity of the process, the diagram below (Fig. 26) should be presented, provided by the "Institut Carnot-Chimie Balard Cirimat" [*83*].

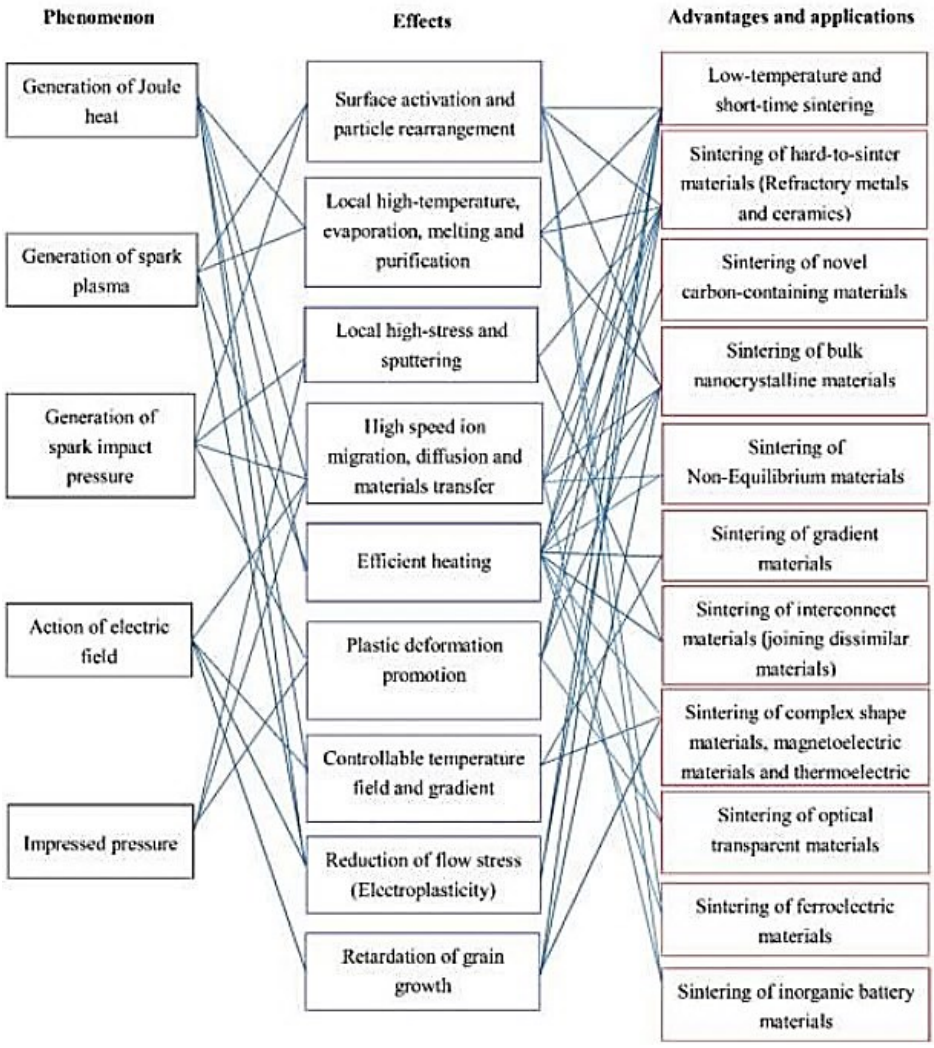

Figure 266 General perspective of SPS parameters linked to their effects and applications.

This diagram relates the phenomena that occur during the Spark Plasma Sintering (SPS) process to the effects that these phenomena produce within the process itself. These effects are, in turn, connected to the advantages of the SPS process and the applications where this process is particularly suitable for the production and sintering of specific materials. This

complex diagram highlights the wide range of interactions and connections that characterize the SPS process, emphasizing its relevance in various fields of materials engineering.

Consequently, this technique emerges as a valuable engineering resource to produce a wide range of artifacts, from the most complex to thermal insulating materials for aerospace applications and transparent ceramics.

S. Grasso et al. [*84*] have successfully developed the Spark Plasma Sintering process to produce structured ferroelectric ceramics. In the case of $CaBi_2Nb_2O_9$ synthesis, a high-temperature piezoelectric material used in technical devices, the process was divided into two phases. Initially, using fine powder with particle sizes less than 200 nm, a first step was conducted at a pressure of 80 MPa, a temperature of 1200°C, and a time of 3 minutes. This phase led to a fine granular microstructure and a relative density greater than 90%. Subsequently, a second step was carried out at 80 MPa, 1350°C for 5 minutes to achieve the desired structured microstructure. During this experimental phase, it emerged that texturing in SPS, in a two-step approach like the one adopted, requires accurate optimization of parameters, as temperature, pressure, and time play a critical role, and poor optimization can lead to a decrease in density in the second step.

J. Zhang et al. [*85*] used SPS to produce transparent silica glass. They used silica powder with particle sizes less than 500 nm and placed it in a cylindrical graphite mould with a diameter of 30 mm. The powder was sintered at temperatures ranging from 800°C to 1600°C, with a time of 10 minutes, and subjected to a uniaxial pressure of 100 MPa, with a heating rate of 100°C/min. Some samples were subsequently annealed at 1000°C for 3 hours. The study showed that the maximum density, 100%, was achieved for samples sintered at 1400°C (which had also undergone annealing), and these samples did not undergo crystallization during the process.

H. Masai et al. [*86*] conducted experiments using SiO2 silica powder with a purity of 99.999% and particle sizes of 25 μm. They controlled the sintering temperature following a specific sequence: initially, they raised it to 600°C from about 25°C in about 5 minutes, keeping it at 600°C for about another 5 minutes. Then, they increased it to 1300°C or 1400°C

at a constant heating rate of 10°C/min and maintained it at this temperature for an additional 15 minutes. The process was conducted under vacuum, with pressure variations from 6 to 70 MPa. At the end of the experiments, they obtained glass without grain boundaries or precipitated crystallites. The highest density (2.249 g/cm^3) was achieved at a pressure of 70 MPa and a temperature of 1400°C.

Z. Shen et al. [*87*] extended the application of the SPS process using even smaller SiO_2 particles, with sizes less than 10 nm. After being subjected to a pressure of 100 MPa, a temperature of 1000°C for 5 minutes, and annealing at 900°C for 5 hours in air to remove the graphite surface, they obtained a pellet. This sample showed significant similarities to conventional silica glass but differed in having a significant presence of hydroxyl groups in its composition, accompanied by traces of graphite contamination.

The experimental work conducted in this study will be closely related to the recent literature review. In Chapter 4 of the thesis, the SPS process developed to produce silica glass from SiO_2 particles with very similar sizes to those treated in the cited studies will be examined.

2.4 Conclusions

This chapter has laid the foundation for the experimental research presented in this work. Reducing the energy impact of processes is a fundamental goal in the fight against climate change. Lowering temperatures in processes could be an effective solution compared to traditional methods. The properties of glass and scientific evidence demonstrate that applying glass to unconventional sintering techniques for ceramic materials is a very promising research avenue.

In the following chapters, the methodologies and sample analyses will be examined, as well the process parameters and results obtained for each type of glass. This scientific approach will elucidate how the use of glass can enhance the energy efficiency and properties of ceramic materials produced using unconventional sintering techniques.

CHAPTER 3

Experimental methodologies: characterisation techniques and process systems developed.

The following chapter will delve into the experimental phase that underpins this research work. The experimental investigation encompassed the utilization of specialized equipment capable of generating elevated pressures; this facilitated the execution of sintering processes that diverge from the traditional methods. Specifically, three distinct techniques were employed: cold sintering, Spark Plasma Sintering and Diamond Anvil Cell.

Moving forward, the subsequent section of this chapter will comprehensively present the various characterizations carried out on the obtained samples. These characterization analyses, introduced with a concise elucidation of their fundamental principles, will be meticulously detailed. Each analysis will encompass explicit information regarding the employed instrumentation, the physical location of analysis, and the specific parameters that were scrutinized, along with their corresponding values.

3.1 High pressure generating devices.

Pressure-generation devices employed in this study are outlined in this section. For each distinct process, comprehensive descriptions of the press type, mould configuration, and operational principles are provided. These elucidations are intended to facilitate a deeper comprehension of the subsequently discussed sample production in Chapters 4 and 5.

3.1.1 Cold sintering process

The cold sintering process (CSP) was carried out at the laboratories of the Department of Industrial Engineering (DII) at the University of Padova. Nanostructured glass powder, specifically, commercially available borosilicate glass powder, was subjected to the process outlined in this paragraph.

In order to provide a more comprehensive account of the experimentation related to this process, a specific description of the type of press employed and its corresponding operating principle is hereby presented.

3.1.1.1 Hydraulic press set-up

The cold sintering process has been developed using the "Specac"-type press, a state-of-the-art hydraulic press, specifically designed for the uniaxial compaction of powders. It provides precise pressure control and uniform distribution throughout the sample; specifications are reported in Tab. 1.

Table 4 Specac Press - technical data sheet

Parameter	Specification
Maximum pressure [tons]	15
Maximum height [mm]	610
Maximum width [mm]	310
Maximum depth [mm]	190
Weight [kg]	50
Lower piston stroke [mm]	25,4
Upper lead screw travel [mm]	89
Lower pressing face diameter [mm]	86
Upper pressing face diameter [mm]	32
Maximum width of sampling area [mm]	134
Maximum depth of sampling area [mm]	141
Oil capacity [litres]	0,284
Oil type	CL 37

WP-1 Pressing Die Set type press, manufactured by Across International is the mould-type used for cold-sintering process; it offers heating and cooling capabilities, allowing for controlled temperature conditions during the cold sintering process.

The following Fig. 1. and Tab. 2 visually illustrates the components and the specification of the mould utilized, respectively.

Figure 7 Die parts.

Table 5 Specifications of the WP-1 Pressing Die Set

Parameter	**Specification**
Model	SDS25.H
Manufacturer	Across International
Operating principle	Hydraulic uniaxial compaction
S/N	201914116
Power	220 VAC, 50/60 Hz, 280 W
Maximum temperature [°C]	250
Rockwell Hardness	Rc 62
Internal diameter [mm]	25
Outer diameter [mm]	92
Sheath heigh [mm]	45
Total heigh (w/o sample) [mm]	105
Maximum loading height [mm]	25
Thermal plate diameter [mm]	105
Temperature rate [°C/min]	1
Accuracy	1%
Environment	0-50 °C, <35% RH humidity

The mould consists of various components: the mould itself, where the powder is inserted, and an attached piston that enables compression under the action of the press. Additionally, an external heating ring is tightly secured around the mould to provide conductive heating.

To fulfil their designated functions, the components are constructed using the following materials:

- Sleeve, ejector, and support: Cr 12 hardened carbon mould steel
- Core die and push rod: W18Cr4V hardened carbon tool steel

The Core die and push rod are made of W18Cr4V hardened carbon tool steel, which is a high-speed carbon tool steel. The mechanical (A) and physical (B) properties of this material are presented in the following Tab. 2.

Table 6 Mechanical and Physical Properties of W18Cr4V Hardened Carbon Tool Steel

(A) Mechanical properties

Property	**Value**
Hardness (Brinell) [HBW]	131
Tensile Strength [MPa]	725
Yield Strength [MPa]	118
Elongation [%]	31
Impact KV/Ku [J]	21
Reduction in cross section on fracture [%]	41

(B) Physical properties

Property (at 117°C) [*73*]	**Value**
Density [kg/dm³]	414
Poisson's coefficient	131
Thermal Conductivity [W/(m·°C)]	12,2
Coefficient of Thermal Expansion [× 10^-6 / °C]	13

As can be observed from the tables presented above, this steel is characterized by a high tungsten content, which imparts excellent hardness, high tensile strength, and resistance to elevated temperatures. The material exhibits a relatively high density, contributing to its

overall strength and durability. Moreover, its low coefficient of thermal expansion indicates minimal dimensional changes with temperature variations, making it well-suited for precision systems aimed at conducting heat by conduction.

As the press is manually operated, it is feasible to establish a correlation between the applied force and the corresponding pressure value. This enables us to determine the force required to achieve the desired pressure on the system.

Considering that ID $(\text{internal diameter}) = 25\ \text{mm}$, the area subjected to compression is $A = 4{,}9087 \cdot 10^{-4} m^2$; the subsequent Table UU illustrates the desired relationship between force and desired pressure.

Table 7 tons-MPa correlation

tons	N	P (MPa)
1	9806,65	19,9781
2	19613,3	39,9562
3	29419,95	59,9343
4	39226,6	79,9124
5	49033,25	99,8905
6	58839,9	119,8686
7	68646,55	139,8467
8	78453,2	159,8248
9	88259,85	179,8029
10	98066,5	199,781
11	107873,2	219,7591
12	117679,8	239,7372
13	127486,5	259,7153
14	137293,1	279,6934
15	147099,8	299,6715

Such an approach allows for precise process control and ensures that pressure conditions are optimized to produce high-quality glass-ceramic materials.

3.1.1.2 Operating principle

The cold sintering process has been developed according to the following procedure. The particles intended for sintering are placed in a mortar with a mass equal to the desired amount. Inside the mortar, a basic solution (specifically, NaOH) is added drop by drop while mixing with a pestle, creating a glassy paste.

Subsequently, the glassy paste is inserted into a specially designed mould for cold sintering. There is no direct contact between the mould and the glassy powder; the lower and upper walls of the mould are separated from the powder by two Teflon discs (one for each part). This arrangement allows for easy removal of the sintered pellet, preventing the two base surfaces of the cylindrical pellet from adhering to the mould.

After closing the mould and positioning the upper cylinder, a heating ring is placed around the mould's lateral walls and connected to the heating system. Once the desired temperature is set, the mould is gradually heated while manual pressure is applied using a press. The compression is instantaneous and is applied from the heating phase. After reaching the set-up temperature, the mould is kept at the established temperature and pressure for a specific dwell time. Subsequently, the mould is disconnected from the temperature controller, and the pressure is released.

After an appropriate cooling period, the sintered pellet is extracted for purely visual analyses, with a focus on identifying transparent, translucent, and/or opaque regions. Finally, to ensure complete drying of the pellet, it is placed in an oven at T=70°C for a period of t=24h.

This research aims to explore the effects of different cold sintering conditions on the optical properties and microstructure of glass-ceramic materials, providing valuable insights for process optimization. In particular, the conditions that will be analysed are represented by the following parameters: liquid-to-solid ratio, quantity of liquid phase, molarity of the liquid phase solution, pressure, temperature, dwell time, drying temperature, and drying time.

3.1.2 Spark Plasma Sintering

The Spark Plasma Sintering process (SPS) was developed at the University C. Bernard Lyon 1. The collaboration with this university was established to achieve significantly high pressures, in the range of several gigapascals (GPa), to investigate their role during the sintering process. This objective is accomplished using the "Paris-Edinburgh" press-type.

Below, detailed information on sample preparation and the operating principle behind the sintering process under investigation are provided.

3.1.2.1 Paris-Edinburgh press [88]

To facilitate the Spark Plasma Sintering (SPS) process using the Paris-Edinburgh press, a preliminary step of sample preparation is required, which involves creating a pre-compacted powder pellet with a cylindrical shape matching the SPS mould dimensions of 7mm in diameter and 3mm in height.

To achieve effective powder pre-compaction, an Enerpac swan-neck press-A330,295kN type hydraulic press is utilized. The press specifications are outlined in Table 1.

Table 1 Enerpac Press - technical data sheet

Properties	**Values**
Piston diameter [mm]	42,9
Pellet contact surface [mm^2]	1445
Maximum Operating pressure [bar]	700
Press capacity [kN]	267
Maximum vertical daylight [mm]	260
Maximum Bed Width [mm]	178
Cylinder type	Single-Acting
Weight [kg]	100

Tab. 2 provides the correlation between the oil pressure and the force necessary to apply that.

Table 2 Oil pressure-applied force correlation

Oil pressure [bar]	Force [kN]	Force [tons]
50	7,2	0,737
70	10,1	1,03
80	11,6	1,18
90	13	1,33
100	14,4	1,47
150	21,7	2,21
200	28,9	2,95
300	43,3	4,4

Oil pressure, imparted to achieve the powder compaction, is connected to the pressure inside the sample which would be created; equation (*3.1*) links the sample pressure (P_{sample}) to the oil pressure (P_{oil}) through the pellet and press surfaces' (S_{pellet}, S_{press})

$$P_{sample} = P_{oil} \cdot \frac{S_{press}}{S_{pellet}} \qquad (3.1)$$

After the creation of a pre-compacted powder pellet, the sample cell assembly must be prepared, whose section view is shown in the *Figure 1*.

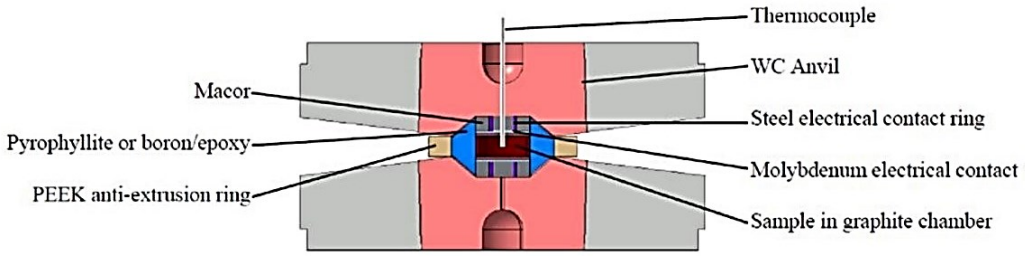

Figure 2 Section of sample cell assembly for the Paris-Edinburgh press

The prepared pellet is placed inside a graphite mould, positioned at the centre of an 8mm fired pyrophyllite gasket. Two steel-electrical contact rings and two molybdenum discs are placed above and below the graphite mould to ensure the electrical feed. Macor discs provide thermal insulation to preserve the WC anvils. Furthermore, a polyether ether ketone ring is used to enclose the gasket to limit its extrusion and enhance pressurization efficiency.

The entire assembly is then placed between two anvils, comprising hardened steel in the bulk and tungsten carbide in the central region where the cell is placed. Thanks to the anvils and gasket geometry, the pressure is applied in a quasi-isostatic manner on the sample. These preparatory steps must be executed with utmost precision to ensure, on one hand, the complete filling of the mould and, on the other hand, the proper alignment between the mould and the anvils. The process involves thorough cleaning steps and evaluation of geometrical characteristics to facilitate the correct functioning of the press and achieve appropriate thermal flow during the process.

The entire system developed is subsequently positioned within the Paris-Edinburgh press, as depicted in Figure A. This press comprises an upper and lower piston: the former is fixed to a stationary piston, facilitating the mechanical clamping of the cell assembly, while the latter primarily undergoes the compression action during the process. Displacement sensors are employed to monitor the relative shift between the two pellets.

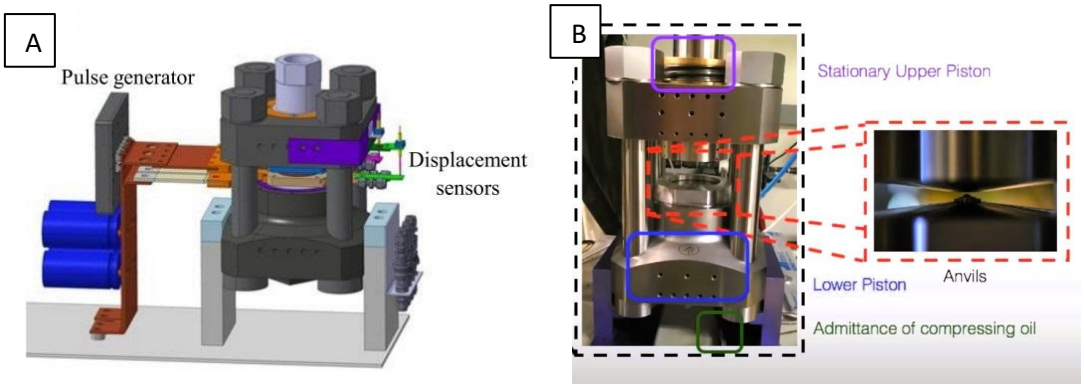

*Figure 3 Spark Plasma Sintering Devices: Paris-Edinburgh press (**A**) and entire system (**B**) [88]*

The pressure system is interconnected with a pulse generator (B), which generates a high-intensity electric current flowing through the sample to produce heat via electrical resistance. This rapid heating process allows the sample to achieve elevated temperatures within a noticeably brief time, typically in a matter of minutes. The connection phase between the press and the current generator plays a crucial role. It must be precise to deliver a current pulse with meticulous control over voltage and intensity, ensuring uniform and controlled heating of the sample.

Upon completion of the preparation steps, which include powder pre-compaction, mould assembly, and connecting the current generator to the compression system, the Spark Plasma Sintering (SPS) process is ready to be programmed.

3.1.2.2 Operating principle

To initiate the development process, it is crucial to identify the key process parameters, namely pressure and temperature, and gain a comprehensive understanding of how the machine operates.

The pressure and temperature settings are determined as follows:

• For compression, the machine is subjected to a specific value of oil pressure, corresponding to the desired pressure required during the experimental phase.

• The target temperature is achieved by applying a certain power, which is related to the current density passing through the generating circuit.

To calibrate the machine accurately, experimental graphs, such as those illustrated in Figure 3, are used. These graphs provide essential information on the oil pressure (A) and power (B) values needed to achieve the desired pressure and process temperature, respectively. The graph on the left was generated from in-situ neutron diffraction of a NaCl sample, while the second graph was obtained by positioning a K-type thermocouple at the centre of an alumina sample.

These calibration graphs play a critical role in ensuring precise control of the pressure and temperature parameters during the Spark Plasma Sintering process, contributing to successful and reproducible sintering outcomes.

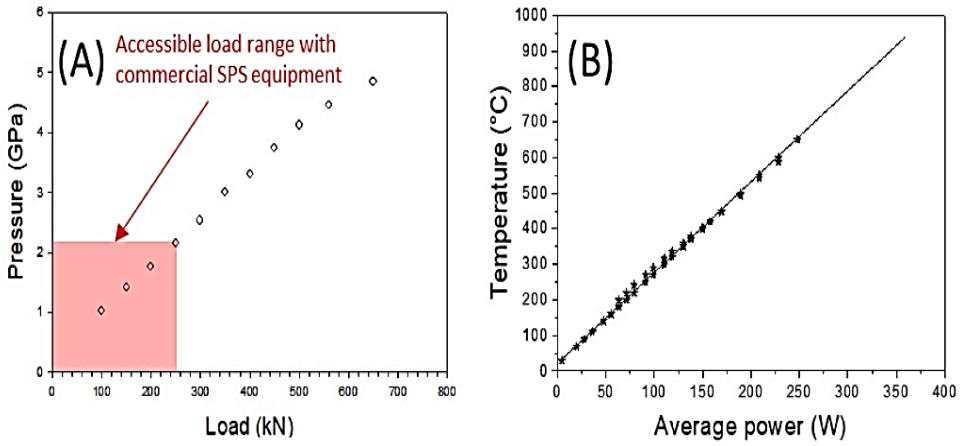

Figure 4 Pressure and Temperature calibration graphs.

For instance, if the objective is to apply a pressure of 2 GPa to the sample, the machine should be adjusted to have an oil pressure of approximately two hundred bar. Similarly, if the desired temperature is 800°C, an average power of around 300W will be necessary.

It is important to note that the Paris-Edinburgh press has its limitations in terms of maximum achievable values. The oil pressure can reach a maximum of 2500 bar, and the temperature can go up to 2000°C. In the SPS Paris-Edinburgh press used, it's possible to achieve pressures of over 4 GPa on a 7mm sample and up to 10 GPa on a 1mm sample.

Reaching the desired pressure and temperature requires precise control of the speed at which these values are achieved, as well as the duration for which they are maintained. The influence of these parameters on the outcome must be considered and appropriately set to achieve the desired results in the Spark Plasma Sintering process. Properly calibrating and adjusting these parameters is essential to ensure successful sintering and the attainment of the intended material properties. Current pulse is another important parameter that must be established. The current generator provides high-frequency current pulses, typically in the kilohertz (kHz) or megahertz (MHz) range, which are applied to the sample. The current pulses have a wide variety of waveforms but are often characterized by high peak power and short pulse duration. When the current is applied to the sample, the current passage through the material generates heat through Joule heating, which, due to the high frequency of the current pulses, occurs rapidly and selectively in the sample, allowing efficient sintering with relatively short processing times. The graph of current generation in an SPS system will depend on the waveform of the current pulses provided by the current generator; Fig. 4 shows an example of current generation graph.

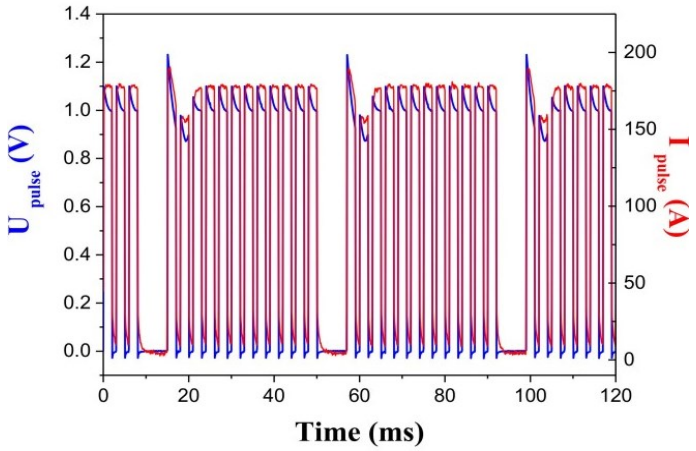

Figure 5 Pulse pattern example

The graph illustrates the variation of current intensity over time. It typically shows peaks of high-intensity current during the application of current pulses, which are then followed by periods where the current decreases or is absent. The precise waveform depicted on the graph is dependent on the specific parameters of the Spark Plasma Sintering (SPS) system and the

design of the current generator utilized in the process. The shape and duration of the current pulses play a significant role in determining the heating rate, temperature distribution, and overall sintering behaviour of the material being processed. These factors must be carefully controlled and optimized to achieve the desired sintering outcomes and material properties.

3.1.3 Diamond Anvil Cell

The diamond anvil cell (DAC) is an instrument that makes it possible to reach extremely high pressures (tens of GPa) and to conduct in-situ measurements to assess the properties of the materials analysed under the action of such considerable pressures.

3.1.3.1 Operating principle

The diamond anvil cell employed in this study is referred to as a "membrane" cell. It derives its name from the pressure application method, which involves deforming a pressurized metal membrane. The cell consists of two identical IA-type diamond anvils with specific cuts, featuring a table facet diameter of 4 mm, a culet thickness of 0.50 mm, and a height of 1.80 mm. The two diamonds have flat circular surfaces, which are securely clamped together at their culets using a circular metal gasket. This gasket is perforated with a hole, defining the experimental volume (as shown in Figure 6).

With the pressurized gas-deformed metal membrane exerting force, the upper diamond is pushed against the fixed lower diamond. The various components that constitute the cell are depicted schematically in Figure 7. This diamond anvil cell design allows for precise pressure application and facilitates experimental investigations under high pressure conditions, offering valuable insights into material behaviour and properties.

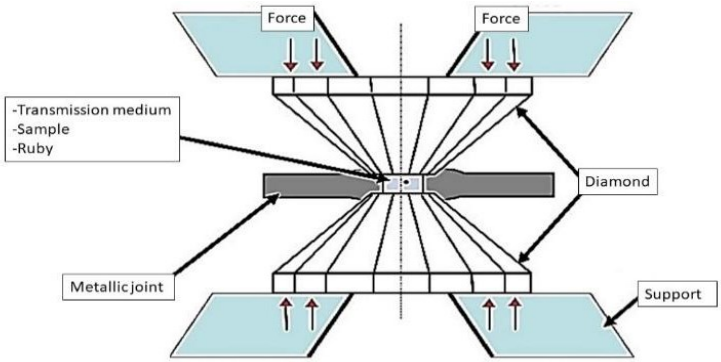

Figure 6 Diamond Anvil Cell process scheme [89]

Figure 7 Diamond Anvil Cell picture

3.1.3.2 Diamond Anvil Cell preparation

The procedure described in this section is detailed in the provided bibliographical reference [*89, 90*].

The first step involves aligning the culet centres of the diamonds. This alignment is done under white light using a microscope after bringing the diamonds into contact. Ensuring proper parallelism is crucial to prevent diamond-to-diamond contact under high-pressure conditions.

In the second step, the stainless-steel gaskets, shaped as 200µm thick discs, are prepared. Before each experiment, the gaskets are indented using the diamond anvil cell, applying

pressure to achieve an approximate thickness of 50μm. This specific thickness is closely related to the pressure to be applied. For higher pressure values, culet dimensions of about one hundred μm and hole dimensions of thirty μm are required. In this case, a conventional drilling machine is used. For higher pressure, a femtosecond laser is used to drill smaller holes.

After the indentation, the centre of the indentation is drilled using electro-erosion, creating a hole typically 120μm in diameter, which defines the experimental volume. Once the gaskets are prepared, they are placed and centred on the lower diamond. The sample is then introduced into the gasket hole, usually in the form of grains measuring approximately 50 μm × 50 μm × 20 μm.

Since the pressure inside the experimental volume is not a straightforward function of the pressure applied to the membrane, a ruby ball (Al_2O_3: Cr^{3+}) of 2-3 μm in diameter is introduced into the experimental volume. The luminescence spectrum of Cr^{3+} (Fig. 8) exhibits two highly intense peaks that shift with pressure, following a calibration curve established by Piermarini [*91*]. This calibration allows for precise pressure determination during the experiments.

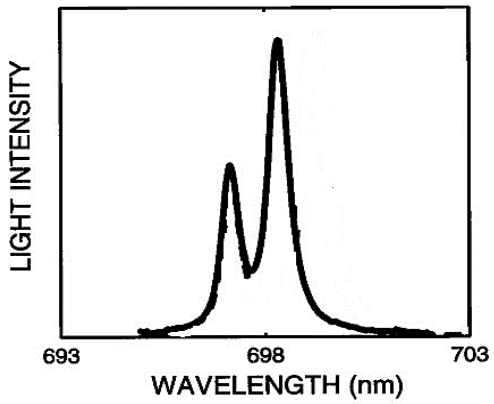

Figure 8 Ruby-Raman spectrum

The position of these peaks directly provides information about the pressure within the experimental volume. The ruby serves as a pressure gauge, and the choice of the pressure-transmitting medium, as well as its hydrostaticity, have been extensively discussed in

Deschamps' thesis [*89*]. The thesis provides detailed insights into the selection and calibration of the pressure-measuring technique, ensuring accurate and reliable pressure determinations during the experiments.

3.2 Characterization analysis

The paragraph under examination addresses the characterization techniques of particles and samples employed during the entire experimental phase of the thesis project in the field of Materials Engineering. The primary goal of these characterization analyses is to gain insights into the properties and structures of the studied materials, facilitating the evaluation of their performance, physical and chemical attributes, and the potential for improvement or optimization. Each technique is characterized by specific parameters and procedural considerations, with the expectation of obtaining distinct information about the material being investigated through their application.

3.2.1 FT-IR

The FT-IR (Fourier Transform Infrared) analysis on micro/nano-sized powders is used to investigate the molecular vibrations and functional groups present in solid-state materials.

In this study, the FTIR analysis was conducted using the "Jasco FTIR 6200 with ATR pro ONE" instrument, where ATR stands for Attenuated Total Reflection; this accessory allows for the analysis of samples in their native solid form without the need for additional preparation, such as making pellets or films.

The key parameters considered during the analysis are as follows:

- *Scan Range*: it defines the range of wavenumbers (cm^{-1}) over which the analysis will be performed. the Scan Range used for the FT-IR analysis covers the mid-infrared region, which typically spans from *4000 to 400* cm^{-1}, allowing the assessment of

various vibrations related to the chemical bondings present in the sample (including water and silica, respectively around 3000 and 500 cm^{-1}).

- *Accumulation*: it refers to the number of scans that are averaged to enhance the signal-to-noise ratio; higher accumulation improves the data quality. In this work an accumulation of *64* scans is used.

- *Resolution*: it determines the level of detail in the obtained spectrum; higher resolution allows for finer spectral features to be resolved. The resolution value chosen is *4* cm^{-1}.

- *Type*: this parameter specifies the type of data processing or mathematical algorithm used to convert the raw interferogram data into the final FTIR spectrum. The analyses are conducted in *Abs*-type.

The parameter values used are critical for replicating the experiments and ensuring the accuracy and reliability of the obtained FTIR spectra.

3.2.2 Raman spectroscopy

Raman spectroscopy is an optical phenomenon discovered in 1928 [*92*]. This effect is based on the scattering of light and is widely employed in material study and characterization. It allows for the identification of molecular vibrations within a material; it provides insights into molecular bonding, crystal structures, and chemical compositions.

Two instruments were utilized for this study, both located at the University of Lyon:

- Labram Aramis (Horiba): This instrument facilitates Raman measurements with two immediate wavelength options, 473nm and 633nm.

- Labram Hr Evo (Horiba): This equipment enables measurements at lower frequencies, starting from $10cm^{-1}$, using 532nm and 660nm wavelengths.

Parameters considered for the experimental setup included:

- *Acquisition Time*: the duration for which data is collected during each measurement.
- *Accumulations*: the number of times the measurement is repeated to improve signal-to-noise ratio.
- *Lens Type*: the specific lens used in the setup to focus the laser light on the sample.
- *Laser wavelength*: the wavelength of the laser light directed onto the sample.
- *Spectrum*: the range of wavenumbers analysed in the Raman spectrum.
- *Filter*: the percentage of filtered light to eliminate unwanted signals.

Due to the requirements of experimental development and the variability in sample conditions, fixed parameter values for each test were not feasible. Therefore, in the work, the parameters will be presented individually alongside the characterization of the samples.

3.2.3 SEM, TEM, XRD

- SEM

An SEM (Scanning Electron Microscopy) analysis on micro/nano-sized powders is a powerful tool used to investigate the surface morphology and microstructure of materials at high magnification. It provides detailed information about the particle size, shape, and surface features, allowing researchers to gain insights into the physical characteristics of the powders. In the context of this study, the SEM analysis was conducted using two different instruments due to the experimental requirements. Some analyses were carried out at the laboratories of the Department of Industrial Engineering (DII) at the University of Padua, using the "Zeiss Sigma HD, Schottky FEG source" instrument. Others were performed at the laboratories of the University of Lyon 1, using the "MEB FEI NanoSEM450" instrument.

Due to the use of two different instruments, the values of the parameters used for each SEM analysis will not be described in the current paragraph. Instead, they will be presented in subsequent chapters when reporting the characterization of each specific sample.

Specifically, the parameters of the SEM analysis developed at Padua will be presented in Chapters 5 and 6, while those from the analysis conducted in Lyon will be presented in Chapter 4.

- TEM

Transmission Electron Microscopy (TEM) is a powerful imaging technique used to examine the structure and composition of materials at the nanoscale. In TEM, a beam of electrons is transmitted through an ultra-thin specimen, interacting with the material, and generating images with extremely high resolution. This method provides detailed information about the sample's morphology, crystallography, defects, and more.

In the specific study conducted at the University of Lyon, the TEM analysis was carried out using the "TEM JEOL JEM2100" instrument. The key parameters evaluated were:

- *Accelerated electron voltage*: The electron beam's energy is measured in kilo-electronvolts (kV) and affects the penetration depth and interaction with the sample. In this case, an electron voltage of 200.00 kV was used.

- *Spatial resolution*: This refers to the ability to distinguish between closely spaced features in an image. The value of x50k indicates a spatial resolution of 50,000 times, enabling the visualization of fine details in the sample.

- *Operating modes*: The instrument was operated in two specific modes:

a) Electron Diffraction Mode: This mode is used to analyse the crystallographic structure of the sample by measuring the diffraction pattern of the transmitted electrons.

b) High-Resolution TEM (HR TEM) Mode: This mode allows for imaging with exceptionally high spatial resolution, revealing atomic-level details.

The preparation of the sample is a crucial parameter in TEM characterization. In this study, the sample preparation process followed these steps:

- A solution containing 2 ml of the particles under investigation and absolute anhydrous ethanol was created.
- The solution was subjected to ultrasonic treatment for 5 minutes in a sonication bath. This step aided in dispersing the particles within the solvent effectively.
- The prepared solution was deposited onto a silicon wafer.
- Subsequently, the solvent was allowed to evaporate, leaving the particles on the silicon substrate.

The combination of the JEOL JEM2100 TEM instrument and the meticulously prepared sample facilitated the acquisition of high-quality data, enabling a comprehensive analysis of the material's nanostructure and properties.

- XRD

XRD analysis serves as a key tool for identifying crystallographic phases within a sample and revealing its structural characteristics. This data is essential for comprehending material properties and behaviour. The XRD analysis was performed at the University of Lyon 1 using the "Two D8-Advance BRUKER" instrument with Bragg-Brentano Theta-Theta geometry.

In this experimental work, these following parameters are used:

- Fixed Distance: The X-ray beam was directed at the sample from a fixed distance of 4mm.
- Time Scale: The analysis was conducted over a time span of 8 minutes.

During the interpretation of the results two types of graphs are evaluated:

- I-2theta Graph: The intensity of diffracted X-rays was plotted against the 2theta angle. The 2theta angle values were evaluated from 5 to 45 degrees during the analysis. This graph helps identify crystallographic phases and their relative strengths.

- I-q Graph: The intensity of diffraction peaks was plotted against q values on the x-axis, ranging from 0.4 to 1.1. The q value is related to the scattering vector and provides information about the arrangement of atoms within the crystal lattice.

3.2.4 DSC/TGA

DSC and TGA are analytical techniques used to study the thermal behaviour of materials. In DSC, the sample and a reference material are subjected to controlled temperature changes, and the heat flow difference between the sample and the reference is measured. This helps in detecting phase transitions, such as melting points, crystallization, and glass transitions. On the other hand, TGA measures the weight change of a sample as a function of temperature or time. It's particularly useful for studying decomposition, oxidation, and other thermal stability-related processes.

All the analysis tests related to DSC/TGA characterization for this research were conducted at the DII (Department of Industrial Engineering) laboratories at the University of Padova. The instrument used was a "Mettler Toledo," capable of achieving temperatures up to a maximum of 1200°C. This temperature range was chosen to capture potential organic phase and water adsorbed loss in the powder, leading to mass reduction; in the case of commercial silica, water and organic phase are removed with a heat treatment at 900°C. The resulting analysis graphs are presented both in terms of mass loss and as a function of temperature. Additionally, analysing the derivative of the mass or heat flow curve with respect to temperature enables the evaluation of the glass transition temperature, which is a critical point indicating changes in the material's mechanical properties.

3.2.5 DLS

DLS is a technique utilized to investigate the size distribution of particles or molecules in a solution. It works by measuring the fluctuations in light scattering caused by the Brownian

motion of particles. This information helps to determine the hydrodynamic diameter of particles in a sample, which is crucial for understanding their behaviour, interactions, and overall stability.

In the context, DLS analysis was conducted using the "Malvern ZS nano DLS" instrument, equipped with the "Zeta-potential" module available at the Department of Department of Pharmaceutical Sciences at the University of Padua. Prior to performing DLS, it is imperative to have an ethanol/particle solution where the particles are well-dispersed. This aspect will be covered more comprehensively in Chapter 6, Paragraph 6.2.2.4.

For each sample, two key parameters were particularly determined:

- *Z-average*: known as the “intensity-weighted mean diameter”, it provides a representative measure of the particle size distribution.
- *Polydispersity Index (PdI)*: it quantifies the width of the size distribution. A lower PdI indicates a relatively narrow distribution, while a higher value suggests a broader distribution. The utilization of the "Malvern ZS nano DLS" instrument, in conjunction with the "Zeta-potential" module, allowed for accurate and insightful characterization of particle sizes and their distribution within the given solutions.

3.2.6 Drop Casting

The "drop casting" technique is a commonly employed method for depositing thin layers of materials, frequently in the form of powders or nanoparticles, onto a solid surface to produce thin films or coatings. With reference to the work in the literature [*93*], the drop-casting technique was developed, as illustrated in the following schematic:

- A powder suspension is prepared in ethanol: Given the lack of specific information regarding the quantities of powder and ethanol to be used, a total of 50 mg of powder is combined with 1 ml of ethanol. This quantity is deemed sufficient to enable the deposition of an adequately evaluable amount of powder.

- The deposition is initiated onto a cut quartz silica glass substrate, following thorough cleaning of the substrate. The drop-casting deposition proceeds as follows: With the glass slide positioned on a 90°C hot plate, the suspension of each sample is added drop by drop onto the glass, allowing for ethanol evaporation after each addition.
- Samples are subjected to thermal treatment at 700°C for 10 minutes, with a furnace heating rate of 10°C/min.

Upon the culmination of the procedure, purely visual comparative analyses are performed between the outcomes of the second step and those resulting from the thermal treatment.

The conducted analyses will be presented in Chapter 6, Paragraph 6.2.2.3.

3.2.7 Picnometer

Pycnometer is an advanced laboratory instrument used to measure the density of solid samples. It is known for its extreme precision in density measurements, making it ideal for scientific and engineering research applications. The instrument used is the "Antoon Paar Ultrapyc 3000 Gas Pycnometer", available in the Industrial Engineering Department of University of Padua.

The operation of the gas pycnometer involves inserting the solid sample into the instrument's measuring chamber. This sample must be carefully prepared to eliminate any air bubbles or impurities. Subsequently, inert gas, usually helium, is used to fill the chamber and pressurize the sample. Helium is chosen for its low molecular mass and its low reactivity with the sample. During the pressurization process, the volume of the sample undergoes a change, which is measured with extreme precision using a pressure sensor. These pressure and volume data are then used to calculate the density of the sample, following the ideal gas law. The result obtained represents the apparent density of the sample.

The Antoon Paar Ultrapyc 3000 offers several key features, including: wide range of operating temperatures and pressures, automation of many operations to reduce the risk of human errors and compatibility with a variety of sample shapes and sizes.

It is a highly precise and versatile instrument used for measuring the density of solid samples in laboratory environments. Thanks to its advanced features and reliability, it is widely used in engineering and scientific research for density studies and material characterization.

3.3 Conclusions

This chapter was entirely dedicated to explaining the processes and analyses used during the research. The main objective was to provide a clear understanding of the devices and techniques that played a fundamental role in the study.

In the first section, a detailed examination was made of the pressure generation systems used in the research, including the device for cold sintering, the Spark Plasma process, and the diamond anvil cell. For each system, a detailed explanation was provided regarding the materials involved, the mechanisms of pressure and temperature generation, and the sample preparation process. This section was designed to provide a solid foundation for understanding how these systems were employed in the context of the study.

In the second part of the chapter, emphasis was placed on characterization analyses. For each of these analyses, a brief introduction was provided explaining their general purpose. Subsequently, detailed descriptions were given of the usage procedures, the type of equipment used, and the key parameters involved in carrying out the analyses. These descriptions were developed to enable a comprehensive understanding of the characterization techniques and their specific applications within the study's context. Additionally, it was emphasized that if a specific characterization technique was used differently in subsequent chapters compared to what was described in this chapter, it would be duly highlighted, and the specific parameters used for that particular application would be described.

In summary, this chapter provides a solid foundation for understanding the devices and analyses that constitute the core of the research. A detailed knowledge of these processes and techniques is essential for interpreting and evaluating the results presented in the subsequent chapters of the thesis.

CHAPTER 4

Production of a silica glass starting by nanoparticles

The following chapter will discuss the production of a transparent glass using nanoscale silica particles. It will present the reasons and results of the characterization analyses conducted on the silica particles used. Based on this, the production methods of the glass will be analysed, focusing on the produced samples and their respective characterizations. The objective is to elucidate the results derived from this experimental investigation concerning the production of glass through an unconventional sintering technique.

4.1 *Commercial SiO_2 nanoparticles: chemical-physical properties*

The production of sintered glass involved commercial silica particles (*Sigma-Aldrich*) with the specifications listed in the Tab. 1

Table 1 Silica commercial powder - specifications

Product name	Silica, fumed - powder
Product number	S5130
CAS number	112945-52-5
MDL	MFCD00011232
Formula	O2Si
Formula weight [g/cm^3]	60,08
m^2/g (Surface Area)	370 - 420
pH (4% AQ Slurry)	3,8-4,3
Mesh Residue (325 Mesh Residue)	≤ 0,02%
Mean diameter [nm]	7

As the SiO_2 data sheet suggested, the SiO_2-T=25°C has adsorbed water and carbonate-bonded molecules on the powder surface. The presence of these linkages is attributable, with good reason, to the exposure of silica to the atmosphere, the influence of which is all the greater the smaller the particle size being analysed [*94*].

4.2 *Characterisation of particles: influence of heat treatments*

The unconventional sintering process that these nanometric silica particles have undergone is Spark Plasma Sintering (SPS). As explained in *Chapter 3- paragraph 3.1.2.2*, a fundamental requirement for the development of SPS using the Paris-Edinburgh press is the complete absence of a liquid phase, whether used as a binder for the particles or adsorbed on the surface.

In order to eliminate the adsorbed water and carbonates, thereby increasing the purity of the powder being used, various heat treatments were carried out at different temperatures. This allowed an estimation of the amount of water and carbonates existing in the initial powder to be obtained.

After performing the heat treatments, the powders, treated at different temperatures, will undergo characterization analysis to evaluate the optimal conditions for the Spark Plasma process. This analysis aims to assess the chemical and physical properties of the powders and determine the effects of the heat treatments on them. By analysing the results, it is possible to better understand the development conditions required for the Spark Plasma process.

4.2.1 *Preliminary heat treatments*

Heat treatments were conducted using an oven of the type "Landcal Blackbody Source-Type P1600B". The percentage reduction in mass was determined in relation to the previous mass of the heated powder at various treatment temperatures: 200, 500, 700, 900, and 1000°C. Each heat treatment followed a heating/cooling rate of 10°C per minute, and the powder was held at the desired temperature for a duration of 2 hours. Tab. 2 presents the percentage weight loss observed during each temperature increment.

Table 2 Thermal treatments: weight loss in function of temperature

T [°C]	25	200	500	700	900	1000
Δ [%]	0	19,12	0,39	0,91	3,6	3,28

From the provided table, a progressive decrease in powder mass can be observed as the temperature increases. A significant reduction is achieved when heating the silica to 200°C,

where the 19.12% decrease indicates the amount of evaporated water present in the initial powder. The mass loss continues to occur in exceedingly small quantities until reaching 900°C, at which point the organic groups are also eliminated.

At the end of the heat treatment at 900°C, an overall decrease of 24.02% is observed, resulting from the combined contribution of water and carbonate organic group (CO_3^{--}) elimination.

In order to assess whether the removal of organic groups was fully completed at 900°C, a heat treatment at 1000°C was performed. As can be seen, the treatment of the powder at a hundred degrees higher has a minimal impact on the mass loss (17,3%)

Therefore, the elimination of organic groups can be considered complete at 900°C.

4.2.2 *Characterisation analysis*

The following paragraph will provide a detailed description of the characterization analysis procedures and present the results obtained.

4.2.2.1 *Raman spectroscopy*

SiO_2-T=25°C and SiO_2-T=900°C are submit to Raman spectroscopy. By analysing the vibrations of the bonds in the constituent molecules, it is possible to assess the differences and the influence of the thermal treatment. Several measurements were performed to obtain a Raman vibrational spectrum but due to the high diffusivity of the powder [*95*] in Tab. 3 only the parameters that give the best results are reported.

Table 3 Raman spectroscopy technical data

	SiO_2 - T=25°C	**SiO_2 - T=900°C**
Acquisition time (s)	30	600
Accumulations	2	1
Instrument	labRAM HR Evol.	ARAMIS
Objective	x50 Lwd	x50 LMP
Laser (nm)	Green 532	Cobalt 473
Spectrum (cm^{-1})	905,075	2000,06
Filter (%)	100	100

The best results are obtained under different analysis conditions: powders treated at 900°C are influenced by green light, which gives rise to the development of great diffusivity; this prevents a vibration spectrum from being obtained in which the constituent bonds of the molecules can be recognised. [*95*]

Secondly, the best condition for obtaining an acceptable spectrum for powders treated at T=900°C is the development of the test in a longer time. A longer acquisition time allows a higher spectral resolution to be obtained, enabling a better distinction of subtle spectral features; in addition, it allows better signal averaging and noise reduction, improving the spectrum quality.

Fig. 1 and Tab. 4 show the resulting Raman vibrational spectrum from the characterization analysis and the correspondence between each peak to the referred vibration mode.

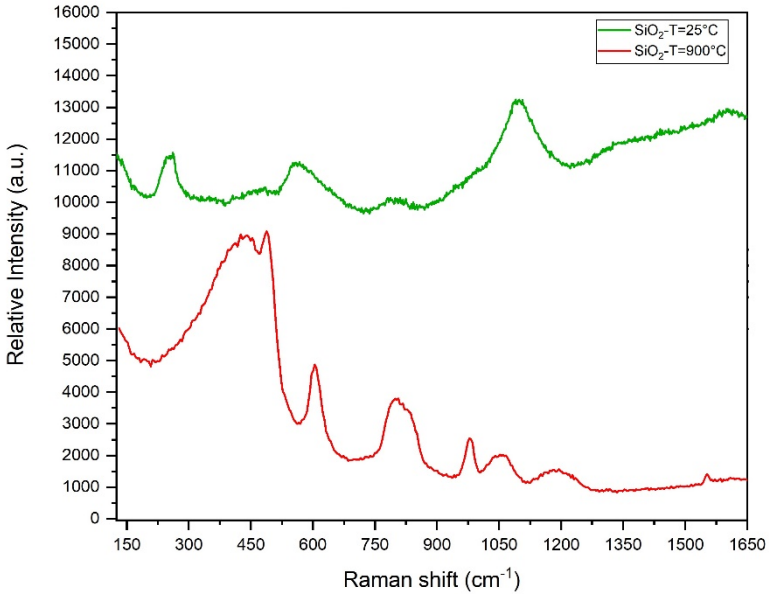

Figure 1 Raman spectra: comparison between untreated and treated powder

Table 4 Assignment of Raman vibrational modes

Raman shift (cm^{-1})		**Band assignment**
SiO_2-T=25°C	**SiO_2-T=900°C**	
455,526	456,415	Si-O-Si rock.
551,845	492,242	3-fold-rings
612,59	605	4-fold rings
792,321	798,949	Si-O-Si bend.
986,605	*976*	Si-OH
1101,73	1165,67	Si-O-Si stretch.
1588,7	-	CO_3^{--}

From Tab. 4, a good correspondence between the analysed powders and a typical silica glass' peaks can be noticed; however, differences can be identified between the two samples at the two different exposure temperatures.

Treating silica at T=900°C, as assumed earlier in the heat treatment analysis, results in the disappearance of the carbonate bond and the presence of a weak signal at the bond vibration between silica and hydroxyl group. Although the operation was conducted at a temperature that assumes complete evaporation of water, and despite the silica powders being placed in

a vacuum-sealed box, the presence of water observed can be accredited to atmospheric exposure during the sample's transportation and testing phase.

4.2.2.2 *DAC in situ Raman spectroscopy*

Following the heat treatment, the SiO_2-T=900°C powders were subjected to an in-situ analysis using Raman spectroscopy with the Diamond Anvil Cell (DAC) technique. The DAC, prepared accordingly to [*96*], was connected to the labRAM spectral acquisition instrument, as shown in Fig 2.

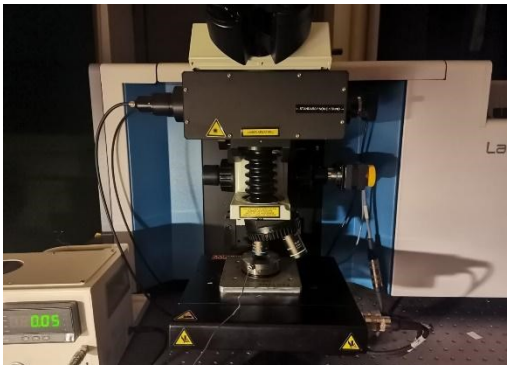

Figure 2 DAC in situ with Raman spectroscopy - connection

During the experimental procedure, the pressure within the cell was elevated from 0.05 bar to 23.61 bars. As described in *Paragraph 3.2,3.2*, the presence of ruby in the cell allows for the determination of the internal pressure achieved within the cell. This is made possible by identifying the wavenumber corresponding to the bonding bands that characterize the Raman spectrum of the ruby itself. As predicted in the literature [*97*], an increase in the pressure applied to the cell membranes leads to a rightward shift in the ruby's bands (Fig. 3).

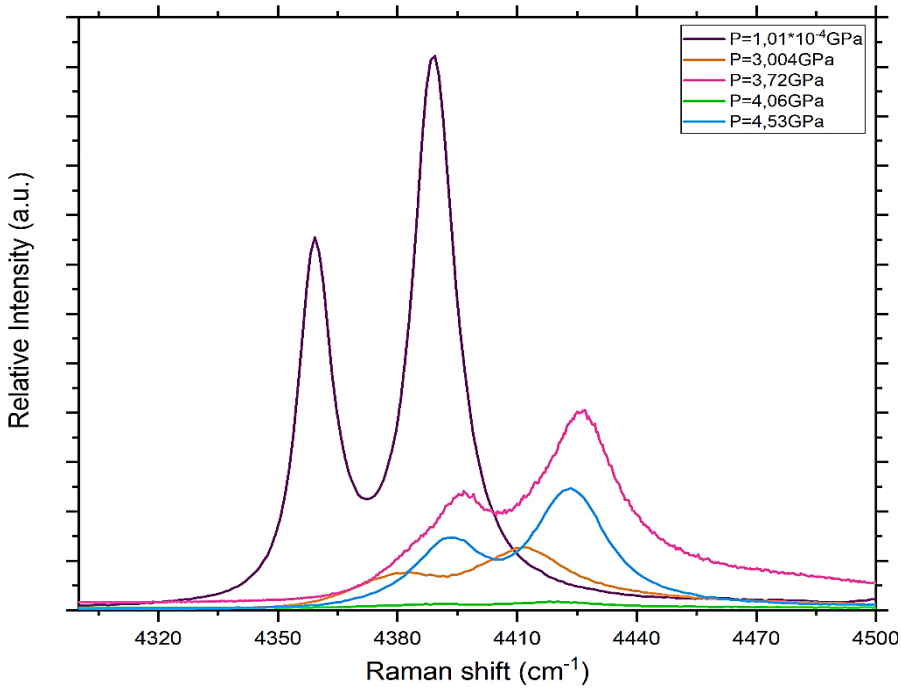

Figure 3 Raman Spectra of ruby at different pressures

Subsequent calculations that establish a relationship between the wavenumber of the bands and the internal pressure provide values for the internal pressure, which are presented in Tab. 5. The table displays the correlation between the pressure of gas (bar), the wavenumber of the main band, and the internal pressure (GPa).

Table 5 Identification of internal pressure of the cell on the base of ruby Raman shift

Pressure of gas [bar]	**Raman Shift [cm^{-1}]**	**Pressure in cell [GPa]**
0,05	4394	0,66
13,1	4402,3	1,76
16,01	4405,61	2,2
19,01	4411,58	3,004
22,03	4419,47	4,06
23,61	3323	4,53

In addition to acquiring Raman spectra of ruby, which are essential for evaluating the internal pressure, Raman spectra of the powder were also obtained for each pressure level reached. The analysis was conducted in two stages: initially, the pressure was incrementally increased,

and the behaviour of the powder under progressively higher pressures was evaluated. After a couple of days, while maintaining the cell under pressure, spectroscopic analysis was performed once again.

In the subsequent stage, in accordance with fundamental physical principles, it was observed that the pressure did not remain at its maximum value (4.53 GPa), but instead decreased to 3.72 GPa. Through deconvolution analysis was possible to attribute peaks in the spectrum to different bond vibrations.

Fig.4 illustrates the spectra obtained at different pressure levels, while Tab.6 presents the correspondence between wavenumbers and bond vibrations.

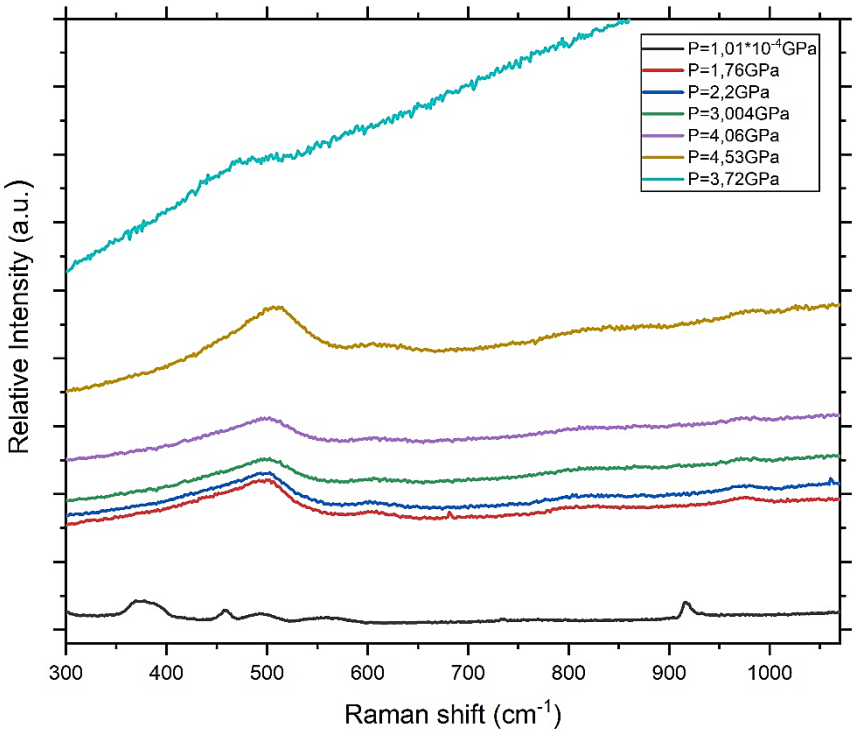

Figure 4 Raman spectra of SiO2-T=900°C at different pressures

Table 6 Assignment of Raman vibrational modes of SiO2-T=900°C at different pressures

	Pressures values [GPa]						
	1,76	*2,2*	*3,004*	*3,72*	*4,06*	*4,53*	*Band assignment*
Raman shift [cm^{-1}]	455,221	457,793	458,601	458,98	492,002	494,872	Si-O-Si rock.
	493,166	498,395	502,72	503,113	503,48	505,11	3-fold-rings
	599,348	602,327	605,315	606,814	608,03	612,917	4-fold rings
	786,164	801,37	801,4	801,4	801,59	814,948	Si-O-Si bend.
	974,767	976,426	976,872	978,416	981,397	984,712	Si-OH
	Not visible						Si-O-Si stretch.

The figure and table demonstrate a rightward shift of the peaks associated with the vibration bands of the bonds characterizing silica. Although the shift is minimal with each increase in pressure, there is a noticeable overall difference between atmospheric pressure and the maximum pressure reached. Furthermore, the relative intensity of each curve increases as the pressure rises.

However, it is important to note that the figure shows an apparent anomaly concerning the pressure release. The light blue line corresponding to p=3.72 GPa does not adhere to the pressure-conditions, as it does not fall between the lines for P=3.004 - 4.06 GPa.

This discrepancy arises because the labRAM spectrophotometer used to acquire the previous spectra failed to detect the spectrum related to the discussed pressure. For this reason, the pressure spectrum P=3.72GPa was conducted using a home-made Raman spectrophotometer, which has higher power than the LabRAM spectrophotometer used for the previous tests (7.14mW vs. 4.23mW). The differing relative intensity values observed in the graph can be attributed to variations between the two spectrophotometers used. This divergence is the reason for the lack of correspondence between the expected pressure/intensity relationship and the values depicted in the graph; the use of different spectrophotometers, indeed, can introduce variations in sensitivity, calibration, and instrument-specific factors that influence the measured intensity values.

4.2.2.3 *XRD*

XRD analysis was developed on the following samples: SiO_2-T=900°C, SiO_2-T=1000°C and bulk silica glass; the latter, analysed in [*98*], is used as a reference to assess on the one hand the accuracy of samples spectra trends, on the other hand the similarities/differences that nanostructured silica might show. Fig. 5 show the spectra obtained from the XRD analysis; Tab. 6 shows the statistical analysis conducted considering the I-q graph.

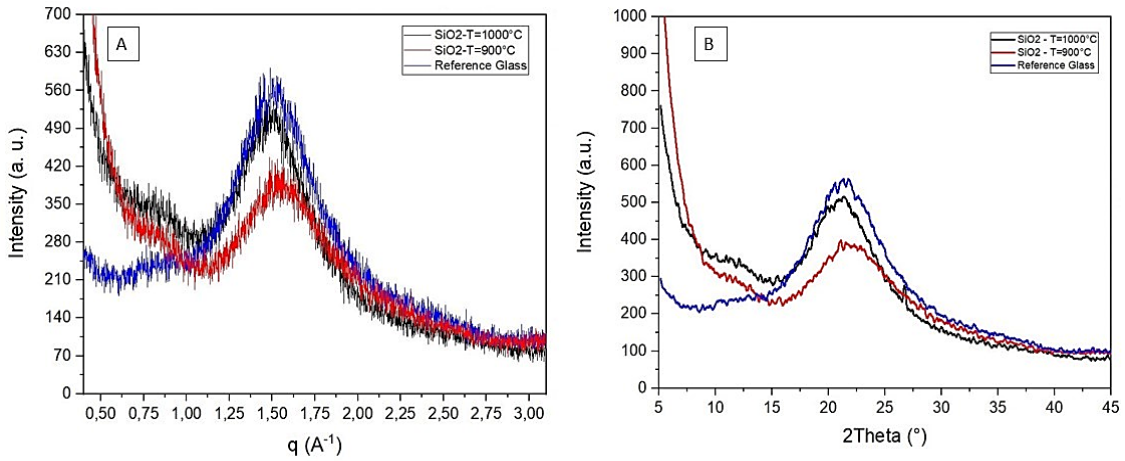

Figure 5 (A) I-q diagram (B) I-2theta diagram of treated and bulk silica

Table 7 I-q graph -- statistical analysis

	Area	**% Area**	**FWHM**	**Left Half Width**	**Right Half Width**	**Centre of gravity**
SiO_2-T=1000°C	332,52	58,203	0,51814	0,24847	0,26967	1,63217
Glass Reference	438,53	89,752	0,52207	0,23531	0,28678	1,51654
SiO_2-T=900°C	270,86	52,736	0,52007	0,20383	0,31265	1,68245

Fig. 6 shows the following more clearly:

- The spectra of SiO_2-T=900°C and SiO_2-T=1000°C have similar trends to the reference bulk silica glass ones: they show a broad band peak at 2theta=22.45°, which is attributed to Si-O-Si bonding. This is an unsharp peak with a full width at half maximum (FWHM value) close

to 0.52; this value indicates an amorphous phase distribution that characterises the molecular aggregation systems for all the samples.

- The SiO_2-T=1000°C sample shows the clear presence of a sharp peak at 2theta=26.77°.

With the aim of investigating the presence of this peak, which is attributable to a crystalline phase, analyses were conducted to identify what is shown in Fig. 7.

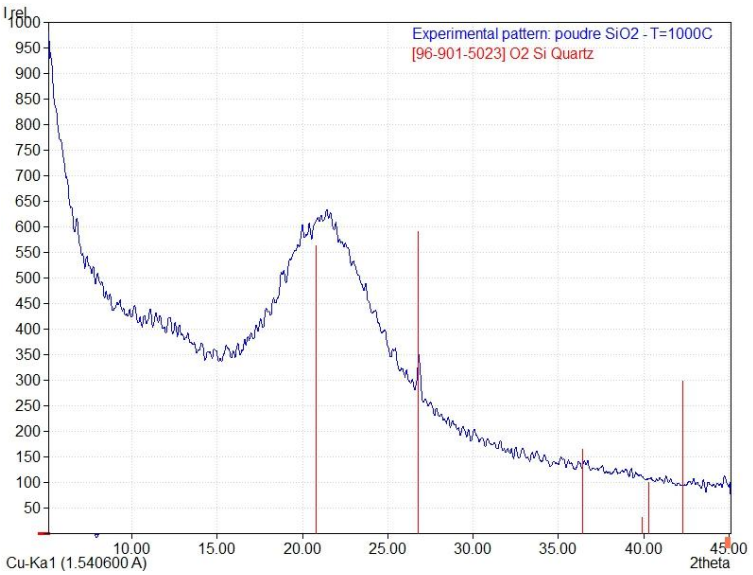

Figure 7 I-2theta diagram of SiO2-T=1000°C - peaks analysis

It is possible to derive that what is shown a particular type of quartz: evaluated only in a theoretical way and reported in [*99*], it is the unique element which has peaks in perfect conformity with the analysed powders.

Based on the provisional obtained results, it can be concluded that the thermal treatment at 1000°C applied to nanostructured silica results in the formation of an unintended crystalline phase, which is undesirable to produce glass.

The experimental results indicate that subjecting the nanostructured silica to a heat treatment at such an elevated temperature leads to a transformation of the material's atomic arrangement, causing the formation of crystalline structures instead of a vitreous state. This deviation from the desired glassy phase can be attributed to the specific thermodynamic conditions imposed during the thermal treatment process.

4.2.2.4 *TEM*

TEM analysis was carried out on silica powders subjected to three different exposure temperatures: 25, 900, 1000°C; it aims to assess the change in size brought about by the heat treatments, the way the particles are disposed in the space and the diffraction pattern.

Below are the results obtained for each of the three types of powder.

- SiO_2-T=25°C

Fig. 7 shows the image visualised by microscopy: the particles are well-defined (B), and the absence of clear diffraction rings (C) indicates the absence of crystalline phase in the analysed powders.

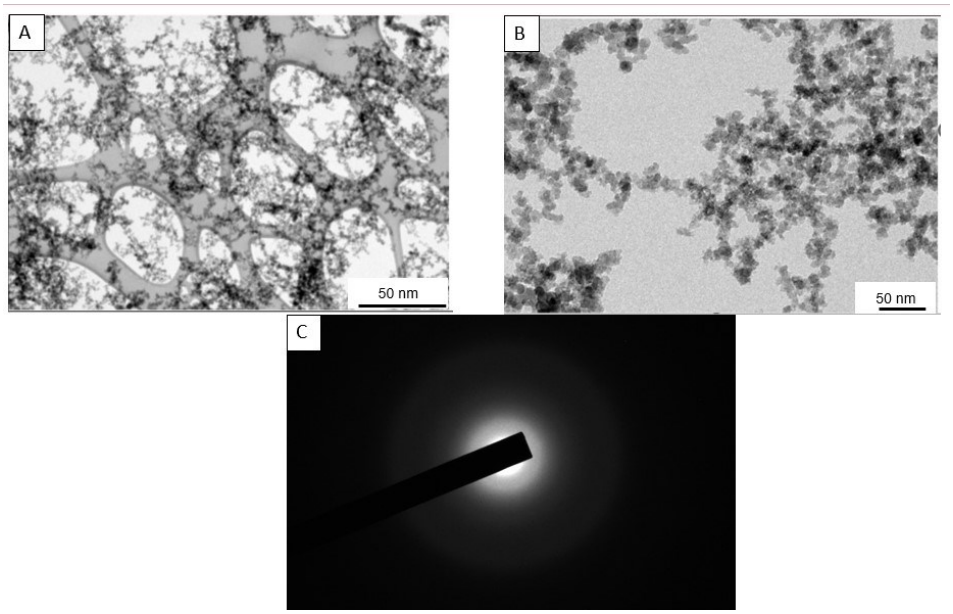

Figure 7 TEM images of SiO2-T=25°C: (A) e (B)microscopical images; (C) diffusion pattern

The evaluation of particle size was conducted by statistical analysis; the parameters evaluated, and the mathematical distribution of particle size are shown in Tab. 7-8 and Fig. 8, respectively.

Table 8 Statistical distribution analysis - SiO2-T=25°C

Bin Centers	Counts	Cumulative Sum	Cumulative Percent
3,5	5	5	1,60256
4,5	26	31	9,9359
5,5	56	87	27,88462
6,5	75	162	51,92308
7,5	72	234	75
8,5	42	276	88,46154
9,5	26	302	96,79487
10,5	9	311	99,67949
11,5	0	311	99,67949
12,5	1	312	100

Table 9 Statistical analysis - SiO2-T=25°C

Mean Diameter (nm)	St. Deviation	Maximum	Minimum
6,979	1,568	12,900	3,334

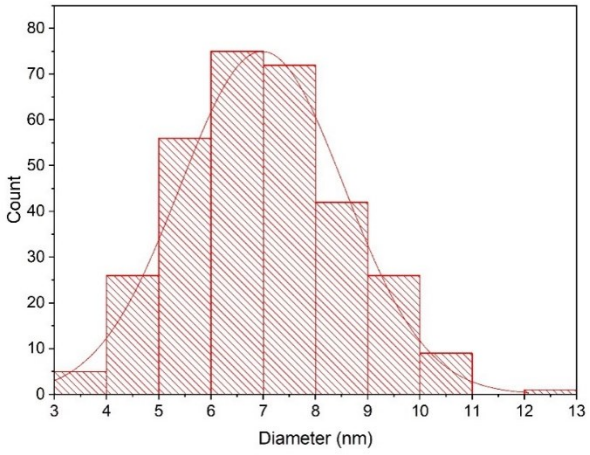

Figure 8 Normal particle size distribution - SiO2-T=25°C

The statistical analysis conducted confirms what the silica manufacturer has provided regarding its size: the average diameter of non-heat treated SiO_2 is 7nm.

- SiO_2-T=900°C

Fig. 9 shows the image visualised by the microscopy: the particles are well-defined (B), and the absence of clear diffraction rings (C) indicates the absence of crystalline phase in the analysed powders.

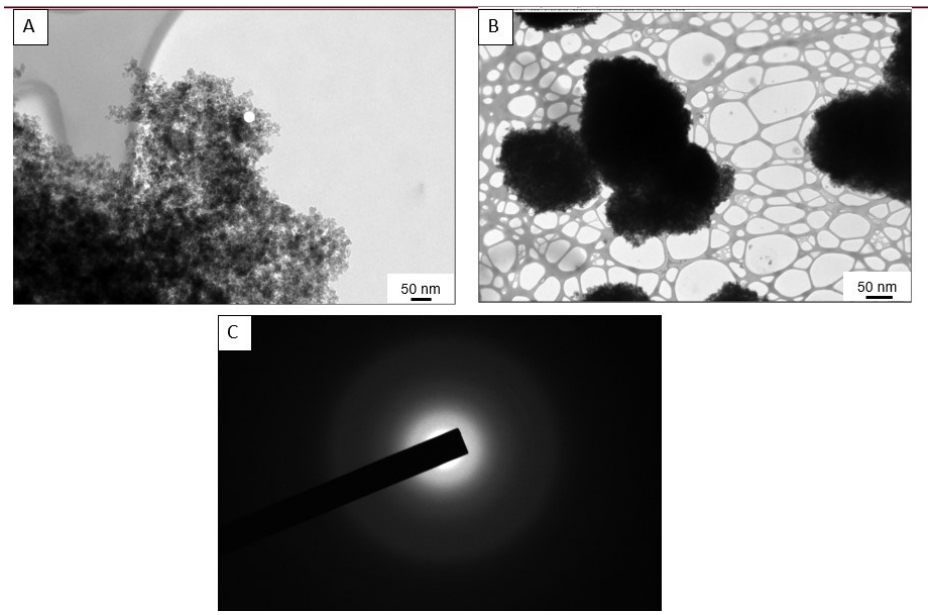

Figure 9 TEM images of SiO2-T=900°C: (A) e (B)microscopical images; (C) diffusion pattern

The evaluation of particle size was carried out by means of statistical analysis; the parameters evaluated, and the mathematical distribution of particle size are shown in Tab. 9-10 and Fig. 10, respectively.

Table 10 Statistical distribution analysis - SiO2-T=900°C

Bin Centers	Counts	Cumulative Sum	Cumulative Percent
7	1	1	0,32154
9	12	13	4,18006
11	41	54	17,36334
13	57	111	35,69132
15	55	166	53,37621
17	60	226	72,66881
19	36	262	84,24437
21	31	293	94,21222
23	13	306	98,39228

25	4	310	99,67846
27	0	310	99,67846
29	1	311	100

Table 11 Statistical analysis - SiO2-T=900°C

Mean Diameter (nm)	St. Deviation	Maximum	Minimum
15,833	3,822	29,556	5,366

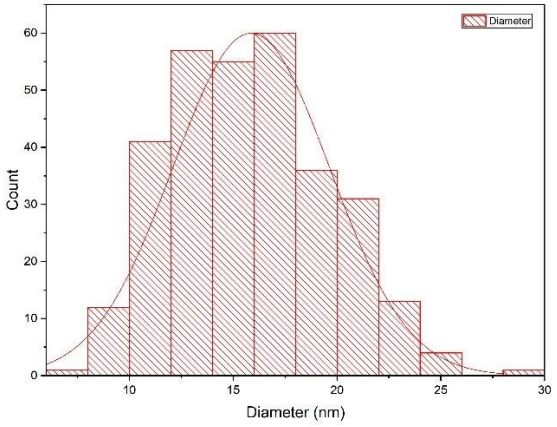

Figure 10 Normal particle size distribution - SiO2-T=900°C

When heat-treated at T=900°C, the silica particles undergo an increase in the size of their diameter of double that of the initial particle, but still remains in the nanometric range; the average diameter is around 15nm.

- SiO_2-T=1000°C

Fig. 11 shows the image visualised by the microscopy: the particles are well-defined (B), and the absence of clear diffraction rings (C) indicates the absence of crystalline phase in the analysed powders.

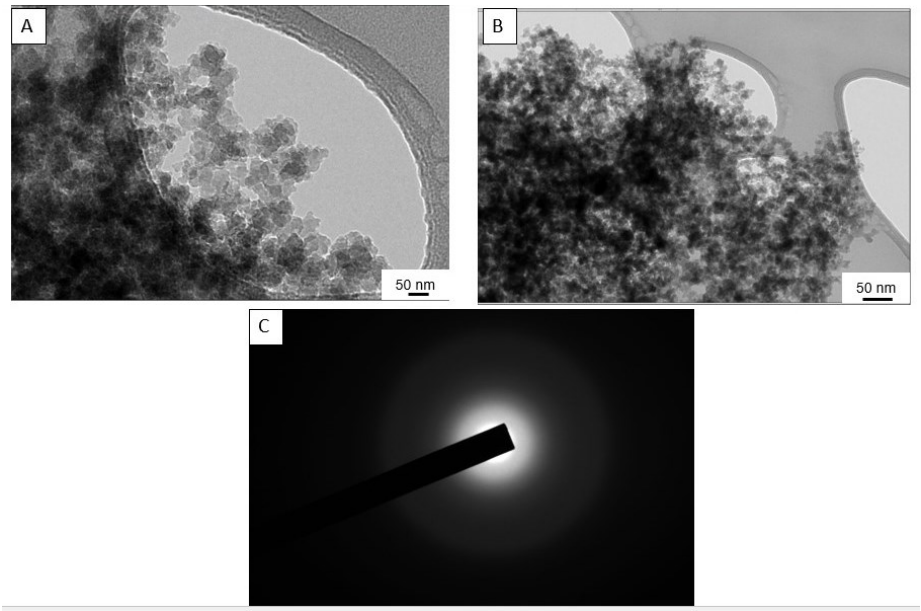

Figure 11 TEM images of SiO2-T=1000°C: (A) e (B)microscopical images; (C) diffusion pattern

The evaluation of particle size was conducted by means of statistical analysis; the parameters evaluated, and the mathematical distribution of particle size are shown in Tab. 11-12 and Fig. 12, respectively.

Table 12 Statistical distribution analysis - SiO2-T=1000°C

Bin Centers	Counts	Cumulative Sum	Cumulative Percent
7	3	3	0,96154
9	13	16	5,12821
11	11	27	8,65385
13	34	61	19,55128
15	61	122	39,10256
17	54	176	56,41026
19	40	216	69,23077
21	30	246	78,84615
23	22	268	85,89744
25	21	289	92,62821
27	7	296	94,87179
29	6	302	96,79487
31	6	308	98,71795
33	3	311	99,67949
35	0	311	99,67949
37	1	312	100

Table 13 Statistical analysis - SiO2-T=1000°C

Mean Diameter (nm)	St. Deviation	Maximum	Minimum
18,060	5,261	36,371	6,339

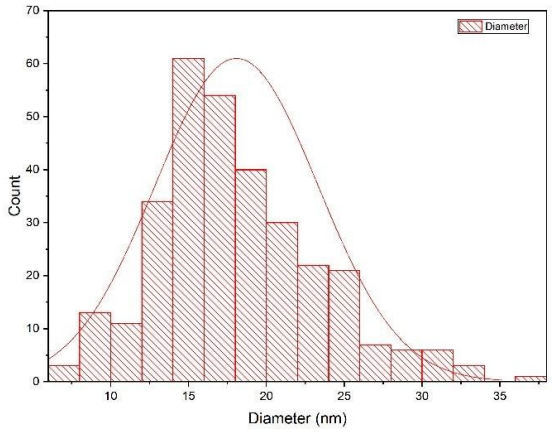

Figure 12 Normal particle size distribution - SiO2-T=1000°C

The powders treated at T=1000°C undergo a slight increase in size compared to the previous ones treated at a lower temperature; the average diameter is 18 nm.

In conclusion, it can be stated that temperature influences particle size: a temperature that leads to the evaporation of water and the removal of organic compounds induces a significant increase in size compared to their initial value; a further increase in temperature, however, has less impact in influencing particle size.

4.2.2.5 *SEM*

SEM analysis was performed on silica powder treated at 900°C and pre-compacted under Spark Plasma pre-development conditions. The resulting pellet exhibited the following properties:

- Mass: 102.7 mg
- Cylindrical dimensions: 7 mm in diameter, 3 mm in height
- Compaction: 175 MPa

The SEM analysis results are reported in Tab. 14, and the images obtained from the analysis are shown in Fig 13.

Table 14 SEM parameters; SiO2-T=900°C compacted at 175 MPa

	A	**B**
FoV [um]	500	5
WD [mm]	5,14	5,14
Speed	4	3
BC [pA]	22	22
Det	E-T	E-T
Scan Mode	UH-RESOLUTION	UH-RESOLUTION
Energy [keV]	2	2
Mag [kx]	558	55,8
Pixel size [nm]	488	4,88
Spot size [nm]	3,20	3,20

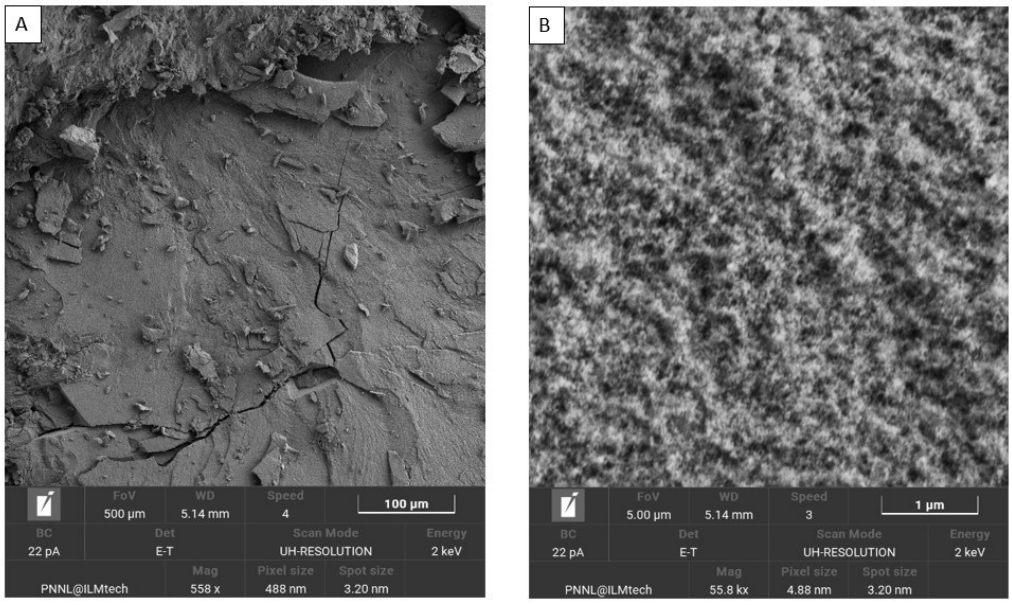

Figure 13 SEM images: SiO2-T=900°C compacted at 175MPa; (A) complete pellet area, (B) zoom on a specific area

The particle's surface appeared to be non-uniform, indicating delamination during the production phase.

In conclusion, the SEM analysis data confirms the presence of surface irregularities of the silica powders treated at 900°C, which are crucial considerations for the Spark Plasma process under investigation.

4.3 *Glass production by cold sintering process*

This paragraph aims to examine their response when subjected simultaneously to variations in both pressure and temperature. Specifically, the behaviour during the cold sintering process will be evaluated. This aspect is comprehensively explored in Chapter 3, Section 3.1.1, where the process development procedure is detailed. Subsequently, the fundamental characteristics of this process will be presented, with a focus on the significance of the involved parameters and the optimization strategies employed.

In the latter part of the paragraph, the outcomes of the characterization analyses conducted on the samples will be presented. Special emphasis will be placed on accurate density measurements, as well as on the visual interpretation of results and micrographic analysis.

4.1.1. Experimental work

The cold sintering of nanostructured silica has been developed, producing a single sample characterized by the following parameters: solution molarity of 15M, T=200°C, liquid phase equal to 20% of the solid phase, and powder residence time in the mould set at 60 minutes. The choice of these parameters is based on the results obtained in a previous time-scale study of cold sintering of commercial borosilicate powder. Referring to Chapter 5, Section 5.4.2, the parametric conditions of molarity, liquid phase, and temperature are the ones that yield a higher relative density compared to other parameter combinations. Assuming that this evaluation holds true for nanostructured silica in CSP as well, the same parameter combination was retained compared to borosilicate glass, while reducing (by half) the value of the residence time.

It is important to note that the amount of powder used is lower than what would be theoretically required. The utilized mass was 0.165g, approximately one-third of the value estimated based on the theoretical density of silica glass (2.2 g/cm^3) and the mould volume

(Chapter 3, Section 3.1.1.1). The use of a smaller mass was necessary due to the properties of nanostructured silica. This material exhibits significantly higher porosity and much lower apparent density compared to non-nanostructured silica [*100*]; therefore, a smaller mass is needed to achieve the same volume as non-nanostructured silica.

4.1.2 Characterisation of samples

The nanostructured silica wafer produced under the previously described conditions exhibited immediate instances of delamination and fracture upon removal from the mould. However, it is important to clarify that the fracture is not solely attributed to the inherent brittleness of the silica wafer. While silica is known for its inherent brittleness [*101*], it's worth noting that due to the high volatility of the material itself, the act of removing it from the mould necessitated the use of tools (such as a manual hammer) to facilitate the definitive separation of mould components.

Following the removal from the mould, the wafer underwent a drying process at a temperature of T=60°C for a period of t=24 hours. This treatment was undertaken to facilitate the removal of water, stemming not only from the liquid phase employed in the CSP process but also from the ultrasonic bath to which the mould was initially subjected in an attempt to extract the wafer.

Upon the conclusion of this operation, from a purely observational standpoint, the wafer presents itself as extremely thin and characterized by transparent regions. These observations might suggest that the primary objective of the experimentation could potentially be achieved through the application of increased pressure, higher temperatures, or, in general, a more optimal combination of parameters while continuing to develop the cold sintering process.

4.1.2.1 Density measurements

In order to ascertain whether the sintering process had been fully completed at the conclusion of the process development, the Archimedes' test was conducted to estimate the relative density of the obtained sample. The reference theoretical density utilized for comparison was that of bulk silica glass, which is 2.2 g/cm³ [*102*].

The Archimedes' test revealed a relative density value of 92.64%. The inability to attain the maximum density value suggests an incomplete sintering process. This situation could be

attributed to an insufficient residence time employed to facilitate sintering or to an inadequately chosen combination of parameters. It is important to highlight that while the developed process has the potential to yield transparent glassy pellets of nanostructured silica, achieving this objective necessitates the optimization of parameters and therefore requires a more comprehensive study.

To assess the impact of higher pressures and temperatures, the experimentation conducted through the Spark Plasma Sintering (SPS) process is presented below.

4.4 Glass production by Spark Plasma Sintering Process

The sintering process for Spark Plasma was conducted from SiO_2-T=900°C powders, which the best in the characterisation analysis (high purity, good compression behaviour, nanometric size, and absence of crystalline regions).

Two samples were produced through the procedure operations described in Chapter 3 in the process development section using the Paris-Edinburgh type press. It was decided to conduct the process in such a way that only the effect of temperature was evaluated: pressure and mould dwell time were thus kept constant, 2GPa and 3min respectively; the process temperature was 1000°C for the first test and 800°C for the second.

The details of the operations, the results obtained for each sample and the sample characterization analysis are presented below.

4.4.1 Experimental work

- SiO_2-T1000P2

The sample is produced according to the parameters presented in Tab.15

Table 15 SPS process parameters: SiO2-T1000P2

Compression			
Compressed pellet mass [mg]	102,7	*Oil pressure [bar]*	200

Pressure in pre-compacted pellet [MPa]	175	*Oil pressure rate [bar/s]*	0,17
Sintering			
Temperature		**Electric Current**	
Setup Temperature [°C]	1000	*Tdown*	1
Dwell time [min]	3	*Tup*	2
Heating speed [°C/min]	100	*N. Pulses (ON)*	12
Cooling speed [°C/min]	490	*N. Pulses (OFF)*	2

A pre-compacted powder pellet weighing 102.7 mg underwent sintering using the Spark Plasma technique, with an internal pressure of 2 GPa and a process temperature of 1000°C. The choice of a temperature slightly below the glass transition temperature of silica served as the starting point for the research operations. The pellet was held under the conditions for 3 minutes, after which the pressure was decreased at the same rate of increment, while the temperature was rapidly lowered.

During the operations, in-situ measurements allowed for the acquisition of the graphs shown in Fig. 14.

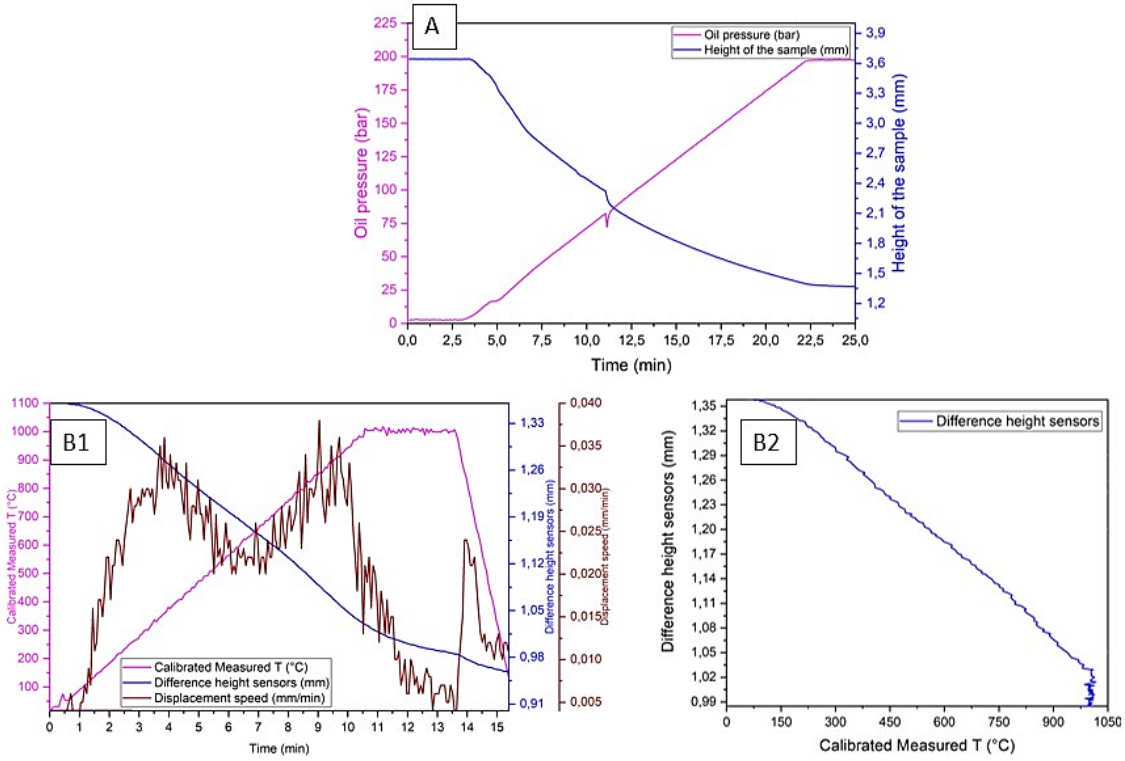

Figure 14 Graphs from in situ measurements at the sintering process for Spark Plasma - (A) compression step, (B1) and (B2) sintering cycle – SiO2-T1000P2

During the compression phase (A), the pressure gradually increases over time in a linear mode. However, at t=11.261 minutes, a slight decrease in pressure occurs, resulting in a reduction in the rate of decrease of the sample height. This occurs when the sample height reaches 2.2 mm. For longer durations of the compression process, both the pressure and the sample height exhibit a consistent pattern of increase and decrease, respectively, without any noticeable anomalies.

The sintering phase (B1) progresses without anomalies in terms of temperature increase and power development (measuring 385.74W). Sensors detect a gradual decrease in the sample's height due to particle aggregation, the formation of necks between particles, and a corresponding decrease in porosity. The displacement velocity, however, exhibits two distinct peak values at the following points:

- t=3.84 min, T=359.414°C, v=0.036mm/min

- t=9.046 min, T=856.001°C, v=0.038 mm/min

This observation suggests that the actual sintering phase begins at lower temperatures, particularly at the temperature corresponding to the absolute maximum peak (around 800°C). However, the initial stage of sintering may occur at significantly lower temperatures (around 400°C).

Moreover, Fig. 14-B2 reveals that the sintering process does not seem to reach completion at the conclusion of the temperature holding period at 1000°C. The disparity in sensor height diminishes smoothly until reaching 1.02 mm, but then it remains constant, creating a region with a height difference of 0.03 mm where no further height reduction, and therefore sintering progression, has taken place.

The sample at the end of the process appears as shown in Fig. 15.

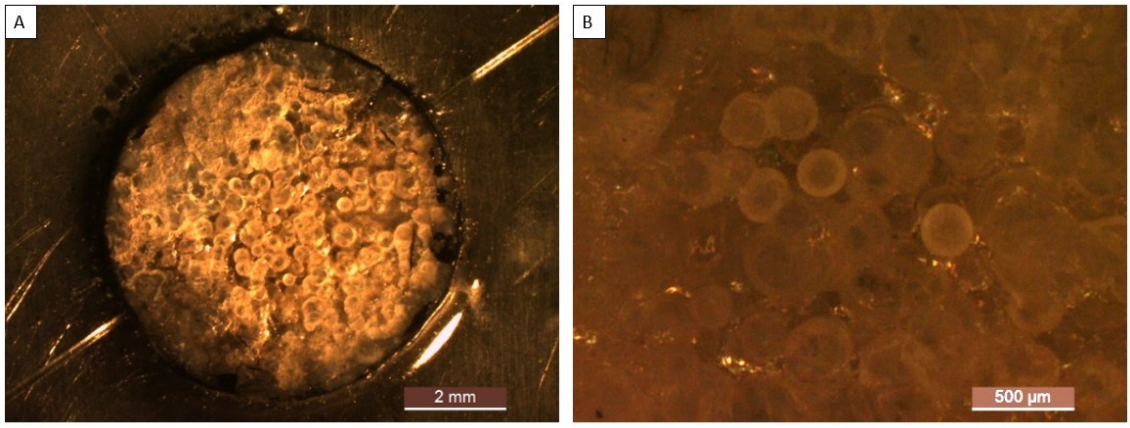

Figure 15 Optical microscope images –(A) entire pellet (B) Focusing on a surface region-- SiO2-T1000P2

The sample, subjected to graphite removal using sandpaper and polishing, exhibits a surface under the microscope that is not smooth. Instead, it consists of distinct areas that reflect light but are difficult to identify and interpret with certainty. Further characterization analyses, which will be explained later in this chapter, will provide an explanation for the observed phenomenon.

- SiO_2-T800P2

Considering that sintering occurs at T=800°C in the developed sample, it has been decided to implement the SPS (Spark Plasma Sintering) process while keeping the pressure and dwell time constant. The only variable being changed is the temperature, which is set precisely at 800°C. The detailed parameters are presented in Tab 16.

Table 16 SPS process parameters: SiO2-T800P2

Compression			
Compressed pellet mass [mg]	40	*Oil pressure [bar]*	200
Pressure in pre-compacted pellet [MPa]	37	*Oil pressure rate [bar/s]*	0,17
Sintering			
Temperature		**Electric Current**	
Setup Temperature [°C]	800	*Tdown*	1
Dwell time [min]	3	*Tup*	2
Heating speed [°C/min]	100	*N. Pulses (ON)*	12
Cooling speed [°C/min]	390	*N. Pulses (OFF)*	2

A pre-compacted powder pellet weighing 40 mg underwent sintering using the Spark Plasma technique, with an internal pressure of 2 GPa and a process temperature of 800°C. The pellet was held under conditions for 3 minutes, after which the pressure was decreased at the same rate of increment, while the temperature was rapidly lowered.

The sample under examination presents noticeable differences compared to the previous one. The process was developed starting from a pre-compacted powder tablet with significantly reduced mass. The high specific volume and the fragile nature of the nanostructured silica pose challenges in the production step of the tablets. Difficulties are particularly encountered during the extraction phase of the tablet from the mould, resulting in both breakage and delamination phenomena. This condition makes it difficult to obtain smooth surfaces on both cylindrical base sides, which are essential for the Spark Plasma Sintering process using the Paris-Edinburgh press. In the sample under examination, these difficulties were clearly observed. Various unsuccessful attempts were made to develop alternative methods of creating the tablet. Consequently, the process was adapted with a much lower mass than the

actual requirement, and the powder used for the tablet was pre-compacted at lower pressures compared to the SiO_2-T1000P2 sample.

During the operations, in-situ measurements allowed for the acquisition of the graphs shown in Fig. 16.

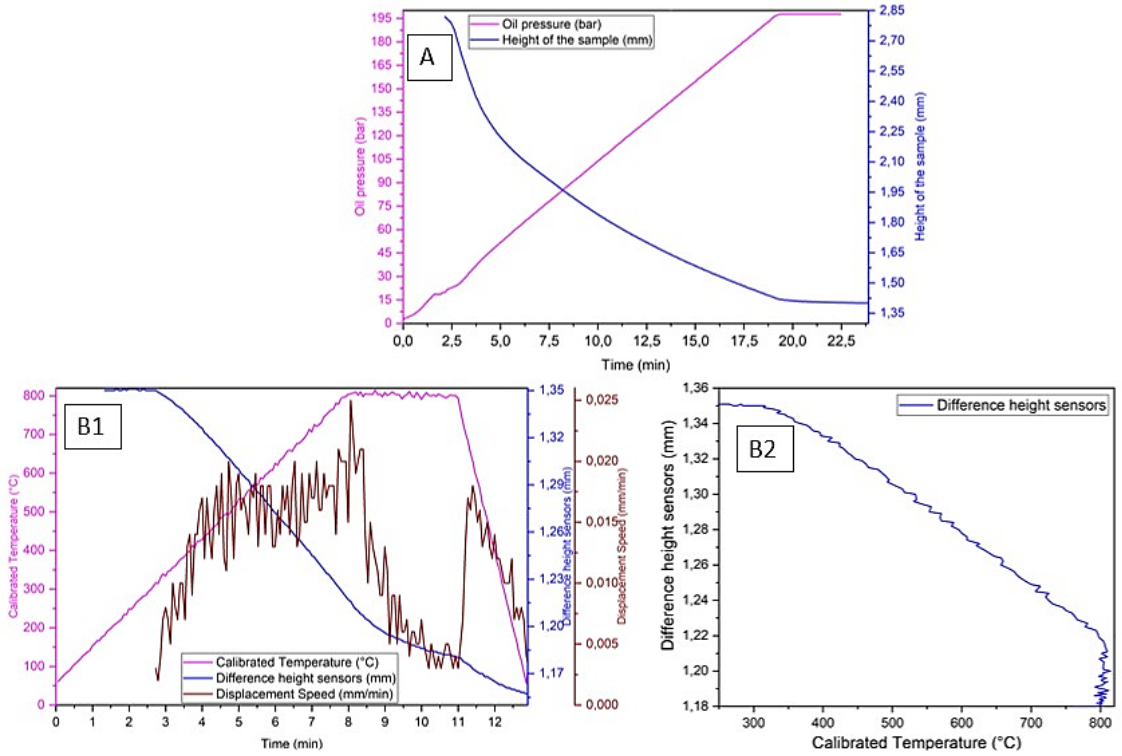

Figure 16 Graphs from in situ measurements at the sintering process for Spark Plasma - (A) compression phase, (B1)-(B2) sintering phase – SiO2-T800P2

During the compression phase (A), the pressure gradually increases over time in a linear fashion, without any noticeable anomalies.

The sintering phase (B1) progresses without anomalies in terms of temperature increase and power development (measuring 306,83W). However, sensors detect a gradual decrease in the sample's height due to particle aggregation, the formation of necks between particles, and a corresponding decrease in porosity. The displacement velocity, however, exhibits a clearly peak value at the following point:

t=8.062 min, T=805,4°C, v=0.025mm/min

Hence, the maximum displacement velocity is achieved when the maximum temperature is reached. The curve depicting the height difference between the sensors exhibits a point of inflection at this juncture, which corresponds to the previously analysed velocity variation. This assumption implies that significant sintering takes place at a temperature of 800°C, which is the temperature under experimentation.

Moreover, Fig. 16-B2 reveals that the sintering process does not seem to reach completion at the conclusion of the temperature holding period at 800°C. The disparity in sensor height diminishes smoothly until reaching 1.22 mm, but then it remains constant, creating a region with a height difference of 0.04 mm where no further height reduction, and therefore sintering progression, has taken place.

Due to its extremely high fragility and minimal thickness, the sample undergoes only graphite removal using sandpaper and not polishing. Polishing was avoided to prevent the sample from fracturing. Upon completion, the sample exhibits its appearance as depicted in Fig. 17.

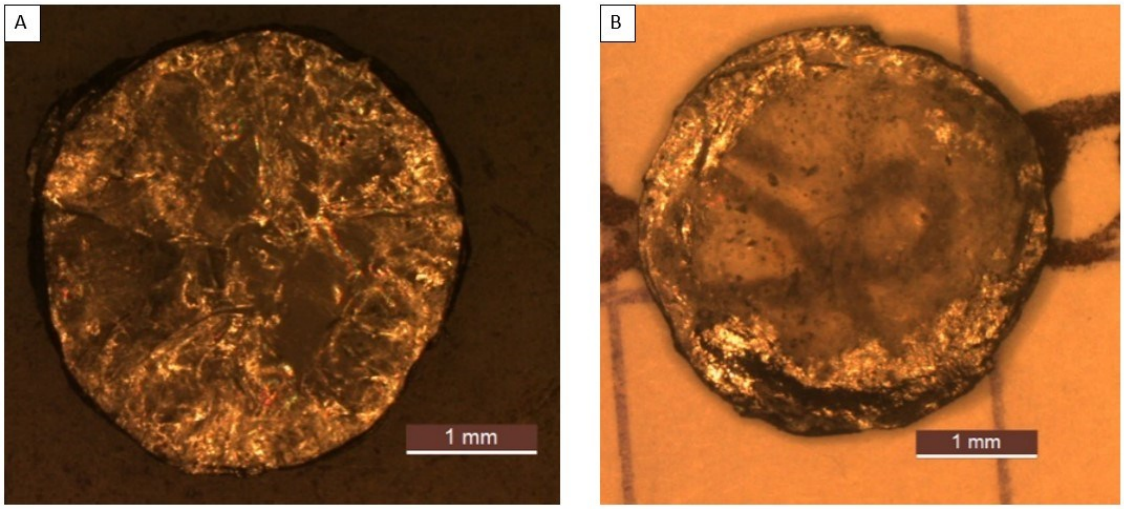

Figure 17 Optical microscope images –(A) entire pellet (B) View of pellet transparency -- SiO2-T800P2

Figure 17-B specifically highlights the presence of transparent regions within the sample, demonstrated by using a piece of paper with writing placed beneath the sample.

Therefore, the sample achieves a partial realization of the intended overall objective, as transparency is an essential requirement. However, it is crucial to consider that transparency is not uniformly achieved in all areas of the sample. Furthermore, the sample exhibits significantly smaller dimensions compared to the theoretically recommended size for the SPS process, as formulated based on established operational procedures.

4.4.2 Characterization of samples

In the following section graphs and a comprehensive analysis of the results obtained from the experimental trials conducted are provided.

4.4.2.1 SEM

SEM analysis is used to characterize sample SiO_2-T1000P2.

The analysis was undertaken with the aim of further investigating the influence of temperature. In the preceding paragraph, it was observed that a temperature of 1000°C led to a phase transformation, resulting in the presence of crystalline quartz. The initial pellet was prepared using powder previously treated at 900°C, ensuring the complete absence of the amorphous phase. However, the sintering process for this sample was conducted at 1000°C, a temperature at which powder crystallization theoretically takes place. The objective, therefore, is to evaluate the impact of temperature on the molecular aggregation of the compacted powders during the sintering process.

Tab. 17 shows the SEM analysis parameters and Fig. 18 (A)-(B) show the images provided by SEM analysis.

Table 17 SEM parameters; SiO2-T1000P2

	A	**B**
FoV [um]	200	20
WD [mm]	4,87	4,87
Speed	1	3
BC [pA]	30	30
Det	E-T	E-T
Scan Mode	UH-RESOLUTION	UH-RESOLUTION
Energy [keV]	1	1
Mag [kx]	1,40	14,0
Pixel size [nm]	195	19,5
Spot size [nm]	4,26	4,26

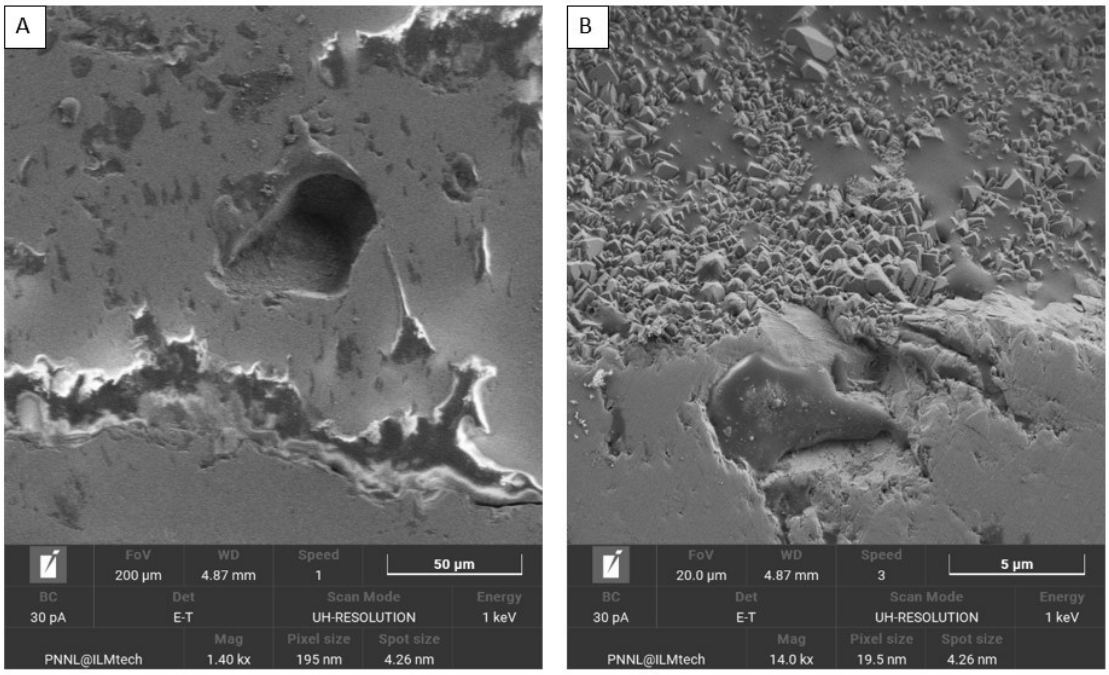

Figure 18 SEM images - SiO2T1000P2: (A) specific area; (B) entire area

The provided images display two notable aspects of the resulting pellet:

- Image (A) exhibits close packed fine grains.
- In contrast, image (B) shows the presence of crystallites: the atomic arrangement seems to create glossy surfaces resembling the facets of a crystalline structure.

As a result, the created pellet possesses a biphasic structure: certain areas exhibit amorphous phases, while others display crystalline regions. The upcoming paragraph will present Raman spectroscopy analysis on this sample, providing a more accurate description and explanation.

4.4.2.2 Raman spectroscopy

Raman spectroscopy analysis is developed to analyse linkage types and the aggregation forms of the particles inside the pellet that may be changed during the sintering process; it is conducted on both sintered silica samples.

- SiO_2-T1000P2

Raman spectroscopy analysis involved directing the laser light onto different regions of the pellet produced during the sintering process. Various measurements were taken, focusing on different areas of the pellet surface, and varying the acquisition parameters of the spectra.

Fig. 19 and Tab. 18 present the areas of interest and the parameters of each measurement that resulted in the acquisition of better spectra, respectively.

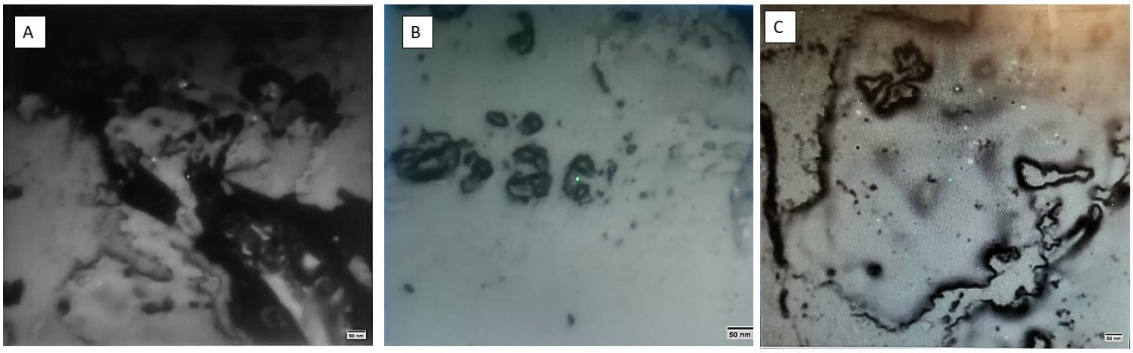

Figure 19 Microscopic images of focalized areas within the pellet: (A) 1st measure, (B) 2nd measure, (C) 3rd measure

Table 18 Raman spectroscopy technical data -- SiO_2-T1000P2

	First measure	Second measure	Third measure
Acquisition time (s)	60	30	20
Accumulations	3	3	1
Instrument	labRAM HR Evol.	labRAM HR Evol.	labRAM HR Evol.
Objective	x50 Lwd	x50 Lwd	x50 Lwd
Laser (nm)	Green 532	Green 532	Green 532
Spectrum (cm^{-1})	907,983	907,983	907,983
Filter (%)	100	100	100

The obtained Raman spectroscopy spectra are shown in Fig. 20 below.

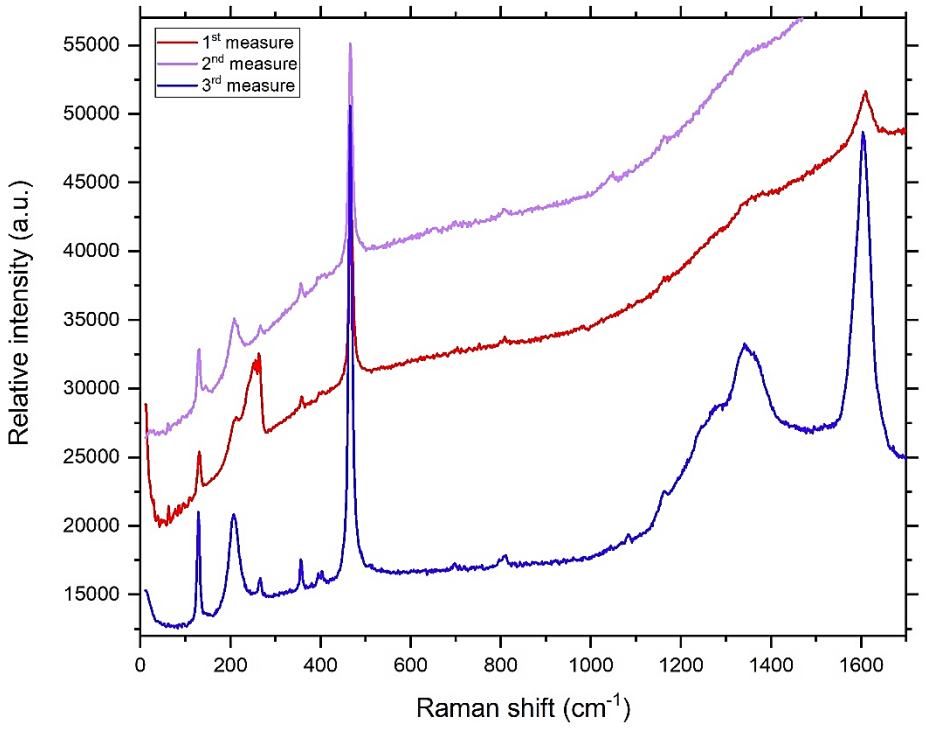

Figure 20 Raman Spectra of SiO_2-1000P2 at different focused areas

The sample exhibits bonding vibrations that align closely with those obtained for SiO_2-T=900°C (*Paragraph 4.2.2.1*). However, a distinctively sharp peak is observed at a Raman shift of 514 cm^{-1}, accompanied by two weaker intensity peaks at 214 cm^{-1} and 325 cm^{-1}.

Through peak analysis, a remarkable similarity was found with the Raman spectrum obtained under atmospheric pressure for alpha-cristobalite, as illustrated in Fig. 21 [*103*].

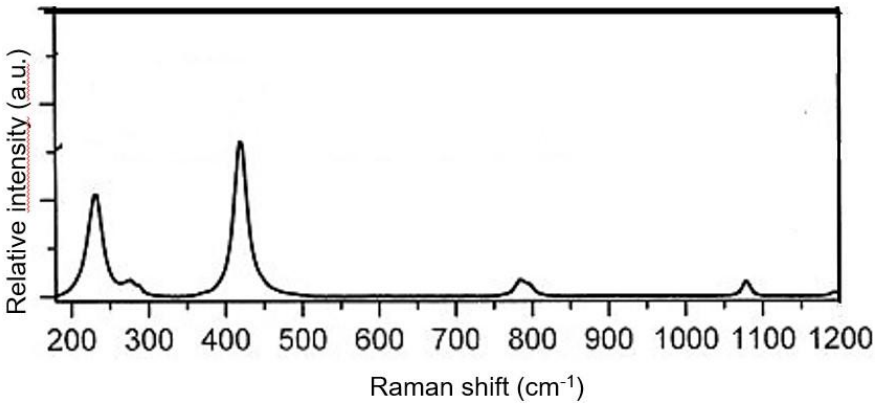

Figure 21 Raman spectroscopy - (alpha) cristobalite

The remarkable correlation observed enables us to draw the conclusion that temperature not only impacts particle aggregation during sintering but also influences the phase they adopt. When the sintering process is carried out at T=1000°C for nanostructured silica, it results, to a certain degree (depending on the duration of the process), in the formation of a crystalline phase known as alpha-cristobalite.

It is crucial to note that the obtained condition differs from what is observed during the powder phase. At T=1000°C in powder form, silica transforms into quartz, while in pellet form, it undergoes transformation into cristobalite.

- SiO_2-T800P2

The development of the Raman spectroscopy analysis for the sample under investigation showed some difficulties, most likely due to the high luminescence and transparency [*104*].

The spectrum acquisition was developed with both instruments (LabRAM and ARAMIS) in order to be able to reduce the effect of diffusion influence; the acquisition parameters are described in Tab. 19 and the best spectrum obtained is shown in Fig. 22

Table 19 Raman spectroscopy technical data -- SiO2-T800P2

	First measure	Second measure
Acquisition time (s)	10	1
Accumulations	3	3
Instrument	ARAMIS	ARAMIS
Objective	x100	x101
Laser (nm)	HeNe-633	HeNe-634
Spectrum (cm^{-1})	905,075	905,075
Filter (%)	100	100

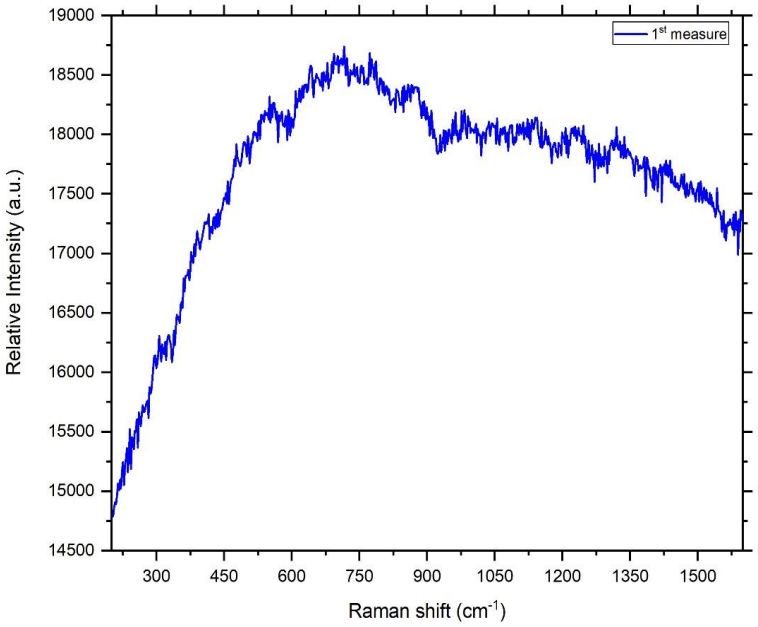

Figure 22 Raman spectrum --SiO2-T800P2

It is possible to notice the absence of a glass pattern; in a general point of view, it is a spectrum where there is not the possibility to link Raman shift values to the bond vibrations. Although this impossibility does not allow the validation of the analysis performed, it can nevertheless be noted that no vibration peaks are present either; this therefore indicates that sintering at a temperature T=800°C does not produce crystal formation, unlike the sample previously analysed (T=1000°C).

4.4.2.3 Density measurements

Density measurement is regarded as a valid test for qualitative evaluation of the sintering process. It enables the identification of whether the sintering process is complete or incomplete, thus indicating whether the achieved outcome represents the true result.

Density measurements were performed using the Archimedes' principle test. By evaluating the variation in mass of the pellet when measured in two different fluids (air and water) and possessing knowledge of the glass's theoretical density, it becomes feasible to assess the relative density and provide a semi-quantitative indication of the accomplished sintering.

Density measurements results are presented below:

- SiO_2-T1000P2: 98,51%
- SiO_2-T800P2: 99,39%

The lack of attainment of the unit value indicates that the process, conducted as described above, did not lead to complete sintering. This observation reaffirms the previously stated information in *Paragraph 4.4.1*

However, it is crucial to note that the density measurement was carried out on the pellet that still contained an unremovable graphite region, as explained in *Chapter 3-Paragraph 3.1.2*. The obtained value is, therefore, influenced by the presence of graphite, thereby causing a lower absolute relative density value when referring to silica glass alone.

4.5 Conclusions

In the examined chapter, the experimentation conducted at the French laboratories focused on pure silica was described. Silica particles, with a diameter of 7 nm at room temperature (25°C), underwent a heat treatment at 900°C, resulting in a weight loss of 23.05%. This weight loss is attributed to the removal of adsorbed water and carbon dioxide from the particle surfaces, along with an increase in their size. The particles selected for subsequent processes had a diameter approximately twice that of the initial size.

Subsequently, the characterization analysis immediately after the calcination process revealed that heat treatment at 1000°C would lead to a phase change, with the formation of quartz, losing the characteristic amorphous structure of glassy materials.

To study the behaviour of the particles under pressure, a Diamond Anvil Cell in situ with Raman spectroscopy was used, reaching a maximum pressure of 4.53 GPa. A slight shift to the right of the peaks associated with the vibrational bands of silica bonds was observed. Although the shift is minimal with increasing pressure, a significant overall difference was noted between atmospheric pressure and the maximum pressure reached. Furthermore, the relative intensity of each curve increased with increasing pressure.

Silica particles pre-treated at 900°C were subsequently subjected to Spark Plasma Sintering (SPS) with constant pressure and a dwell time of 2 GPa and 3 minutes, respectively. By varying the process temperature from 1000°C to 800°C, transparent zones were observed. In situ measurements during the process indicated an incomplete process for both samples. The Archimedes test, conducted on both samples, yielded a relative density of 99.39% for the sample processed at 800°C. However, it is important to note that the accuracy of this data might be compromised due to the difficulties in completely eliminating graphite from the cylindrical walls of the pellet, given its extreme fragility.

Another noteworthy observation is that increasing the temperature to 1000°C not only failed to achieve transparent zones but also led to the formation of surface crystallites, identified as alpha-cristobalite through spectroscopic analysis.

The discussion highlights two key points: crystallization occurs at lower temperatures due to the combined effect of pressure and smaller particle sizes, and the possibility of achieving transparency at temperatures approximately 300°C lower than traditional silica glass production temperatures represents a significant discovery. This result confirms the potential for the development of unconventional sintering processes for glass production, contributing to more efficient use of energy and resources.

CHAPTER 5

Production of a borosilicate glass starting by sub-micrometrical particles

In this chapter, the production of borosilicate glass from sub-micrometric particles of commercial glass powder will be examined. Initially, the chemical and physical characteristics of these particles are introduced, with a primary focus on their glass transition temperature and their significantly larger diameter compared to the silica particles discussed in the preceding chapter.

The main objective of this experimentation is to quantitatively assess the influence of particle size on sintering processes. Borosilicate particles will undergo two distinct treatments: the Spark Plasma process, analogous to the one applied to silica particles, and the cold sintering process. A comprehensive description of the latter process will be provided to present the outcomes obtained concerning sub-micrometric particles. Furthermore, a thorough examination of the multitude of parameters governing the sintering process will be conducted to fully comprehend their impact on the process itself.

With this approach, the aim is the contribution of the understanding of borosilicate glass production by providing a comprehensive overview of particle characteristics and the effect of particle size on sintering processes.

5.1 "Duran" glass: chemical and physical specifications

The particles under study are obtained through the milling of glass powders of type of the "Duran" type, a borosilicate glass manufactured by DURAN Group GmbH, which conforms to borosilicate glass 3.3 standards (DIN ISO 3585). This material is renowned for its robustness and is typically produced by substituting alkali oxides with boric anhydride within the silica glass lattice. The introduction of boric anhydride into the silica lattice weakens the structure due to the presence of planar three-coordinate boron atoms, thus lowering the glass's softening point.

In its bulk glass form, this material exhibits excellent chemical resistance to aqueous solutions, salts, acids, and bases. It complies with Class 1 of DIN 12 116 standards for acid resistance and Class 2 of DIN ISO 695 standards for base resistance. However, it's worth noting that the material's behaviour can vary based on the size of its constituent elements. The aforementioned characteristics pertain to bulk borosilicate glass analysis. Given the uncertainty regarding the precise composition of the oxides comprising the glass in particle form, this thesis work will refer to the composition typical of borosilicate glass recorded in Equation (1):

$$80{,}5\%\ SiO_2,\ 12{,}5\% B_2O_3\ ,\ 4{,}5\% Na_2O|K_2O,\ 2\%\ Al_2O_3,\ 0{,}5\% CaO|MgO \quad (1)$$

These glass particles are selected to conduct sintering experiments due to the specifications provided to the University:

- Average diameter = d = 810 nm
- Glass transition temperature = Tg = 450°C

According to the information provided, these particles exhibit a sub-micron size, significantly larger than that of the silica used in the processes described in Chapter 4 of this thesis. However, the glass transition temperature is much lower compared to that of standard borosilicate glass [*105*]. This unique characteristic, which was a driving factor in choosing to conduct part of the experimentation with these particles, could be a significant advantage. It might lead to the development of sintering processes that require much lower temperatures than conventional sintering methods.

5.2 Characterization of particles

Characterization analyses will be performed to confirm values regarding size and glass transition temperature; it will be done by SEM and DSC/TGA analysis. These will provide greater certainty about material's properties, ensuring increased precision in interpreting the results of experiments related to sintering process development.

5.2.1 DSC/TGA

The DSC/TGA characterization analyses were extended up to a temperature of 1300°C to precisely determine the temperature at which weight loss occurs and any temperature variations indicative of heat absorption or release due to phase changes or specific chemical reactions. Fig. 1 displays the results of the analysis conducted on the "Duran" glass particles.

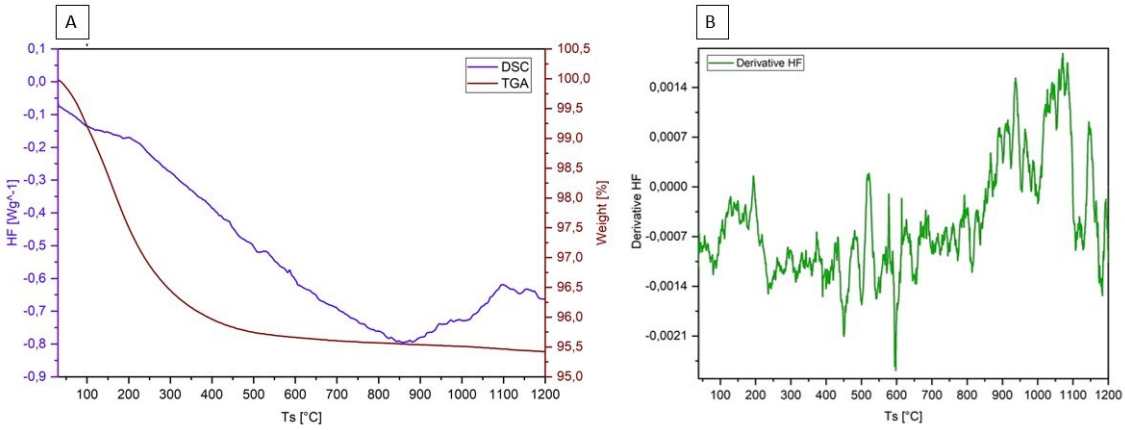

Figure 8 (A) DSC/TGA curve; (B) Derivative HF curve

In the DSC curve, a distinct change in slope is observed at around 300°C, likely corresponding to the elimination of water or volatile compounds. Conversely, the TGA curve exhibits a pronounced minimum at approximately 600°C, though its interpretation remains somewhat ambiguous.

The analysis of the derivative of the DSC curve yielded limited additional insights. The analysis resulted in a curve with significant noise, necessitating data smoothing. Curve (B) represents the best approximation obtained through data processing. However, the complex pattern makes it challenging to identify specific heat absorption or release peaks. A potential peak around 480°C has been tentatively identified as a glass transition temperature. Nevertheless, it's crucial to regard this temperature as a reference with a degree of uncertainty rather than an absolute certainty.

5.2.2. SEM

In Fig. 2, the images obtained through Scanning Electron Microscopy (SEM) of commercial borosilicate glass powder are presented.

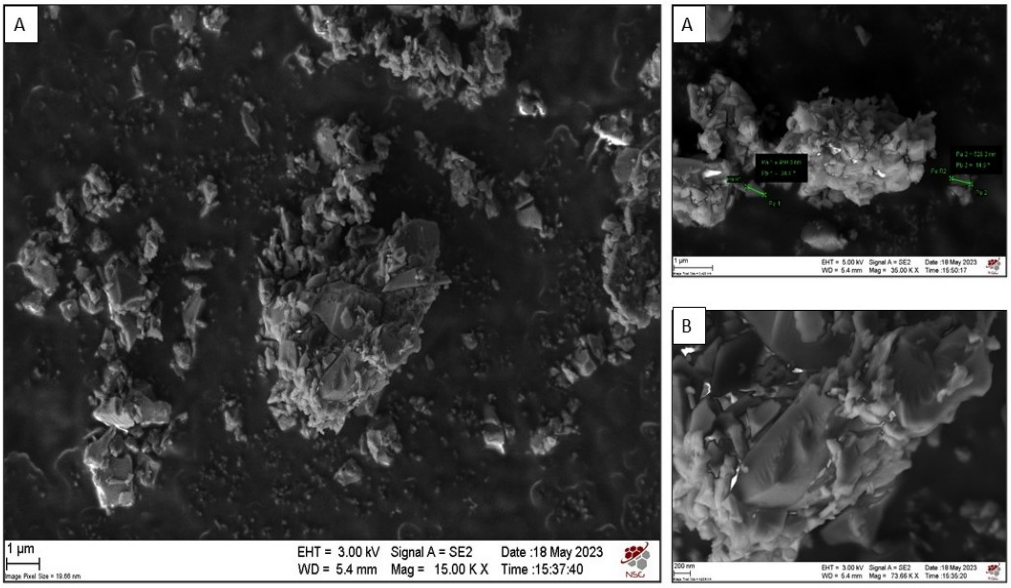

Figure 9 SEM images: commercial borosilicate glass powder: (A) general particle view, (B) zoom on specific area.

The powder is in the form of flaxes rather than discrete particles, resulting from the grinding process. The SEM images clearly show strong agglomeration of the flaxes. Approximate dimensions of the powder constituents have been determined from the SEM images: powders consist of agglomerates with an average size of 1260 nm; flakes have a size of 530 nm, that is slightly smaller than the initially provided value of 810 nm, suggesting a variation in production, or in grinding process.

In conclusion, the use of scanning electron microscopy has allowed for a detailed evaluation of the morphological characteristics of borosilicate glass powder and has provided valuable information about its structure and constituent sizes.

5.3 DAC- influence of pressure on particle properties

The evaluation of changes in the powder as the pressure varied, based on the assessment of its reflective behaviour through optical microscopy, is given by the powder analysis in DAC.

5.3.1 Process parameters

The experiment was conducted as follows on the base of what explained in *Chapter 3-Paragraph 3.2.3.1*.

The powder was placed in the cavity of the metallic gasket that forms the entire diamond anvil cell. The powder was used in a completely dry state, without any liquids, and without undergoing previous thermal treatment, so exactly as it is commercially available as “Duran” borosilicate glass powder, to assess its real behaviour under pressure. The ruby was not inserted.

Subsequently, the upper membrane of the cell was placed, and the whole setup was connected to the pressure generator. During the experimental phase, the gas pressure was increased from 0 bar to a maximum of 50 bars, corresponding approximately an internal pressure of 18-20 GPa within the cell. As explained in *Chapter 3-Paragraph 3.2.3.2*, since the ruby was not used, it was not possible to determine the exact value of the internal pressure achieved.

5.3.2 Evaluation of results

Fig. 3 illustrates the evolution of the powder as the pressure increases. Optical microscopy acquisitions were taken at regular pressure intervals to provide a comprehensive depiction of the pressure-induced changes. Each gas pressure condition was captured under the following acquisition conditions:

- A: Absence of upper light, with constant intensity of light from below.
- B: Presence of upper light, with constant intensity of light from below.
- C: Presence/absence of upper light, with reduced intensity of light from below.

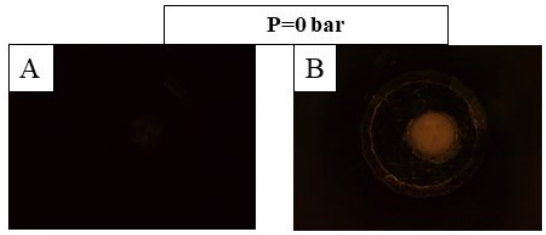
P=0 bar
A
B

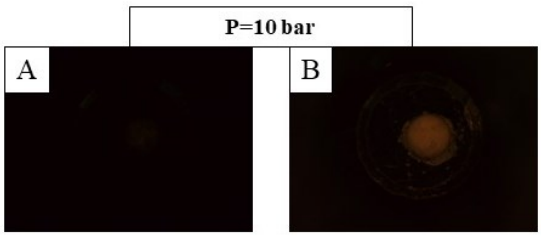
P=10 bar
A
B

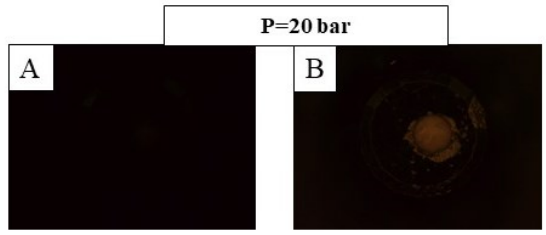
P=20 bar
A
B

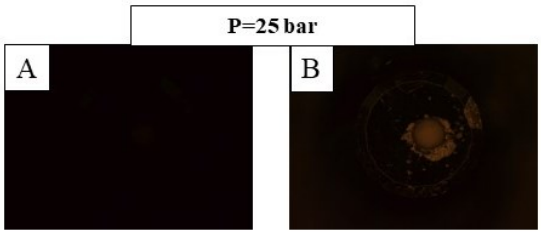
P=25 bar
A
B

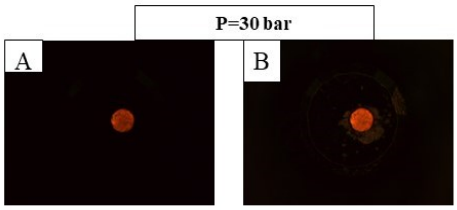
P=30 bar
A
B

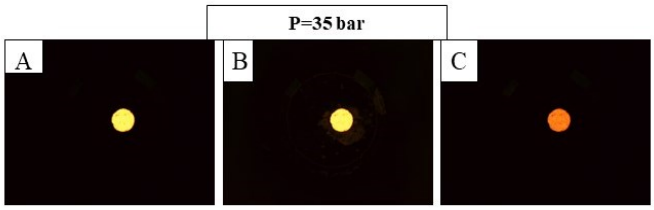
P=35 bar
A
B
C

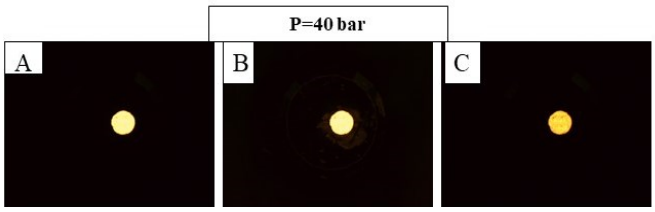
P=40 bar
A
B
C

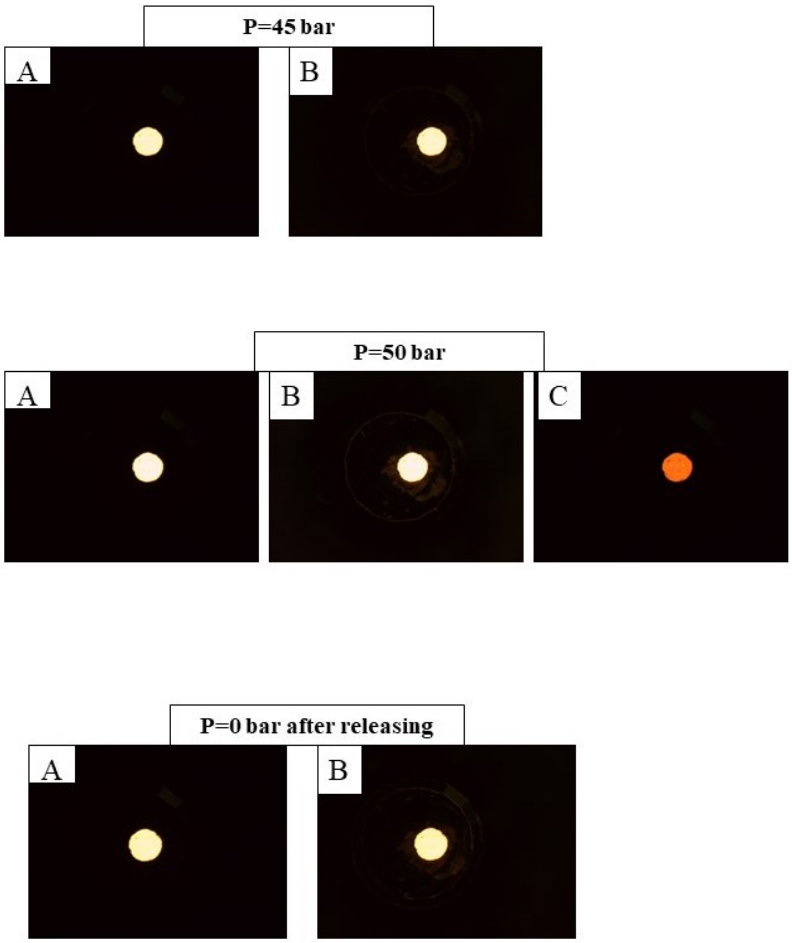

Figure 10 Effect of pressure on borosilicate powder glass – (A) absence of upper light, constant intensity down; (B) existence of upper light, constant intensity down; (C) with or without upper light, less intensity down

It can be observed that increasing the pressure from zero bar to fifty bar causes the powder to transition from a white colour to a pale yellow, passing through red (30 bar), orange (35 bar), and bright yellow (40 bar). The colour variation becomes noticeable starting from a pressure of 25 bars.

Under a pressure of P=45 bar, equivalent to approximately 15 GPa within the powder, it appears that translucent regions have been achieved. After releasing the pressure, the powder exhibits the same colour as it reached after being subjected to approximately 18-20 GPa.

5.3.3 Raman spectroscopy

The following Fig. 4 illustrates the resulting Raman spectrum of the analysed commercial borosilicate glass powder after undergoing cold compression in a diamond anvil cell. To provide an accurate analysis, the spectrum is directly compared with that of a Pyrex glass, which has been previously studied and referenced [*106*].

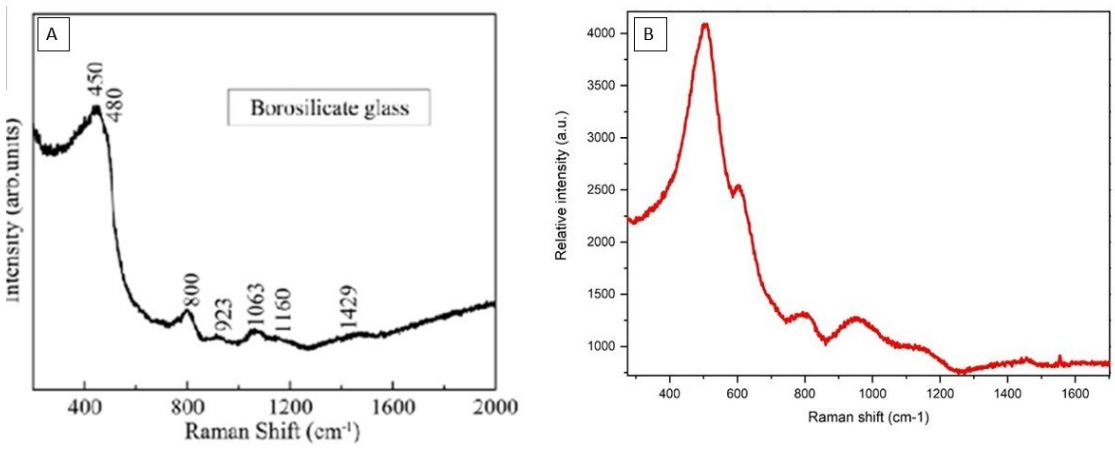

Figure 11 Raman spectrum: borosilicate glass powder after DAC pressure released - (A) reference borosilicate glass, (B) analysed glass.

From the comparison, it is evident that the analysed commercial glass (red curve) exhibits a Raman spectrum that closely resembles, and at times overlaps with, that of a fully densified borosilicate glass (specifically, the characteristics of Pyrex glass in the comparison). Significant shifts towards higher frequencies in the main band and an increased D2 band with a Raman shift of 600 cm^{-1} can be observed.

Thus, it is apparent that the cold compression process in the diamond anvil cell has resulted in a substantial densification of the sample.

5.4 Glass production by cold sintering process

Following the assessment of the behaviour exhibited by powders under high-pressure conditions, this paragraph aims to examine their response when subjected simultaneously to variations in both pressure and temperature. Specifically, the behaviour during the cold sintering process will be evaluated; fundamental characteristics of this process will be

presented, with a focus on the significance of the involved parameters and the optimization strategies employed.

In the latter part of the paragraph, the outcomes of the characterization analyses conducted on the samples will be presented. Special emphasis will be placed on accurate density measurements, as well as on the visual interpretation of results and micrographic analysis.

5.4.1 Optimization of process parameters

The development of the cold sintering process has been detailed in Chapter 3, Section 3.1, where technical specifications of the mould and the constituent phases of the process are provided. Numerous parameters were meticulously considered, including pressure, temperature, molarity of the sodium hydroxide solution, quantity of liquid phase over the powder, and the duration for which the powder-liquid mixture remained within the mould.

The initial sample was produced under dry conditions, with no retention time: the solution's molarity was 2M, temperature was 200°C, and the absence of any liquid phase was ensured (powder was completely dry). Commencing from this pilot sample (denoted as *2M, 2T*), alterations were introduced. Initially, the amount of liquid phase was augmented in relation to the total, followed by an increase in both temperature and liquid phase concentration. The chosen pressure value consistently remained at the maximum allowed by the mould; it is 250MPa.

Consequently, experiments were conducted as follows: at a fixed concentration of solution molarity (15M), tests were performed at 200°C (referred to as "2T" in the sample nomenclature), at 250°C ("5T") and for a dwell time equal to 15, 30, 60 and 120 minutes. Furthermore, the powder development process incorporated pre-heating of the mould. As previously discussed in Chapter 3, once pressure was applied, the heating of the mould initiated, and the retention time was determined based on reaching the desired temperature. Pre-heating the mould entailed introducing the powder into the mould after it had already reached the intended temperature. It's worth noting that the temperature attainment time was calculated precisely, considering the time it took for the mould to reach specific temperature

values. Tab. 1 presents the temperature-time correlation of the instrument, while Fig. 5 illustrates the logarithmic scale governing the temperature attainment over time.

Table 8 Temperature-time correlation for CSP mould

T [°C]	ΔT	Δt	t [min]	t [s]
20			0	0
30	10	00:01:19	00:01:19	79
50	20	00:01:22	00:02:42	164
70	20	00:01:22	00:04:04	244
90	20	00:01:35	00:05:38	338
110	20	00:01:43	00:07:21	441
130	20	02:01,1	00:09:23	563
150	20	02:22,8	00:11:45	705
170	20	03:09,1	00:14:54	894
190	20	05:32,8	00:20:27	1227
200	10	04:24,0	00:24:51	1491

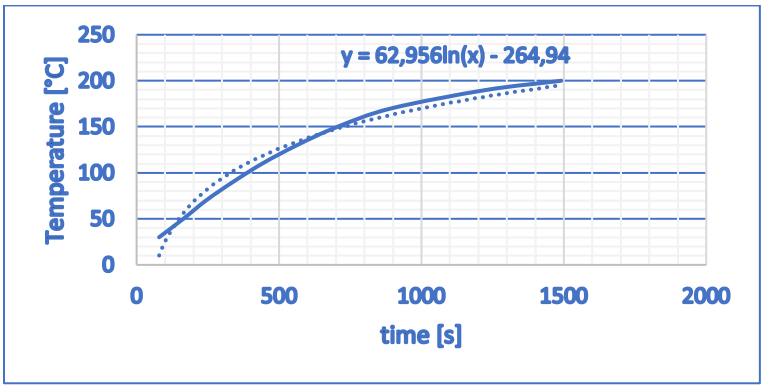

Figure 12 Temperature trend as a function of time in the CSP mould

Consequently, the powder underwent pressure and temperature for the same duration without a preceding pressure phase.

During the advancement of the cold sintering process on these examined particles, optimization was pursued by evaluating the entire spectrum of parameters. Subsequently, a summary table (Tab. 2) is presented below, detailing all the produced samples, and specifying the parameter values used in the production of each sample. In the naming of the samples, please take into account a specific detail: the amount of liquid phase relative to the solid

powder mass used for pellet production is indicated. Two relative quantities have been evaluated with respect to the powder mass itself: 14% and 28%.

Table 9CSP sample overview

Sample	***Powder mass [g]***	***Liquid to solid phase [%]***	***Amount of basic solution [ml]***	***Solution molarity [M]***	***Pressure [MPa]***	***Temperature [°C]***	***Dwell Time [min]***	***Drying Temperature [°C]***	***Drying Time [min]***
2M, 14T	1	14	0,2	2	250	25	15	60	48
2M, 170T, 14P	1	14	0,2	2	250	170	15	60	48
2M,2T, 14P-15	1	14	0,2	2	250	200	15	60	24
2M,2T,28P-15	1	28	0,4	2	250	200	15	80	24
10M,2T, 28P- 15	1	28	0,4	10	250	200	15	80	24
15M, 2T, 28P-15	1	28	0,4	15	250	200	15	80	24
15M,2T,28P-30	1	28	0,4	15	250	200	30	80	24
15M,2T,28P-60	1	28	0,4	15	250	200	60	80	24
15M,5T,28P-15	1	28	0,4	15	250	250	15	80	24
15M,5T,28P-30	1	28	0,4	15	250	250	60	80	24
15M,5T,28P-60	1	28	0,4	15	250	250	30	80	24
15M,2T,14S-15	1	14	0,33	15	150	128	15	80	24
15M,5T,14P-30	1	14	0,33	15	250	128	60	80	24
15M,2T,14S-60	1	14	0,33	15	250	250	30	80	24
15M,2T,14P-120	1	14	0,33	15	250	250	120	80	24
15M,2T,14P-60 (1/2)	0,5	14	0,33	15	250	250	60	80	24
15M,2T,14P-30 Preh.	1	14	0,33	15	250	250	30	80	24
15M,2T,14P-60 Preh.	1	14	0,33	15	250	250	60	80	24
15M,2T,14P-120 Preh.	1	14	0,33	15	250	250	120	80	24

This table provides a concise overview of all the samples produced, along with the specific parameter values used to produce each sample.

5.4.2 Characterization of samples

The samples fabricated using the methodologies are depicted in Fig. 6. The image is composed of several clusters of pictures, thus showcasing the produced samples according to the sequences of conducted tests. This presentation approach is favoured over the chronological development sequence of images, as it allows for a more intuitive grasp of the obtained results.

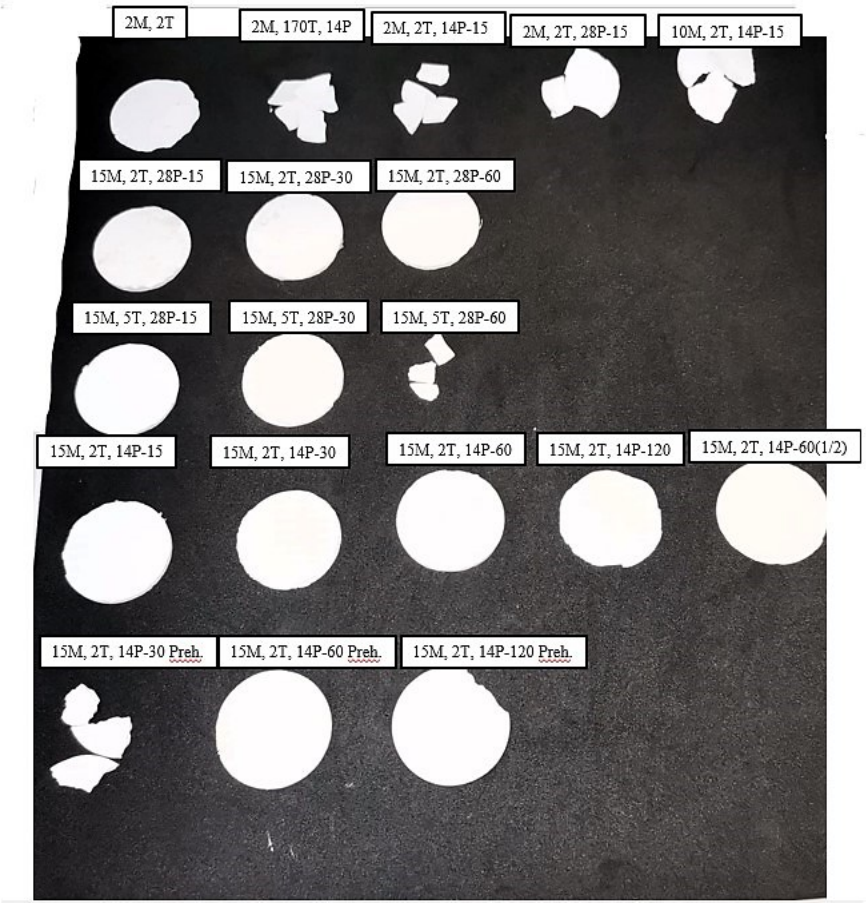

Figure 13 Pellets obtained by CSP process.

Through a meticulous visual examination of the captured images, it becomes apparent that none of the produced samples exhibit zones of transparency or even faint translucency phenomena. While this observation is purely qualitative and lacks scientific analysis, it suggests that none of the samples have undergone complete sintering [*107*]; Archimedes'

density tests and scanning electron microscopy, elucidated in the subsequent section, will be instrumental in assessing this observation.

5.4.2.1 Density measurements

The primary parameter under scrutiny was the relative density of the samples, gauged against the theoretical density of a borosilicate glass, as expounded in Chapter 5, Paragraph 5.1.

The density measurement was executed through the implementation of the Archimedes' principle test. The tables comprising the collective Table 3 present, categorized by sequences of samples, grouped into sequences characterized by fixed parameters written in each table, the density values associated with each produced sample. Figure 7 illustrates the trend of the relative density values for the obtained samples. The samples have been grouped into sequences, characterized by fixed parameters listed in each table.

Table 10 Density values of samples_borosilicate glass pellets

Sequence 1: [NaOH]=2M T=200°C t=15min			**Sequence 2: [NaOH]=2M L/S=14% t=15min**		
L/S [%]	*Relative ρ [%]*	*Theoretical ρ [%]*	*T [°C]*	*Relative ρ [%]*	*Theoretical ρ [%]*
14	89,04	100	20	78,06	100
28	91,15	100	170	80,88	100
			200	89,04	100

Sequence 3: [NaOH]=15M T=200°C L/S=28%			**Sequence 4: [NaOH]=15M T=250°C L/S=28%**		
t [min]	*Relative ρ [%]*	*Theoretical ρ [%]*	*t [min]*	*Relative ρ [%]*	*Theoretical ρ [%]*
15	82,65	100	15	81	100
30	82,08	100	30	94	100
60	82,03	100	60	81	100

Sequence 5: [NaOH]=15M T=200°C L/S=14% Sequence 6:			[NaOH]=15M T=200°C L/S=14% Pre-heated die		
t [min]	*Relative ρ [%]*	*Theoretical ρ [%]*	*t [min]*	*Relative ρ [%]*	*Theoretical ρ [%]*
15	81,17	100	30	84,89	100
30	91,12	100	60	90,26	100
60	86,83	100	120	86,21	100
120	84,89	100			

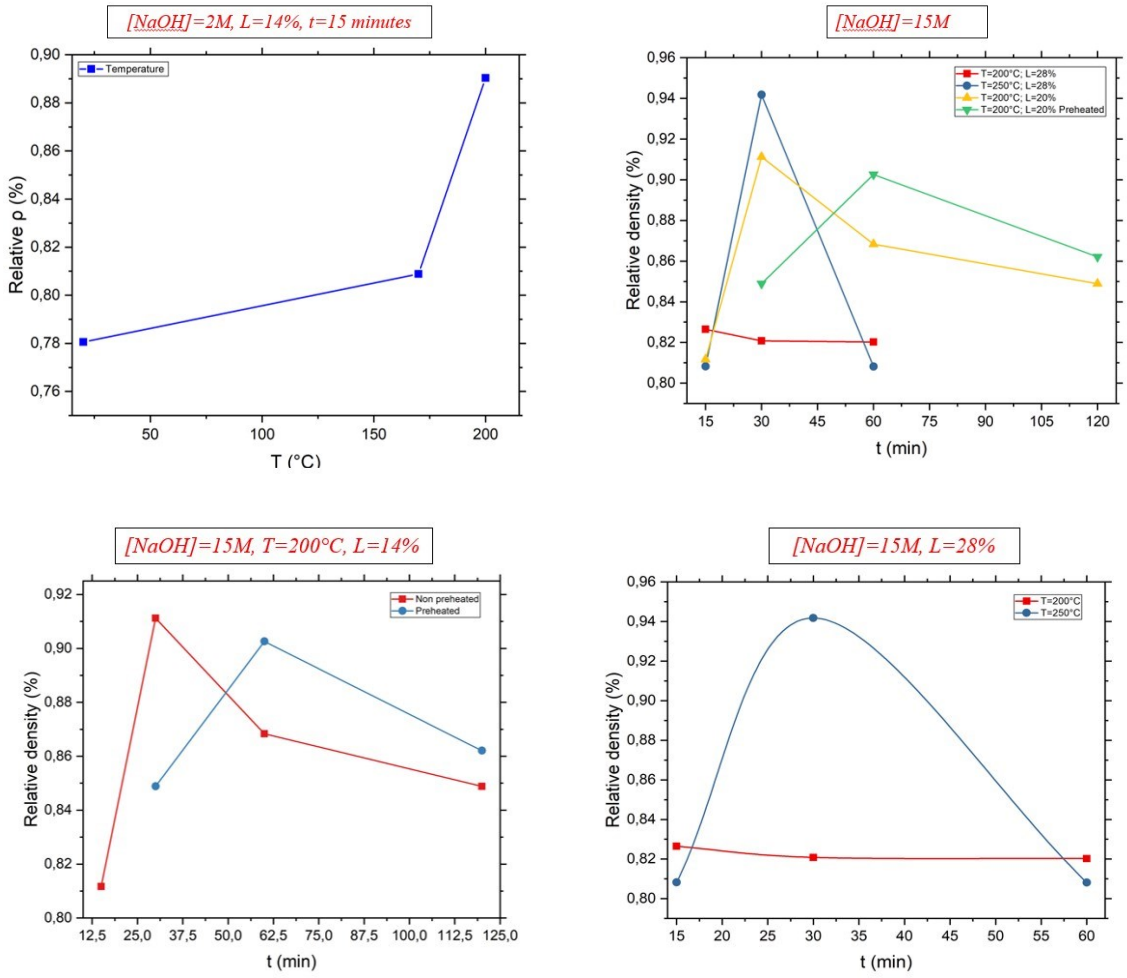

Figure 14 Relative density trend on the base of significant parameters

The following observations can be deduced from the above illustration:

- While keeping the solution molarities constant (2M), the quantity of liquid phase, and the residence time, there is an increase in relative density as the temperature rises, reaching a peak value (0.89) at T=200°C.
- In the case of a constant solution molarity (15M), the residence time does not influence the process at T=200°C and L=28%, but it affects the evolving processes at different temperatures and quantities of liquid phase. In general, a peak in relative density is observed during intermediate development times.
- Mould preheating affects the sintering kinetics: albeit to a minimal extent, an increase in relative density is observed when a preheated mould is used.
- A higher process temperature (T=250°C) leads to an increased relative density compared to the process conditions at T=200°C. However, it is noteworthy that, for the second of the mentioned conditions, no significant differences arise in the powder residence times within the mould. As the process evolves at T=250°C, the relative density seems to increase until a residence time of 30 minutes in the mould, and then gradually decreases if the process is extended for an additional 30 minutes.

It is conspicuously evident that none of the manufactured samples reached 100% relative density; in fact, the values are significantly disparate. The highest peak values are as follows:

- 15M, 5T, 28P– 30 = 94,18%
- 15M, 2T, 14P – 120 = 91,12%

It is noteworthy that the samples under consideration vary across multiple aspects: the testing temperature, the phase under scrutiny (liquid compared to the overall mass), and the exposure duration. Specifically, the first sample is a product of the cold sintering process carried out at a temperature of 250°C for a duration of 30 minutes, constituting 40% of the total mass (equivalent to 28% liquid relative to the powder quantity). On the other hand, the second sample stems from a procedure employing an extended period (120 minutes) and a lower temperature (200°C), presenting a lower percentage of liquid phase in contrast to the solid phase (20%).

Those samples exhibiting the highest density values, as per the Archimedes' principle test, were subsequently subjected to pycnometer analysis—a method affording a more precise assessment of density, developed using a “Ultrapyc 3000” type. The ensuing values are presented as follows:

- 15M, 5T, 28P – 30 = 84,43%
- 15M, 2T, 14P – 120 = 89,07%

As evidenced by the results obtained from the picnometric test, the obtained values significantly deviate from those acquired through the Archimedes' principle test, displaying a disparity of approximately 15% for the former and 4% for the latter. The presence of lower density, as observed in the Archimedes test, is correlated with the white pellets’ colour. This suggests the hypothesis that these values may indicate the presence of closed porosity within the pellets themselves. The confirmation or dismissal of this hypothesis will be assessed later through SEM analysis, which will enable a detailed visualization and evaluation of the internal characteristics of the pellets.

Based on the conducted density measurements, definitively ascertaining which of the two samples exerts a superior influence on the powder densification process proves to be challenging. Nevertheless, it can be asserted with absolute confidence that these represent the highest quality samples generated. It is important to underscore, however, that the sintering process has not reached its completion phase.

5.4.2.2 SEM

Based on the density values obtained from the borosilicate glass pellets produced, SEM analysis was conducted on some of these pellets to provide more detailed information.

The SEM analysis was performed using the "E-SEM FEI Quanta 200" instrument and was carried out in both "secondary electron" and "backscattered" modes. Images of the pellet surfaces were captured, as well as cross-sectional images. However, in this report, surface images of the pellets will not be included as they are considered less significant due to surface contamination and lack of polishing. The absence of pores or bubbles on the surface, which

are present in the cross-sectional view, suggests the presence of closed porosity, which will be confirmed in the subsequent analysis of the corresponding samples. Only SEM images showing the cross-sections, i.e., the internal fracture surfaces, will be presented. These images allow for interesting observations regarding porosity and the degree of powder compaction.

The samples selected for SEM analysis were chosen based on the density measurements' best results, as reported in Table 3. In addition to the pellets for which density was also measured using a pycnometer, SEM analysis was conducted on representative samples from each sequence.

The sample "2M, 2T, 28P-15," with a relative density of 91.15%, exhibits a cross-section as shown in Fig. 8. Two images of the cross-section were captured: (A) was obtained in "secondary electron" mode, while (B) was obtained in "backscattered" mode.

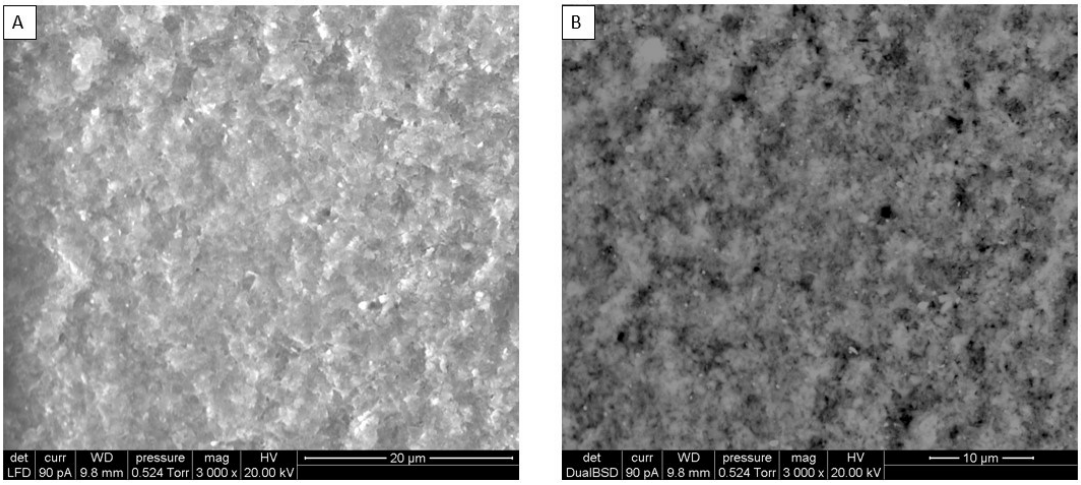

Figure 15 SEM cross-sectional images for "2M, 2T, 40P-15" sample: (A)secondary electron mode, (B) backscattered mode.

The first important observation to make is that no fracture surfaces can be detected from the images. Image (A) displays a highly compact system, suggesting significant densification achieved in the sample. Through a rough estimate based on image (B), the porosity was assessed to be around 10%, and the pore sizes do not exceed 13 nm.

Sample "15M, 2T, 28P-30", with a relative density of 82,08%, belongs to a sequence in which the maximum possible concentration of sodium hydroxide, a component of the liquid phase,

was used, but the treatment temperature was limited to 200°C. Fig. 9 shows significantly different results compared to the previous sample.

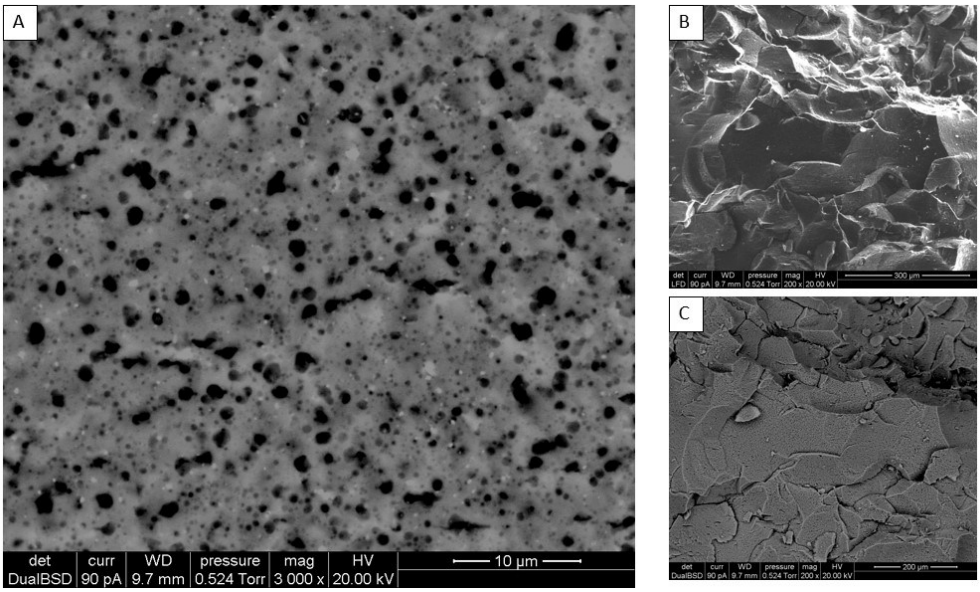

Figure 16 SEM cross-sectional images for "15M, 2T, 40P-30" sample: (A) and (C) backscattered mode, (B) secondary electron mode

Image (A) obtained through backscattered mode clearly shows porosity within the pellet; the pores have an average size of about 480 nm and constitute approximately 14,76% of the area of interest. Images (B) and (C) depict the fracture surfaces. (C), captured at higher magnification, reveals intricate details on the surface. The presence of significant porosity indicates that powder compaction was not fully achieved, confirming the density measurements. Furthermore, the presence of fracture surfaces suggests that strong bonds and a compact three-dimensional lattice were not developed in the material.

The density measurements on the sample "15M, 5T, 40P-30" have raised doubts due to a significant 10% difference in relative density compared to the expected results ($\rho_{\text{Archimede's test}} = 94{,}18\%;\ \rho_{\text{picnometer}} = 84{,}43\%$). Images (A) and (B) in Fig. 10 show a non-compact structure, highlighting the presence of internal porosity and bubbles.

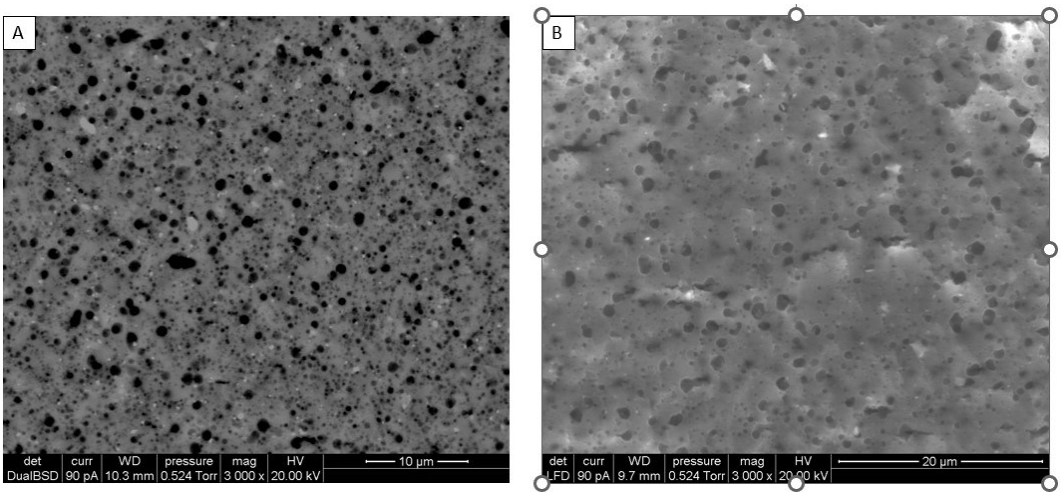

Figure 17 SEM cross-sectional images for "15M, 5T, 40P-30" sample: (A) backscattered mode, (B) secondary electrons mode

The main difference from the previous sample is the higher treatment temperature. This may have caused faster evaporation of the water present in the highly concentrated sodium hydroxide aqueous solution, increasing the likelihood of bubble formation: from image A, it can be inferred that the average pore size is around 1200 nm, and the pores cover 25% of the area of interest. Furthermore, higher temperatures can trigger exothermic chemical reactions between the materials, releasing heat and generating trapped vapor bubbles within borosilicate compounds and sodium hydroxide. It should be noted that this analysis is based on a single sample and is speculative, requiring further investigation for confirmation.

Sample "15M, 2T, 14P-60 (preh.)" differs from the previous sample not only because the powder was not placed in a mould already heated to the operating temperature but also due to a longer dwell time of the powder inside the mould. Fig. 11 shows good compaction of the sample, as highlighted in both (A) and (B).

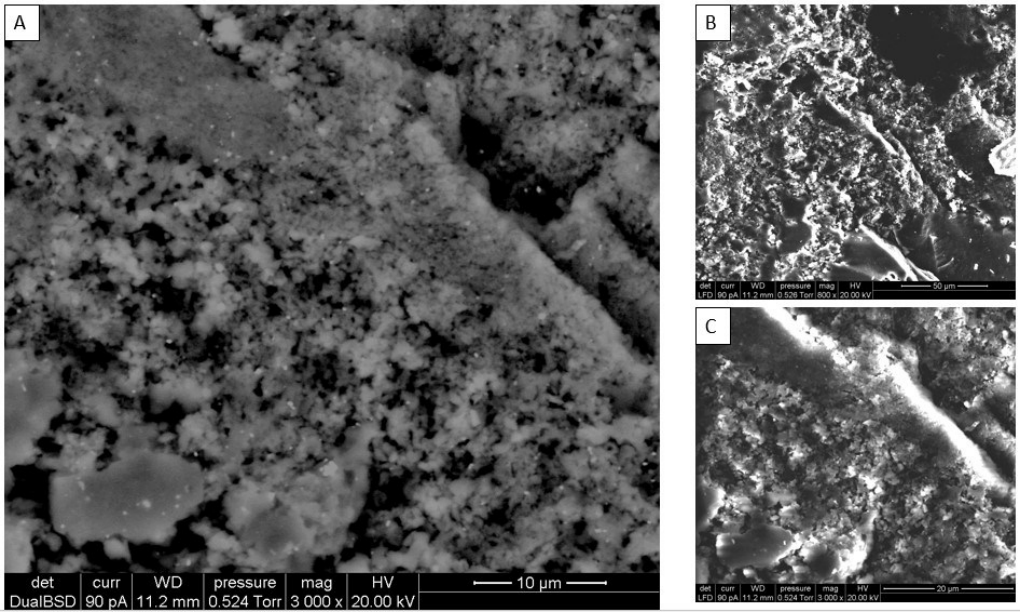

Figure 18 SEM cross-sectional images for "15M, 2T, 20S-60 (prer.)" sample: (A) backscattered mode, (B) and (C) secondary electrons mode

These images, obtained in secondary electron and backscattered electron modes, highlight a significant characteristic of the sample: it exhibits a rugged internal structure. The structure appears to be composed of two distinct phases: there are groups of particles that have not completely compacted together, and areas where there seem to be flakes of compacted dust that, however, are not associated with the same groups of particles. Furthermore, image (C) confirms the hypothesis of incomplete compaction, showing the presence of porosity with pores of average diameter 700 nm. The pores constitute about 15% of the structure, measurements taken on the magnification represented in image (C).

Sample "15M, 2T, 14P-120" underwent density measurements through both tests; the results obtained from the Archimedes (91,12%) test and the pycnometer test (89,07%) show a difference of approximately 2%, confirming the consistency of results between the two methodologies. Fig. 12 shows a significantly more compact structure: the particles have fused to form layers of compact material. Although there are gaps between the various layers that constitute actual separations, each layer is well compacted.

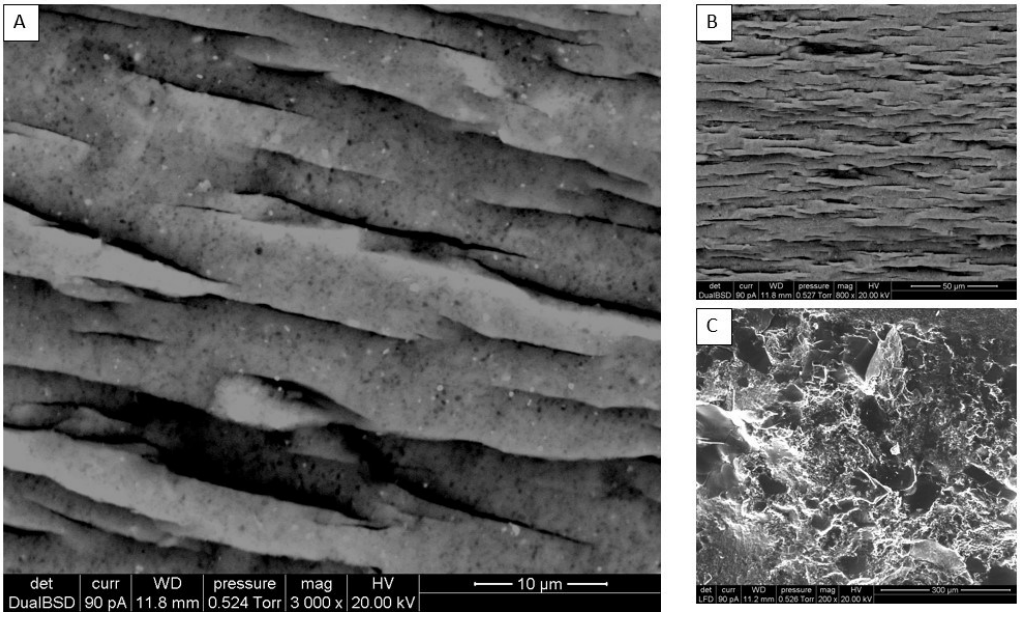

Figure 19 SEM cross-sectional images for "15M, 2T, 20S-120" sample: (A) and (B) backscattered mode, (C) secondary electrons mode

Accurately measuring porosity in this situation is complex. Image (A) highlights areas where closed pores are present on the cross-sectional inner fracture surface, with an average diameter of 300 nm. Image B highlights the presence of a "layered" structure with the presence of horizontal cracks; the presence of these cracks, not found in the other pellets, could be attributed to external factors unrelated to the manufacturing process, such as the method of compression or extraction from the mould.

5.5 Glass production by Spark Plasma Sintering Process

In the following paragraph, the results obtained from experiments aimed at glass production using commercial borosilicate particles through the Spark Plasma Sintering (SPS) process will be presented. Initially, the experimentation focused on evaluating the effect of pressure on sintering while maintaining a constant temperature slightly below the glass transition temperature of the particles under examination (480°C). Two samples (B-T450P1 and B-T450P1.5) were produced, and comprehensive characterization was achieved through in-situ measurements during the SPS process, optical microscopy observations, Raman spectroscopy, scanning electron microscopy (SEM), and relative density measurements.

Subsequently, the development details of the SPS process will be presented, followed by the results of the characterization analyses in the subsequent section.

5.5.1 Experimental work

- B-T450P1

The sample is produced according to the parameters presented in Tab.4

Table 11 SPS process parameters: B-T450P1

Compression			
Compressed pellet mass [mg]	170	*Oil pressure [bar]*	100
Pressure in pre-compacted pellet [MPa]	370	*Oil pressure rate [bar/min]*	0,17
Sintering			
Temperature		**Electric Current**	
Setup Temperature [°C]	450	*Tdown*	1
Dwell time [min]	1	*Tup*	1
Heating speed [°C/min]	100	*N. Pulses (ON)*	12
Cooling speed [°C/min]	430	*N. Pulses (OFF)*	2

A pre-compacted powder pellet weighing 170 mg underwent sintering using the Spark Plasma technique, with an internal pressure of 1 GPa and a process temperature of 450°C. The pellet was held under the conditions for 1 minute, after which the pressure was decreased at the same rate of increment, while the temperature was rapidly lowered.

During the operations, in-situ measurements allowed for the acquisition of the graphs shown in Fig. 13.

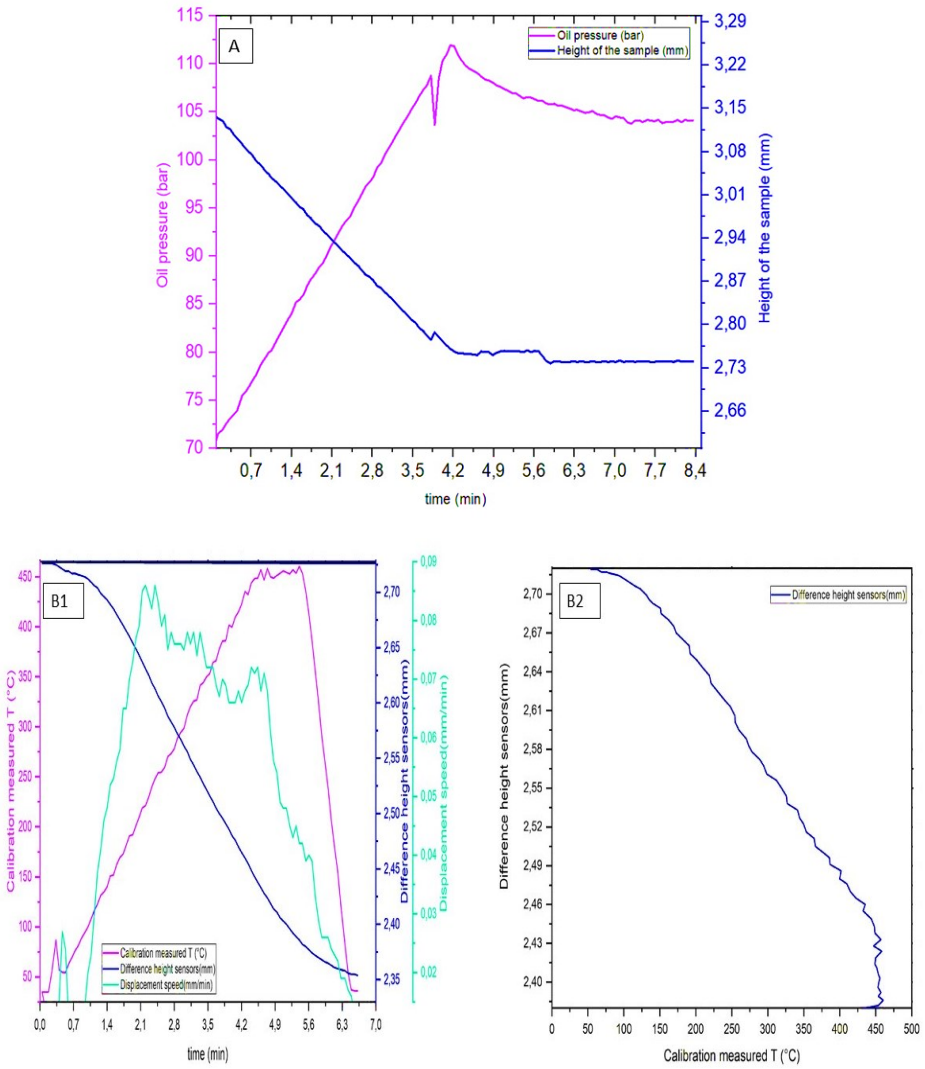

Figure 20 Graphs from in situ measurements at the sintering process for Spark Plasma - (A) compression phase, (B1) - (B2) sintering phase – B-T450P1

During the compression phase (A), a rapid and sudden decrease in pressure was observed at t=3 minutes and an oil pressure of 107 bar, due to an unidentified sudden factor. The initial internal pressure that was intended to be achieved in the sample was 1.5 GPa, but due to this phenomenon, it was decided to interrupt the process and maintain the oil pressure at one hundred bars, resulting in an internal pressure in the sample of 1 GPa. Along with the significant pressure drop, the sample height was also affected. Volumetric shrinkage, corresponding to densification, occurred until reaching 107 bars. It showed a slight variation during the period when the pressure stabilized at one hundred bars and remained constant thereafter.

During the sintering phase (B1), there were no issues with the temperature pattern. The sensors exhibited a progressive decrease in height, and the displacement velocity had two relative maximum values at the following points:

- t=2,216 min, T= 222,214 °C, v=0,086 mm/min
- t=4,472 min, T= 448,6 °C; v=0,071 mm/min

This observation, and in particular the first maximum point, suggests the hypothesis that, under the described pressure conditions, sintering occurs at significantly lower temperatures compared to the process temperature (450°C).

Additionally, Fig4-B2 illustrates that the sintering phase is not complete at the end of the process. The height reduction continues until reaching a height of 2.44 mm but maintains a constant trend at the selected sintering temperature. The region where there is no further height reduction is characterized by a height difference of 0.04 mm.

The sample at the end of the process appears as shown in Fig. 14.

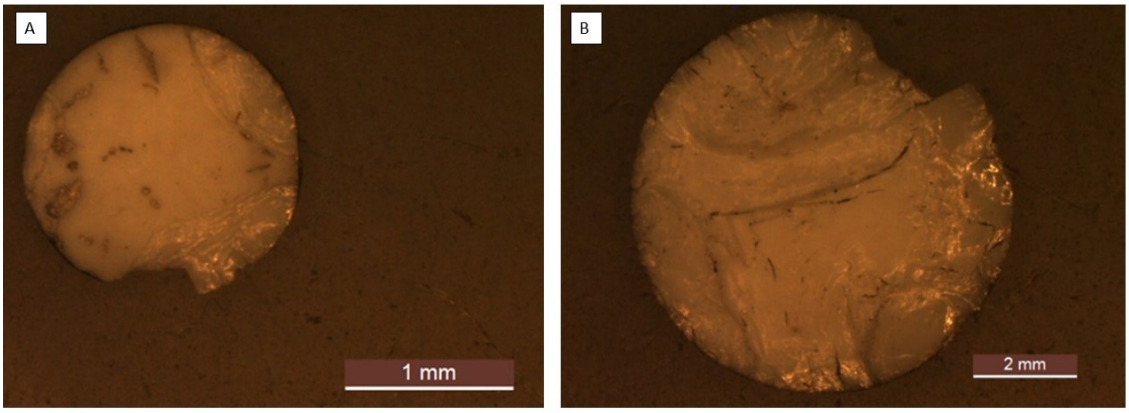

Figure 21 Optical microscope images - (A) lower side; (B) upper side -- B-T450P1

The sample exhibits a white color with the presence of faint translucent areas. Compared to what is achieved through the cold sintering process described in *Chapter 5-Paragraph 5.4.1*, the translucency clearly demonstrates the significant advantage conferred by pressure, thereby emphasizing the crucial role of pressure as a parameter in the development of sintering.

However, the failure to attain transparency indicates incomplete sintering within the sample, as previously shown in the graph of Fig. 13-B2. This condition will be further demonstrated by the obtained value of relative density in Section 5.5.2.3.

- B-T450P1.5

The sample is produced according to the parameters presented in Tab.5.

Table 12 SPS process parameters: B-T450P1.5

Compression			
Compressed pellet mass [mg]	170	*Oil pressure [bar]*	150
Pressure in pre-compacted pellet [MPa]	370	*Oil pressure rate [bar/min]*	0,17
Sintering			
Temperature		**Electric Current**	
Setup Temperature [°C]	450	*Tdown*	1
Dwell time [min]	1	*Tup*	2
Heating speed [°C/min]	100	*N. Pulses (ON)*	12
Cooling speed [°C/min]	430	*N. Pulses (OFF)*	2

A pre-compacted powder pellet weighing 170 mg underwent sintering using the Spark Plasma technique, with an internal pressure of 1.5 GPa and a process temperature of 450°C. The pellet was held under the conditions for 1 minute, after which the pressure was decreased at the same rate of increment, while the temperature was rapidly lowered.

During the operations, in-situ measurements allowed for the acquisition of the graphs shown in Fig. 15.

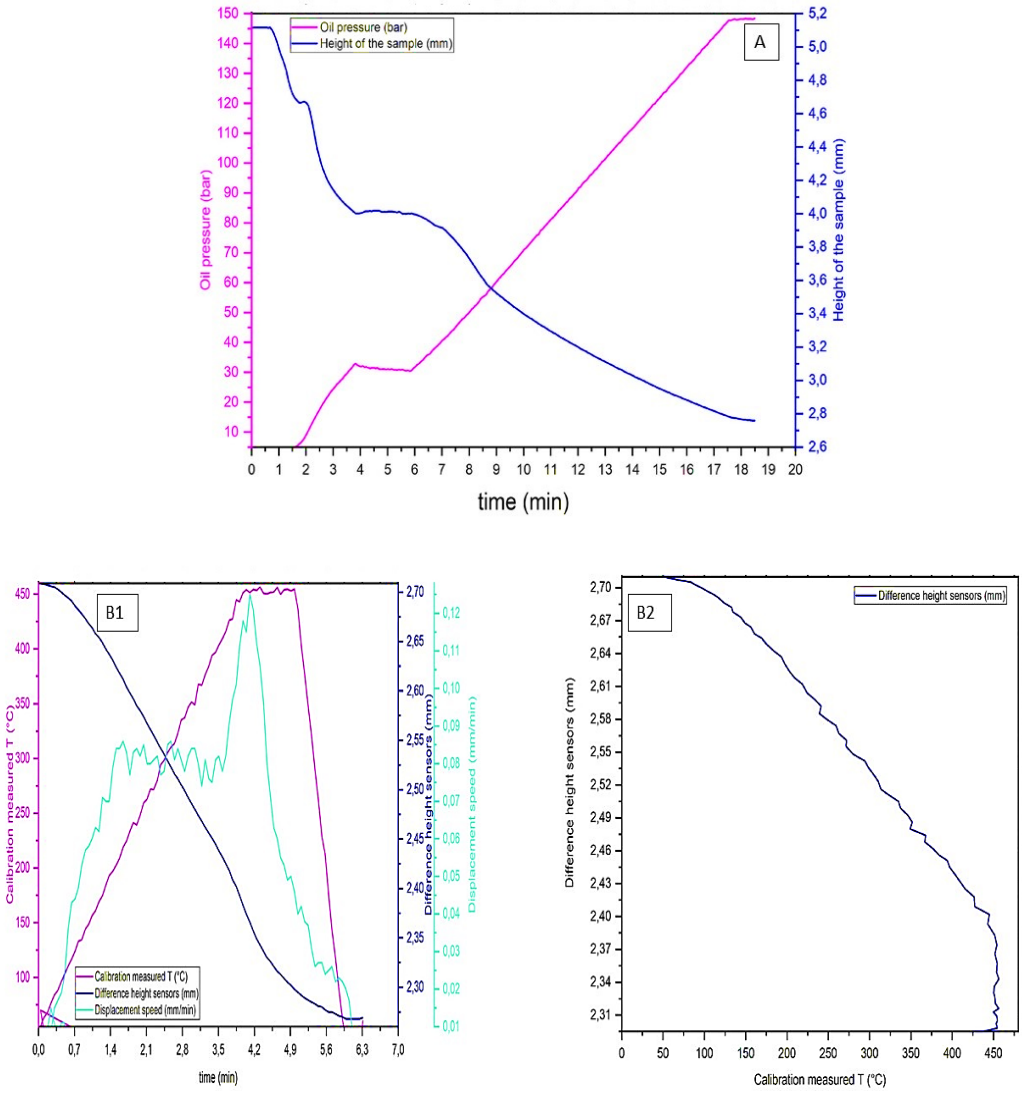

Figure 22 Graphs from in situ measurements at the sintering process for Spark Plasma – (A) compression phase, (B1) - (B2) sintering phase – B-T450P1.5

During the compression phase (A), a gradual increase in pressure is observed without sudden variations over the development time. This already indicates a slight difference compared to the previous analysis of sample B-T450P1. The goal is to reach the desired oil pressure of 150 bar, which corresponds to 1.5 GPa according to the reference calibration graph.

During the sintering phase (B1), an increase in sensor displacement velocity is observed, reaching a peak when the desired process temperature of 450°C is attained. Concurrently, there is an increase in volume contraction, which continues during the time the sample

remains at the process temperature. This indicates that, under the analysed process conditions, sintering occurs as expected. However, Fig.10-B2 reveals that sintering is not yet complete at the end of the process: upon reaching the maximum temperature, there is still a difference of approximately 0.3 mm in sensor height. This condition could potentially be confirmed through pellet optical micrograph evaluation and assessment of the sample's relative density.

The sample at the end of the process appears as shown in Fig. 16.

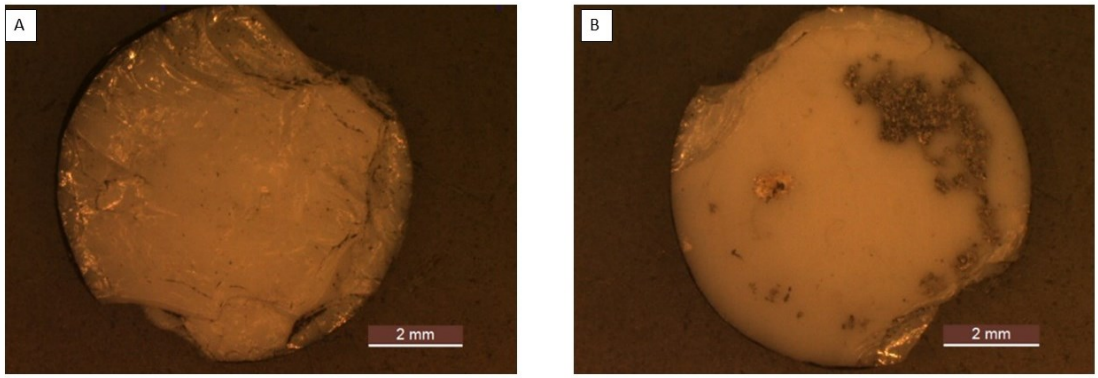

Figure 23 Optical microscope images - (A) lower side; (B) upper side -- B-T450P1.5

After removing the graphite surrounding the pellet, it appears white with the presence of translucent areas; these are mostly found on the periphery of the pellet, on its upper surface, while the lower part of the pellet appears almost completely opaque. The presence of translucency and the absence of transparency confirm the hypothesis of an incomplete sintering process.

5.5.2 Characterization of samples

The produced samples underwent characterization analyses to define their chemical and physical properties. The following paragraph presents the results of Raman spectroscopy, scanning electron microscopy, and Archimedes testing.

5.5.2.1 Raman spectroscopy

Raman spectroscopy analysis was performed on both samples to obtain a precise understanding of the composition of the pellets and the molecular aggregation phase, whether crystalline or amorphous. The spectroscopic analyses were conducted using the methods described in Tab. 6.

Table 13 Raman spectroscopy parameter for both borosilicate glass samples

	First measure	**Second measure**
Acquisition time (s)	60	60
Accumulations	3	3
Instrument	ARAMIS	ARAMIS
Objective	x100	x100
Laser (nm)	HeNe-633	Cobalt 473nm
Spectrum (cm^{-1})	905,075	905,075
Filter (%)	100	100

- B-T450P1

Fig. 17 presents the spectrum obtained from the analysis conducted on sample B-T450P1; (A) represents the results obtained using red laser light, while (B) shows the results from the development of the test using blue laser light.

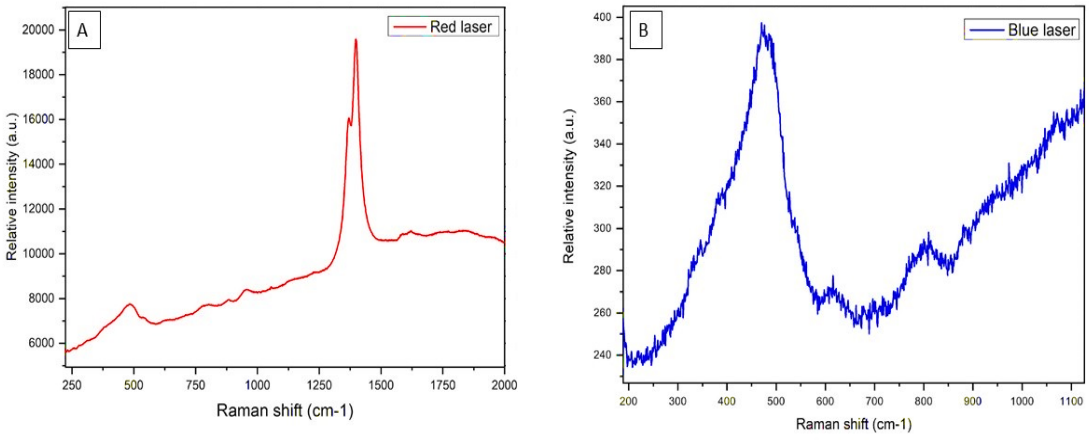

Figure 24 Raman spectra B-T450P1 - (A) Red laser; (B) Blue laser

The graph in (A) exhibits a sharp and prominent peak at a Raman shift of 1400 cm^{-1}, corresponding to a well-known peak in the Raman spectrum of chromium (Cr^{3+}), as

confirmed by the reference citation [*108*]. However, this finding does not align precisely with expectations since the presence of chromium is undesirable and uncommon in typical borosilicate glass. Additionally, the blue laser light reveals a distinct band at a Raman shift of approximately 460 cm^{-1}, precisely corresponding to that of silica. The absence of a sharp peak indicates that the atoms comprising the pellet do not arrange themselves in a well-defined organizational structure, resulting in an amorphous phase. Thus, the condition displayed in (B) demonstrates that, in terms of composition, the starting powder exhibits a significantly higher content of silica compared to boron oxide.

The analysis conducted on sample B-T450P1 consequently reveals two important findings: firstly, the presence of chromium as an impurity, and secondly, the evident mass predominance of silica over boron oxide. Both results, pertaining to the chemical composition, will be investigated through more detailed compositional analyses.

- B-T450P1.5

Fig. 18 displays the spectra resulting from Raman spectroscopy performed on sample B-T450P1.5. The image presents a single graph combining the data obtained using both blue and red laser light.

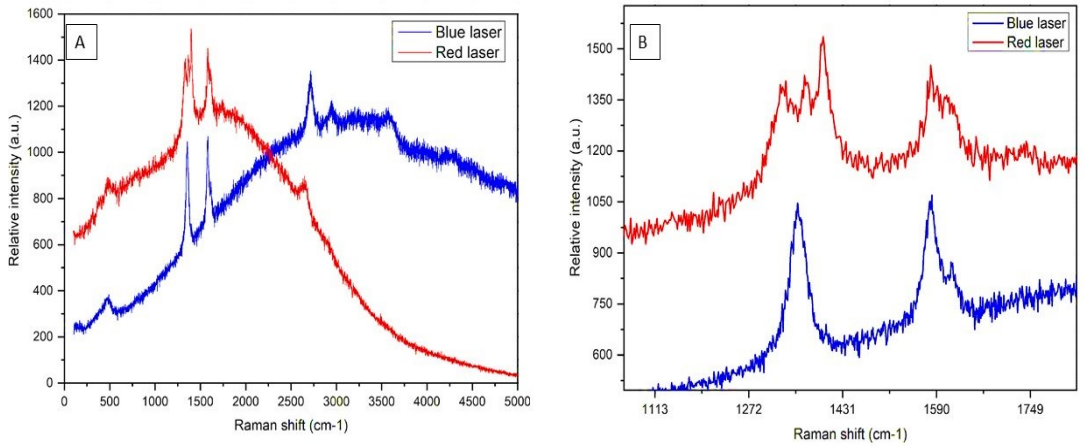

Figure 25 (A) Raman spectra B-T450P1.5; (B) Zoom on 1100-1800 cm-1.

From part (A), two peaks are evident at Raman shifts of 1350 and 1600 cm^{-1}. Both peaks correspond to the bonding vibrations of chromium, specifically in the cationic form of Cr^{3+},

as confirmed by the reference citation [*108*]. The peaks are more pronounced in part (B) and appear as distinct features when the pellet is analysed with blue laser light, but they do not merge into a single peak when analysed with red laser light. The sharpness of the peaks indicates a highly crystalline molecular aggregation phase. This finding suggests that the processing conditions employed for sample B-T450P1.5 led to the formation of undesired crystalline regions in glass production.

In conclusion, like sample B-T450P1, the presence of chromium as Cr^{3+} is observed in the initial powder composition. This reinforces the need for a comprehensive analysis of the commercial powder's chemical composition to accurately define it and confirm or refute the hypothesis of chromium impurities presence. However, the formation of a crystalline phase indicates that the processing conditions may not be appropriate for glass production.

5.5.2.2 SEM

Fig. 19 presents two images obtained from scanning electron microscopy analysis conducted under the conditions described in the Tab. 7.

Table 14 SEM parameters -- B-T450P1,5

	A	**B**
FoV [um]	5	10
WD [mm]	6,76	5,02
Speed	2	3
BC [pA]	22	22
Det	E-T	E-T
Scan Mode	ANALYSIS	UH-RESOLUTION
Energy [keV]	2	2
Mag [kx]	55,8	27,9
Pixel size [nm]	4,88	9,77
Spot size [nm]	5,28	3,17

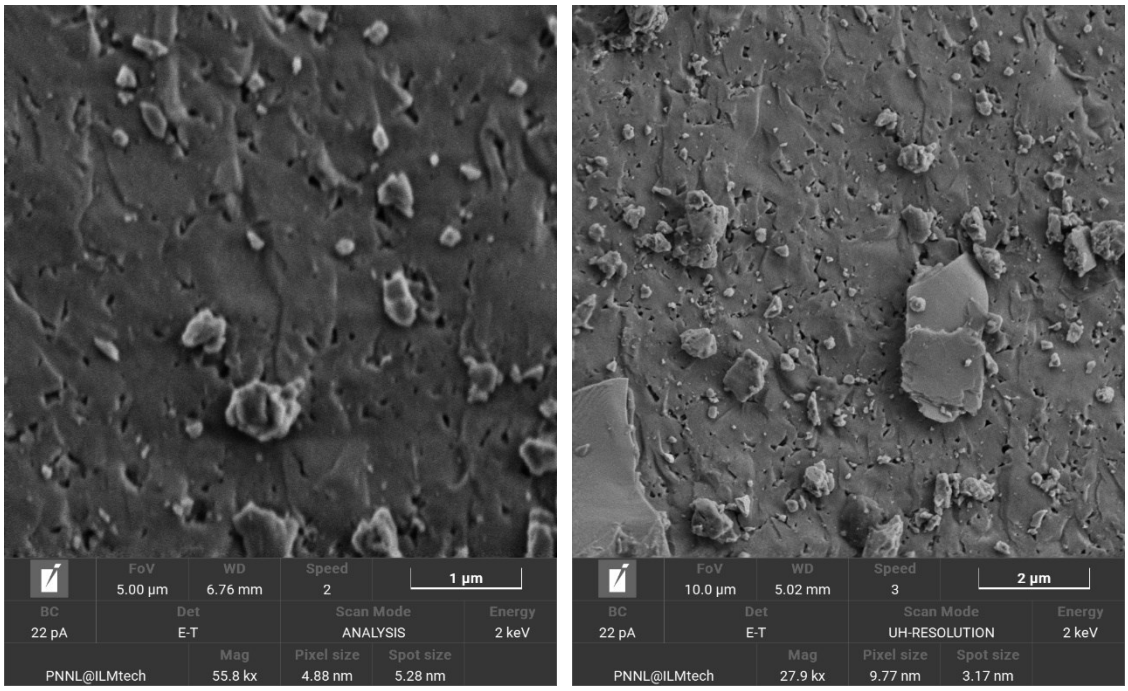

Figure 26 SEM-Images (A), (B); B-T450P1.5

The images depict the surface of the pellet, showing compacted regions and moderately frequent and clearly visible porosity. This observation further confirms what was revealed in Fig. 10-B2, indicating an incomplete sintering process. The pellet surface appears well-defined, but upon closer inspection at higher magnification, distinct geometric shapes with smooth surfaces can be observed.

This corroborates the results from Raman spectroscopy, indicating that the processing conditions employed for sample B-T450P1.5 led to the formation of crystalline phases and, consequently, do not result in the production of glass.

5.5.2.3 Density measurements

The density measurements were conducted using Archimedes' tests, which allow for the evaluation of the samples' relative density compared to the theoretically expected density. The theoretical density considered for evaluation was that of a borosilicate glass with a classical theoretical composition, as described in *Chapter 5, Section 1*.

The obtained results for the relative density of the samples are as follows:

- B-T450P1: 90.48%
- B-T450P1.5: 96.23%

The failure to reach a unity value indicates that the density does not correspond to the theoretical one, confirming what was stated in *Chapter 5-Section 5,4,1*: the sintering process is incomplete for both samples.

Moreover, it should be emphasized that the obtained values of relative density should not be considered in an absolute sense. Considering the uncertain (*Chapter 5, Paragraph 5.2*) chemical composition of the borosilicate glass particles, but only the theoretically hypothesized one, it is reasonable to assume that the actual values of relative density are lower than those obtained. This hypothesis is supported by the micrographs: Fig. 9 and Fig. 11, as described earlier, show the presence of translucent zones that, according to the assumption that the obtained relative densities are accurate, should be more extensive and exhibit translucency tending towards transparency.

Therefore, in this case, the values of relative density should be understood even more as indicative values that provide an insight into what occurred and serve as a starting point for future research.

5.6 Conclusions

In conclusion, the experimentation conducted in this chapter focused on the development of unconventional sintering processes applied to commercial sub-micrometric borosilicate glass powder. Powders consist of agglomerates with an average size of 1260 nm where flakes have a size of 530 nm; glass transition temperature (Tg) is 480°C. The experimentation primarily revolved around the optimization of various parameters for cold sintering, including powder mass, liquid-to-solid ratio, basic solution molarity, pressure, temperature, and dwell time in the mould.

Visual inspections and density evaluations were the primary analyses performed on the produced samples. While visual assessments did not reveal the presence of either transparent

or translucent regions, density analysis provided the maximum relative density achieved for sample “15M,5T,40P-30”. The failure to achieve 100% relative density strongly suggests that sintering was not completed under the specified conditions.

From the SEM analysis, any fracture surfaces in the sample couldn’t be found. However, we observed bubbles on the inner surface, likely due to the higher temperature used during pellet creation. This emphasizes the need for a more detailed study of temperature's impact on pellet production. Additionally, we noticed that the "2M, 2T, 40P-15" sample has lower porosity and better compaction compared to others. This suggests that the specific combination of parameters used for this sample promotes better particle compaction. The amount of liquid phase relative to the solid phase might have played a role, as it's higher in this sample compared to the "15M, 2T, 20S-120" sample, which has a layered structure. In the latter case, although particles within each layer are well compacted, there are separation zones between the layers, making it less compact, as confirmed by the relative density value (90.26%).

Subsequently, the same powder underwent Spark Plasma Sintering (SPS) with pressure as the variable parameter while keeping temperature (450°C, just below the powder's Tg) and dwell time (3 minutes) constant. The results clearly indicate that, under the tested conditions, the sintering process was not completed, as evidenced by the low relative density achieved. This observation is further supported by in-situ measurements during process development.

In summary, the experimentation conducted highlights several aspects that need to be considered in future research. The SPS process may require higher pressures and longer dwell times than those used in this study to achieve not only translucency but also closer to transparency in the fabricated pellets. Thus far, the results do not rule out the possibility of applying the SPS process to borosilicate glass microparticles to obtain transparent pellets.

However, it is crucial to consider the effect of particle size. Both unconventional sintering processes revealed incomplete sintering, with SEM images demonstrating the presence of internal porosity. The particles used in this study were notably larger compared to those in the previous chapter's experimentation, where the objectives were successfully achieved.

Therefore, future research should involve the use of nanometric-sized particles, similar to those found in the treated silica, to enhance the likelihood of achieving the desired outcomes.

CHAPTER 6

Glass production from the synthesis of glass nanoparticles at low Tg

The next chapter delves into the synthesis of glass nanoparticles with a low glass transition temperature. As discussed in previous chapters, particle size is crucial for the sintering of transparent glass components. A low glass transition temperature allows for sintering at lower temperatures on the freshly formed particles.

In the following sections, various synthesis methodologies for the nanoparticles developed during experimentation will be presented. Produced particles will undergo characterization analysis to assess their size, structure, chemical composition, and glass transition temperature.

6.1 Synthesis of glass nanoparticles

The synthesis of glassy nanoparticles is a crucial field in materials engineering, with significant applications in sectors such as optics, electronics, and biomedicine. Nanoparticles are characterized by extremely small sizes, typically less than 100 nanometres, and offer a wide range of advantages due to their amorphous structure. The most common method for their production is the sol-gel process, often associated with the renowned Stöber process. This approach involves the conversion of chemical precursors, such as silicates or metallic alkoxides, into a sol-gel solution that, through a polymerization process, leads to the formation of glassy nanoparticles. However, the versatility of this method allows for targeted modifications of the nanoparticles' properties. For instance, the size and shape of the nanoparticles can be set by altering synthesis conditions, such as precursor concentration or reaction temperature [*109*]. Furthermore, the surface of the nanoparticles can be functionalized with specific chemical groups to impart desired properties, such as the ability to bind to biomolecules or contrast agents for medical imaging. The sol-gel approach, with its flexible synthesis process and the potential for nanoparticle customization, continues to be a vital tool in the design of advanced materials.

6.1.1. Sol-gel process

The sol-gel process represents a colloidal chemical method characterized by the preparation of a colloidal suspension, termed "sol." This is followed by sol gelation and subsequent elimination of the liquid residing in the interconnected channels of the gel. The resulting material is then subjected to drying at temperatures below 100°C.

The conversion steps from the solution into a dense material are elucidated in Fig. 1, which also illustrates the diverse array of products achievable through the sol-gel process. These products can encompass dense ceramics, thin films, fibres, and nanometric particle powders. Their production begins with a sol-gel synthesis process, followed by various subsequent processing steps tailored to yield the specific product.

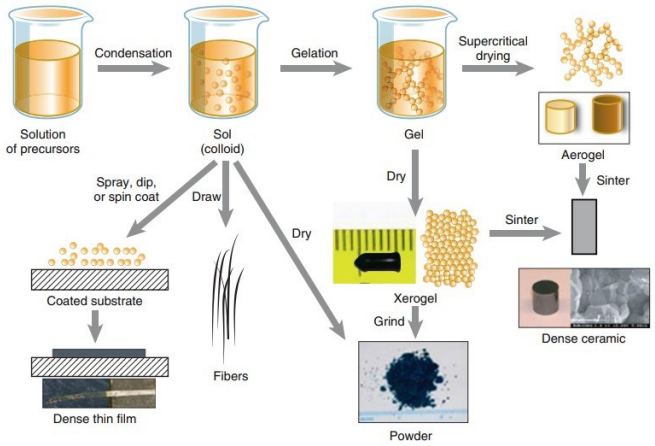

Figure 27 Sol-gel process scheme: steps and products [110]

Metallic salts, metallic alkoxides, or more intricate organometallic precursors undergo hydrolysis and polycondensation to yield a gel matrix. Owing to the immiscibility of organometallic precursors and water due to the hydrophobic nature of alkyl groups, the inclusion of a common solvent, typically an alcohol, is imperative to facilitate homogeneous mixing. In the typical scenario employing alkoxides as precursors, hydrolysis takes place, usually under the influence of either an acidic or basic catalyst.

Hydrolysis and condensation reactions assume pivotal roles in governing the sol-gel process. Common precursors employed in the sol-gel process are typically found in the form of

compounds with the general formula $M(OR)_n$, MX_n, or $R'\text{-}M(OR)_{n-1}$, where M represents a metal centre with a specific oxidation state denoted by n, X and RO stand for common departing groups frequently associated with metallic salts or metallic alkoxides, for instance, chloride ions in metal halides. Meanwhile, R' denotes any organic group that forms covalent bonds with the metal centre (e.g., Si-C, Sn-C) or attaches through coordination ligands when dealing with metals like titanium (Ti) or zirconium (Zr).

Equation 1 portraits reaction involved in sol-gel process.

$$Hydrolisis \qquad M - OR + H_2O \rightarrow M - OH + ROH \qquad (1)$$

$$Condensation \qquad \begin{cases} M - OH + XO - M \rightarrow M - O - M + X - OH \\ M - OH + XO - M \rightarrow M - (OH) - M - OX \end{cases}$$

The formation mechanism initiates with the hydrolysis of an alkoxide group, or the deprotonation of a water molecule linked to the metal centre, resulting in the production of a hydroxide. The resulting hydroxide species has the potential to participate in interactions with other metal centres via condensation reactions, leading to the formation of oligomers. This condensation process may involve the creation of either an oxo bridge, resulting in the removal of water or alcohol, or a hydroxide bridge. In essence, these two fundamental steps occur concurrently rather than sequentially. The structure, connectivity, and morphology of the final inorganic network are significantly influenced by the relative contributions of the three reactions.

To achieve end products characterized by micro or nanometric dimensions, it is plausible to circumvent the gel formation phase by initiating nucleation followed by controlled growth via diffusion. Furthermore, expediting the hydrolysis reaction is feasible through catalysis, rendering the environment either acidic or basic, conditional upon the specific reaction being executed.

In conclusion, sol-gel process is an alternative approach to the conventional glass production technique involving melting and tempering. Its applications span a wide range, including the fabrication of glass coatings, bulk glass, nanoparticles, and powders.

6.1.1.1 Stöber synthesis method

The use of colloidal suspensions, in the form of hydrosols and aerosols, enables the production of a suspension consisting of homogeneous particles with uniform size and shape. In the latter half of the last century, Stöber introduced a synthesis process that made it possible to produce monodisperse suspensions composed of silica spheres in the colloidal size range, specifically with diameters ranging from 50 nm to 2 µm.

Since it has been demonstrated that silica particles can be generated through a chemical reaction involving tetra esters of silicic acid [*111*], the synthesis method employed involves the reaction between a silicon alkoxide, known as tetraethyl orthosilicate (TEOS), and water in an alcoholic solvent. As previously mentioned, the presence of a catalyst, either acidic or basic, accelerates the reaction. In the Stöber process, the use of ammonia as a catalyst creates a basic environment conducive to the reaction. Fig. 2 schematically illustrates this process.

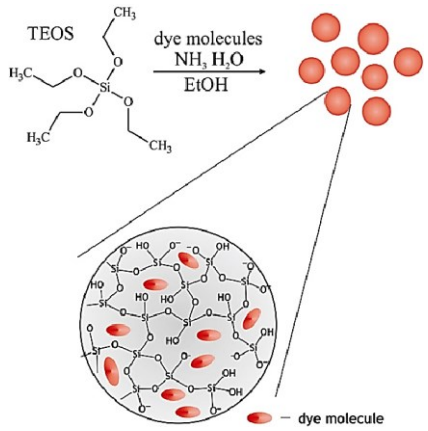

Figure 28 Schematic representation of Stöber process [111]

The size of the particles obtained depends on the concentrations of water and ammonia. The relationship between particle size and concentrations of reactants is depicted in Fig. 3, showing that larger particle sizes are formed with increasing concentrations of water and ammonia, resulting in a broader particle size distribution, until a maximum.

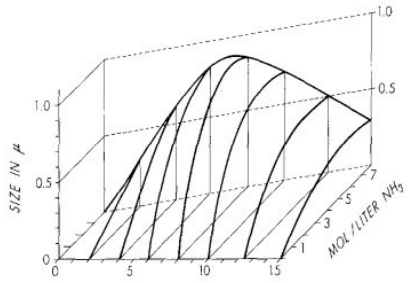

Figure 29 Trend in particle size based on water and ammonia concentration.

The choice of solvent also plays a significant role: using ethanol and n-butanol as alcoholic solvents, Stöber observed that the latter solvent produces larger particle sizes. Furthermore, Stöber conducted a systematic investigation into the influence of different concentrations of water, ammonia, and ethyl ester within the ethanol-ethyl ester system. The condensation rate is strongly dependent on the water content in the system. In the absence of ammonia, silica aggregates into irregularly shaped particles, and spherical shapes cannot be observed under the electron microscope. Ammonia thus acts as both a basic catalyst for alkoxide hydrolysis and a shaper of particle morphology, imparting them with a spherical form.

It is possible to evaluate the size of the nanoparticles produced using the Bogush Formula (Equation 2), which is valid for determining sizes in the range of 5-500 nm. [112]

$$d = A[H_2O]^2 \exp\left(-B[H_2O]^{\frac{1}{2}}\right) \quad (2)$$

where:

$$A = [TEOS]^{\frac{1}{2}} (82 + 151[NH_3] + 1200\,[NH_3]^2 - 366[NH_3]^3) \quad (2A)$$

$$B = 1{,}05 + 0{,}523[NH_3] - 0{,}128[NH_3]^2 \quad (2B)$$

This formulation is the result of fitting a large number of experiments, and its interpolation is represented in Fig. 4 [*113*].

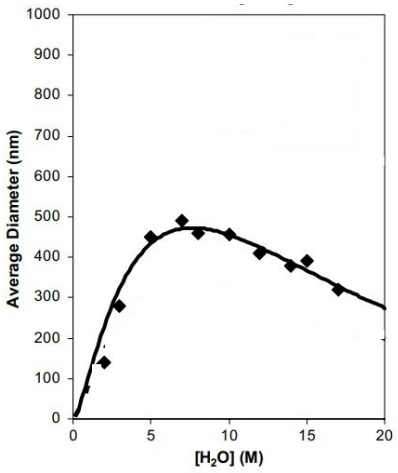

Figure 30 Interpolation curve from Bogush results [113]

However, it's worth noting that this formula contains a topographical error, which can be approximated to around 20%. This discrepancy can sometimes mislead users into thinking that the synthesis has not been conducted optimally.

In conclusion, the Stöber process presents an ideal model for harnessing colloidal phenomena. It is a straightforward synthesis process that yields nanostructured particles, which hold great promise for various applications in the fields of medical and materials engineering.

6.1.1.2 Modified Stöber synthesis methods

By varying the synthesis parameters in the sol-gel process, it is possible to obtain homogeneous materials with tailored properties, including significant chemical and thermal stability, excellent mechanical strength, high optical transparency, and controlled porosity. The final product obtained through sol-gel synthesis is characterized by its *mesoporous* structure, an intrinsic feature of sol-gel materials. Furthermore, this technique allows for the direct synthesis of high-purity multi-component materials, avoiding the use of powder intermediates or expensive vacuum-based processing techniques. These advantages make the sol-gel method a promising synthesis route for preparing a wide range of functional materials with different structures and porosity. Modifications to the Stöber synthesis process are

typically made to produce components such as bioactive glasses, mesoporous glass particles, and other specialized materials.

Microemulsions, for example, [114] are typically produced based on sol-gel glasses, where the aqueous phase consists of silicate precursors and metal ions in addition to catalysts. During the production phase, a catalyst, typically CTAB, is commonly added. In sol-gel synthesis, CTAB serves as a pore-forming agent, reducing volumetric shrinkage, preventing cracking, and eliminating the need for supercritical drying. As catalysts, because they activate the hydrolysis reaction very quickly, strong inorganic acids such as sulfuric acid (H_2SO_4), hydrochloric acid (HCl), and nitric acid (HNO_3) are also frequently used [*115*].

The Stober synthesis can be customized not only based on the catalyst employed but also by selecting the desired components for glass composition. *Bioactive silicate* glasses are distinguished by their remarkable capacity to interact with biological tissues, forming robust bonds with them. In recent years [*116*], formulations have been developed that enable the creation of bioactive glasses using sol-gel techniques, facilitating the attainment of this property by promoting the formation of a SiO_2–CaO–P_2O_5 system. To achieve the desired glass characteristics, precursors of phosphorus and calcium oxides are introduced alongside the silica precursor in concentrations that induce network formation.

Conversely, *phosphorus-based* glasses are not uncommon [117]. The sol-gel synthesis of phosphorus-based glasses is considered rigorous but typical in biomedical applications [117]. These glasses exhibit a substantial presence of phosphates, and it is not uncommon to introduce metallic oxides (titanium dioxide, ferric oxide, copper oxide) to improve the stability of the inherently unstable phosphorus oxide glass.

Modifications to the Stober synthesis process involve adjustments to both process phases and the formulation of chemical solutions. The inclusion of additional precursors alongside TEOS naturally prompts a consideration of the necessary quantities of these precursors and other reagents. This, in turn, necessitates the development of new synthesis steps that can facilitate complete hydrolysis and condensation reactions, thereby leading to the desired final properties.

Consequently, the Stober synthesis is refined to encompass multiple sequential process steps [*118*], with a particular emphasis on the precise introduction of precursors and the duration of their mixing with the solution.

The modifications to the Stober synthesis process presented here represent the current state of research, yielding products with the intended characteristics. Given the numerous parameters that influence Stober synthesis, it is conceivable that multiple variations could be explored to optimize the process according to specific desired outcomes.

6.2 Production of low Tg glassy nanoparticles

Drawing from the insights gained in the preceding section on chemical synthesis, the focus now shifts towards a detailed exposition of the conducted experiments. The starting point is the classical Stöber synthesis, with a gradual progression through various synthesis phases. The foundational hydrolysis and condensation reactions that define the Stöber method remain integral throughout. The upcoming discussion provides a comprehensive breakdown of the methodologies employed, with specific attention on systematic alterations in parameter values. Subsequently, the subsequent section delves into an analysis of outcomes resulting from these parameter changes, aiming to decode their impact on the overall process. This naturally transitions to a meticulous examination of the results obtained from an array of characterization analyses, providing a comprehensive understanding of the experimental outcomes.

6.2.1 Synthesis optimization

The production of low glass transition temperature (Tg) glassy nanoparticles was initiated by referencing a previously conducted thesis work at the University of Padua [*119*]. The synthesis process described in the referenced work was replicated to generate the starting sample referred to as "FG63," maintaining the same nomenclature as in the original reference. The process flow is depicted in Fig. 4.

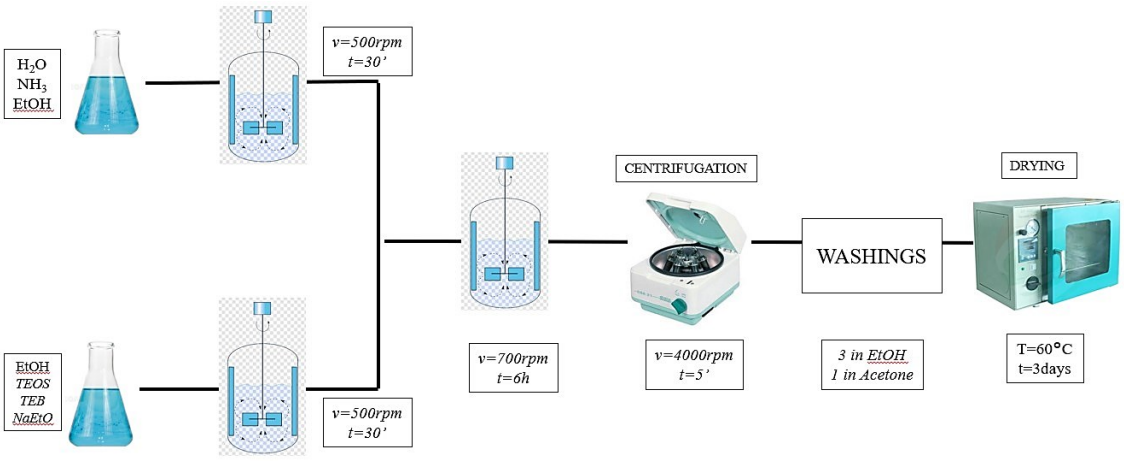

Figure 31 Process scheme_sample "FG63"

The employed method is a modified version of the Stöber synthesis, with specific alterations. This process involves two separate solutions: one containing water, ammonia, and ethanol, and the other containing precursors diluted to 5% in ethanol. The chosen precursors, sodium ethoxide and triethyl borate, serve to lower the glass transition temperature. After 30 minutes of individual stirring of these two solutions, they are combined to form a single solution. During this stage, the stirring speed is increased compared to the initial stirring phase, aimed at reducing gel formation probability. The mixing duration lasts for 6 hours. Following the mixing phase, during which hydrolysis and condensation reactions take place, an intermediate centrifugation step is conducted.

Subsequently, repeated washes are performed using ethanol and acetone (two ethanol washes and one acetone wash). The resulting product is then subjected to drying at 60°C for 3 days to remove residual solvents to the greatest extent possible.

Once the process was developed, the next step involved analysing the influence of the two precursors, in addition to tetraethyl orthosilicate: triethyl borate and sodium ethoxide. With this objective in mind, two distinct syntheses were conducted, one lacking sodium ethoxide and the other lacking triethyl borate. The sample "SB_01" was produced using a process development approach identical to that employed for the "FG63" sample, as outlined in Fig. 6.

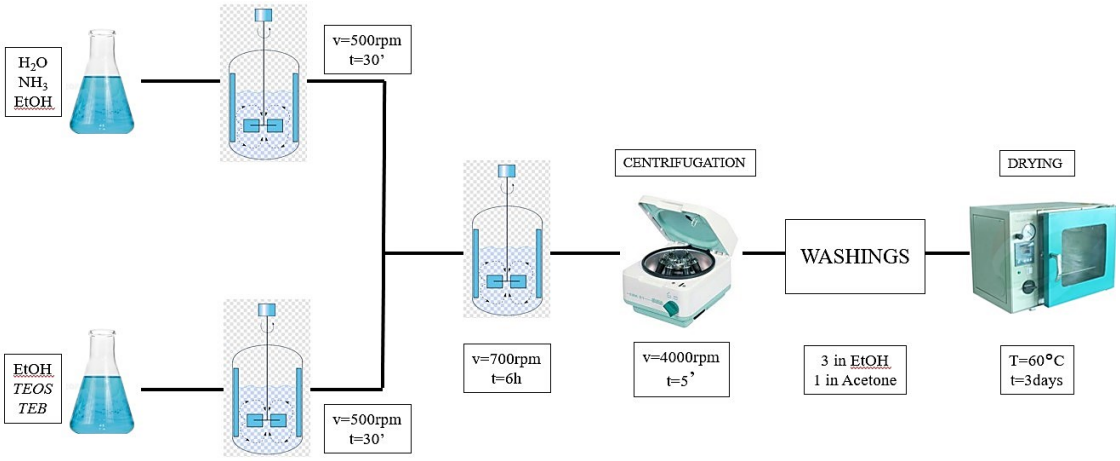

Figure 32 Process scheme_sample "SB_01"

The synthesis procedure entailed the presence of two separate solutions (one containing solvents and the other containing precursors diluted in ethanol), which were mixed individually for 30 minutes and then combined and mixed at a higher rate for 6 hours. Subsequent steps included centrifugation, washing, and drying to conclude the process.

Despite maintaining an unaltered synthesis process, it is important to emphasize that the quantities of precursors employed were as advised by the bibliographic reference [*119*]: the molar ratio of [TEB] to [TEOS] is 1.157, the total precursor concentration is 10M, and the precursors are diluted to 5%.

The synthesis in which the missing precursor is triethyl borate aimed at producing the sample "SNa_02." With reference to the bibliography [*118,119*], the developed synthesis process followed the same production phases as the previously mentioned samples, with the following parameters: [NaEtO]/[TEOS] = 2.086, a total precursor concentration of 10M, and a 5% dilution of the precursors.

However, as evident from Fig. 7, the synthesis operations were halted after 65 minutes of mixing the complete solution.

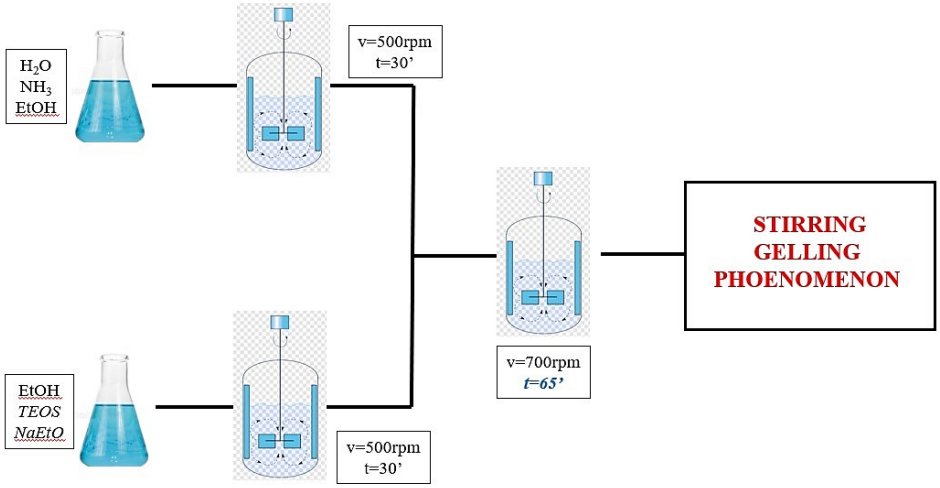

Figure 33 Process scheme_sample "SNa_02"

A gelation phenomenon was observed, which delayed the proper progression of the process and the formation of particles. It can be observed that the gelation effect was exclusively attributed to the presence of sodium ethoxide and the consequent absence of triethyl borate. Triethyl borate is not only responsible for the incorporation of boron oxide into the silica network but also for preventing gelation during the synthesis process.

Having evaluated the influence of the precursors through the synthesis and characterization tests presented below, the phase of optimizing the synthesis process begins to take shape and become more substantial. Referring to [*120*] and Fig. 8, modifications were made to the process phases, opting to introduce the same precursors used thus far, diluted to the same value (5%) in ethanol.

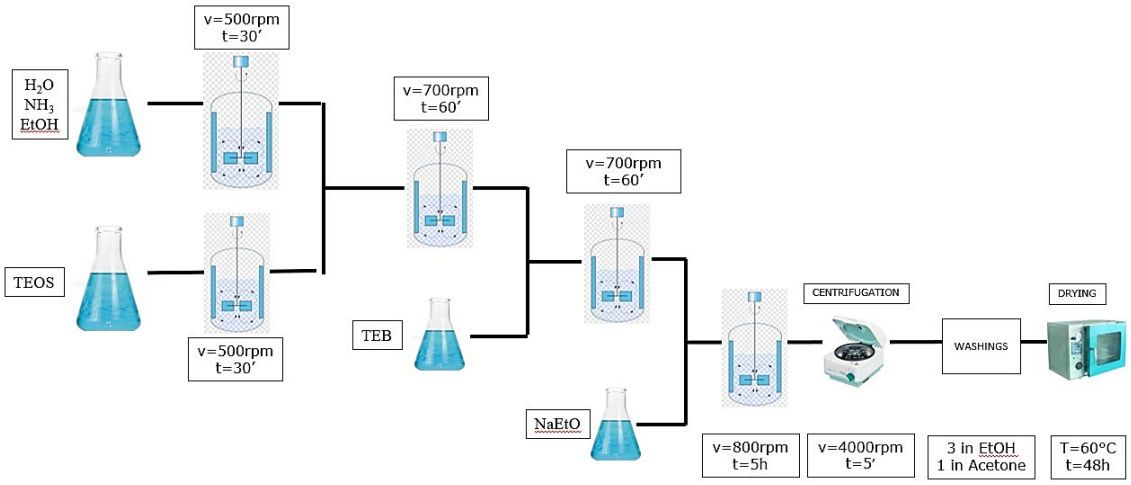

Figure 34 Process scheme_sample "SBNa_03"

The chemical parameters were altered and set as follows: the molar ratios of triethyl borate and sodium ethoxide to TEOS are 1.1248 and 0.8866, respectively, while the total precursor concentration is 24M.

The new synthesis process, still based on the Stöber synthesis, involves the gradual and separate addition of the precursors to the initial solution containing water, ammonia, and ethanol. For each individual precursor, the "solution + precursor" system is stirred at a rate of 700 rpm for 60 minutes. The first precursor to be added is tetraethyl orthosilicate, followed by triethyl borate and then sodium ethoxide. The complete solution containing all the precursors is then mixed at a higher rate of 800rpm for a duration of 5 hours. Subsequent steps of centrifugation, washing, and drying are performed according to parameters held consistent with the previous synthesis operations.

Observing from the characterization tests presented in Chapter 6, Paragraph 6.2.2, that the synthesis steps performed can bring about positive modifications aligned with the experimentation goal, the sample "SBNa_04" was conducted following the same procedures as the previous sample. Fig. 9 depicts the process scheme.

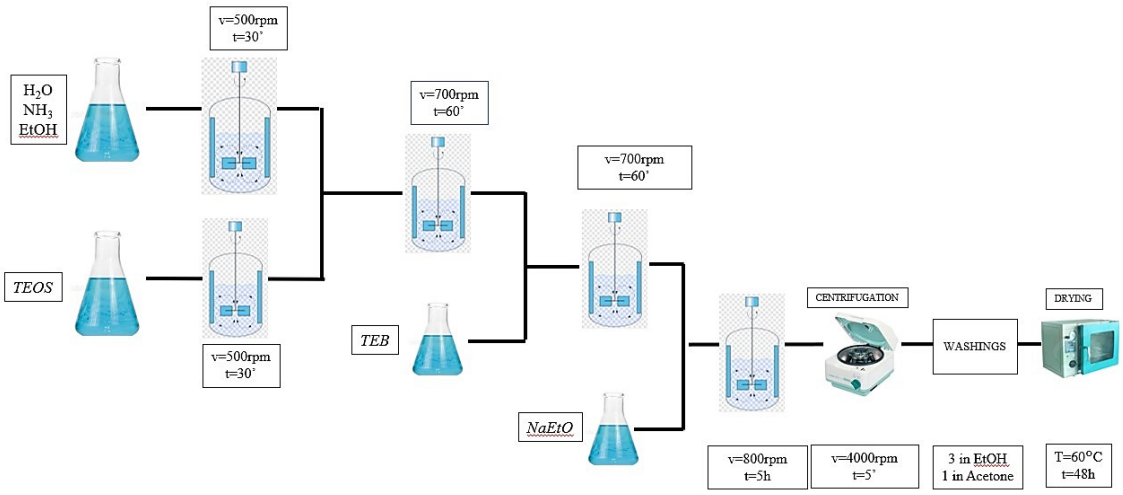

Figure 35 Process scheme_sample "SBNa_04"

Precursors, molar ratios, process steps were all kept constant; only a single modification was introduced concerning the quantity of the precursors. Specifically, these precursors were diluted to 2% in relation to ethanol, as opposed to the 5% utilized thus far.

Continuing the process optimization by altering one parameter at a time to assess the influence of each parameter on the synthesis, the sample "SBNa_05" was created as follows: precursor dilution remained at 2%, consistent with the previous sample; the same molar ratio values were maintained, along with the same concentration. However, the process scheme was reverted to that of the initial reference sample "FG63" [*119*]; therefore, the synthesis no longer involves the gradual addition of precursors, but rather the direct combination of the initial precursor solution with the solution composed of water, ammonia, and ethanol.

The centrifugation, washing, and drying operations remained unchanged. A representative process scheme is depicted in Fig. 10.

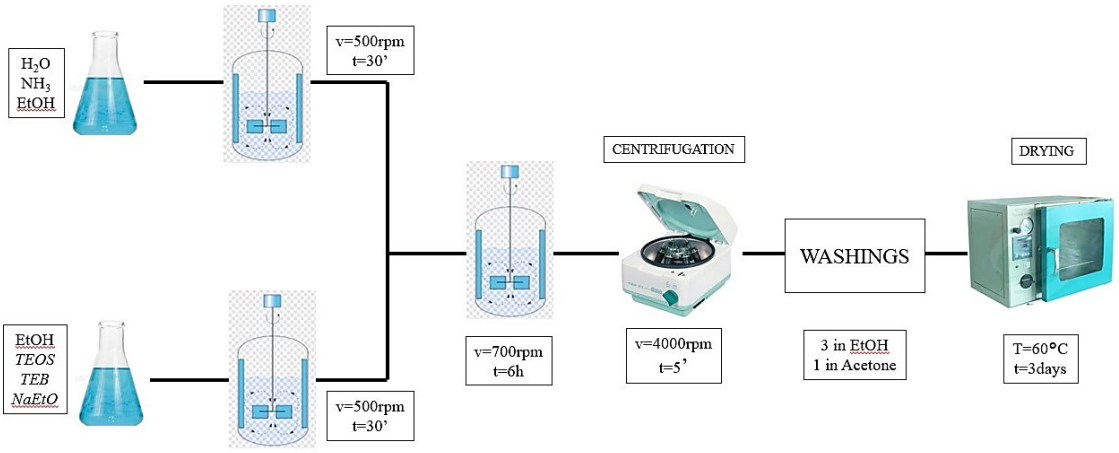

Figure 36 Process scheme_sample "SBNa_05"

After analysing the process optimization conditions concerning the actual synthesis phase and the molar quantities of reagents, the influence of the drying phase on the entire nanoparticle fabrication process is considered. As illustrated in Fig. 11, for the creation of the sample "SBNa_06," the same synthesis process developed for the just-discussed sample "SBNa_05" was followed: the precursor solution, initially separated from the solution containing ammonia, was subsequently added to the latter at a rate of 700rpm for 6 hours.

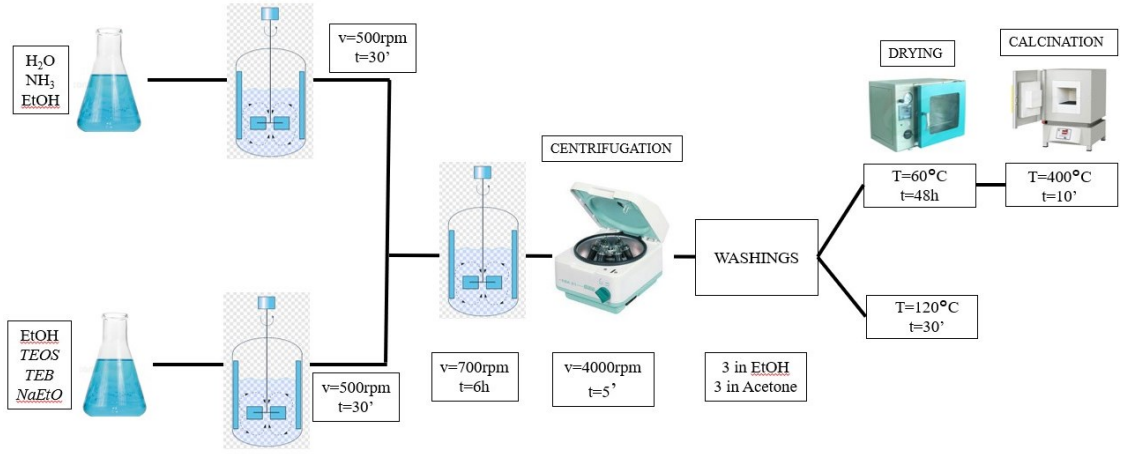

Figure 37 Process scheme_sample "SBNa_06"

Following centrifugation and washing operations, the drying phase was conducted as follows: approximately half of the washed product was dried at a temperature of 60°C for 48 hours, consistent with the previous synthesis operations, with the addition of a subsequent

calcination phase at 400°C for 10 minutes. The remaining portion was dried at 120°C for 30 minutes.

The latest synthesis process conducted demonstrates significant differences compared to the previous ones. Referring to [*121*] and Fig. 12, the synthesis of the "SSrCa_01" sample is as follows: eliminating ethanol, a solution of water and ammonium hydroxide is mixed at 600rpm for 10 minutes. Subsequently, the precursors – TEOS, calcium tetrahydrate nitrate, and strontium chloride – are added dropwise in the quantities stated in the reference.

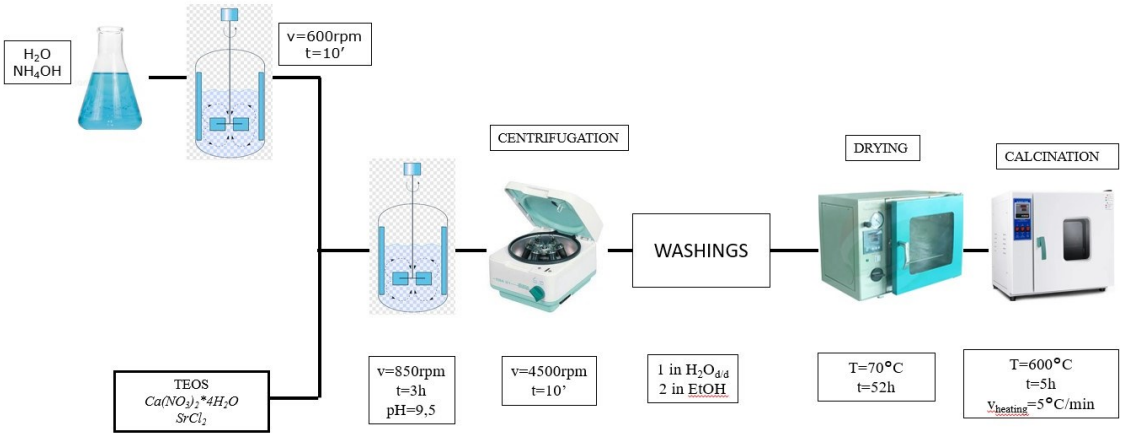

Figure 38 Process scheme_sample "SSrCa_01"

The resulting basic solution (pH=9.5) is subjected to vigorous stirring (at 850rpm) for 3 hours, followed by centrifugation at 4500rpm for 10 minutes. It has to be noted that the pH analysis was conducted as a preliminary assessment: if complete precipitation had not been achieved during the washing procedures, which could likely stem from a variation in the centrifugation speed parameter, a dilution process would have been pursued; The pH evaluation would thus have facilitated an informed decision regarding the choice of reagent for achieving the required solution dilution.

Washing steps include one with distilled water and two with pure ethanol. Removal of the liquid phase is facilitated first by drying at 70°C for 52 hours and then by calcination with a gradual temperature increase (5°C/min) to 600°C for 5 hours.

Compared to the previous synthesis operations, the following variations introduced by this new process should be noted: a fundamental change lies in the precursor selection, where triethyl borate and sodium ethoxide are replaced with strontium chloride and calcium nitrate hydrate. As described in the reference [*121*], these compounds, upon oxide formation, can lead to a reduction in glass transition temperature through the creation of a well-connected network with that of silica. Introduction of the precursors in solution, mixing phase, centrifugation, and washing are characterized by different methods and parameters, a condition mirrored in the drying phase.

6.2.2 Nanoparticles characterization

The samples produced through the chemical syntheses are in the form of particles that necessitate characterization analyses to assess features such as composition, average size, shape, and glass transition temperature. Therefore, the results of the conducted analyses are presented below, with specific attention given to the discrepancies or similarities between samples based on the same types of analyses they were subjected to.

6.2.2.1 FT-IR

The FT-IR analysis, performed as described in Chapter 3, was the chosen method to enable the identification of functional groups, and consequently, the composition of each particle sample created through the synthesis processes outlined in the previous section. Therefore, it concerns an analysis that involved each of the produced samples, and the results will now be presented in the following, progressively highlighting the differences and similarities among the samples, in comparison with the anticipated outcomes from the chemical synthesis.

In the following Fig. 13, the graph depicting the relationship between wavenumber and absorbance for the "FG63" sample is presented. The graph is compared to the FTIR spectrum obtained from a sample of silica nanoparticles synthesized using the classical Stöber synthesis process; this synthesis operated under the following conditions: [H2O] =6.6M, [NH3]=1.8M, [EtOH]=18.01, [TEOS]=0.3M. It is important to underline that this comparison is crucial to outline the main differences resulting from the application of

synthesis processes, namely the Stöber method (SiO_2) and the modified Stöber process described in the previous section (FG63).

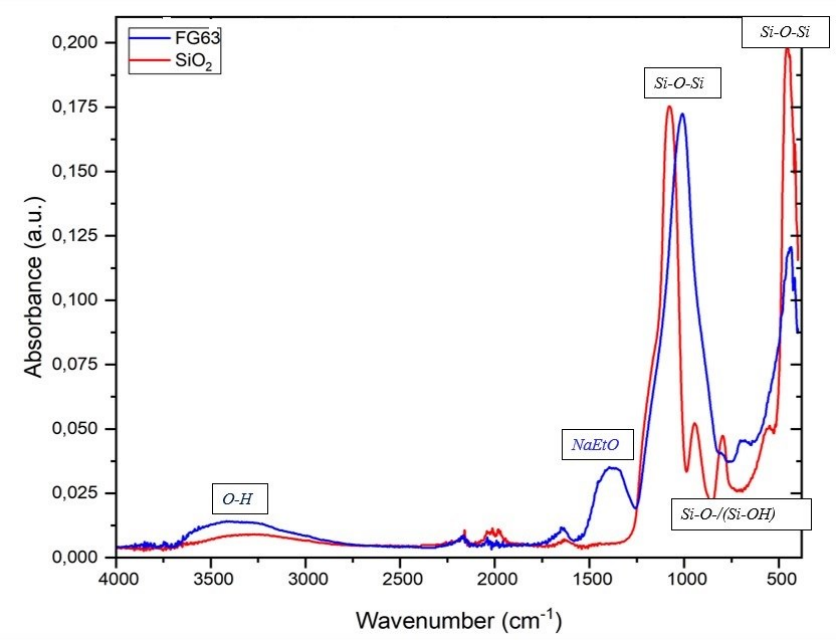

Figure 39 FTIR analysis for compositional evaluation of particle samples "FG63" and "SiO2"

The modifications introduced in the synthesis process, as anticipated, exhibit the emergence of additional peaks in the regions corresponding to bond vibrations involving the newly introduced elements, namely boron and sodium, through the new precursors. While recognizing the presence of boron, whether in oxide form or bound within the silica lattice, might pose challenges, the characteristic bond vibrations of sodium ethoxide are distinctly recognizable. In this regard, the pertinent FT-IR diagram is documented in the literature [*122*].

Tab. 1 and 2 provide the correlation between wavenumbers and corresponding types of bonds, respectively for the silica produced through the classical Stöber synthesis and the FG63 sample, generated through the modified Stöber synthesis.

Table 15 Composition analysis through peak assignment indicating bond vibrations sample SiO2.

SiO2			
Reference wavenumber [cm-1]	*Wavenumber [cm-1]*	*Abs [a. u]*	*Bond type*
450	456,0824	0,2	Si-O-Si
1075	1078,9773	0,1728	
800	796,4568	0,04483	
940-960	944,9488	0,0497	Si-O-/(Si-OH)
530	548,6489	0,04874	C-O-Si
3333-3267	3244,6454	0,009029	C≡H

Table 16 Composition analysis through peak assignment indicating bond vibrations sample FG63.

FG63			
Reference wavenumber [cm-1]	*Wavenumber [cm-1]*	*Abs [a. u]*	*Bond type*
450	450,297	0,11865	Si-O-Si
645	649,8934	0,04404	[*122*]
661	657,6072	0,04482	[*122*]
1075	1008,5882	0,17235	Si-O-Si
1338	1373,0685	0,03479	*Na-C*
3333-3267	3224,9573	0,01384	C≡H

The Fourier Transform Infrared (FTIR) analysis conducted on the sample labelled as "SB_01," with the results highlighted in Figure 14, has revealed the presence of characteristic bonds associated with silicon and boron [*123*]. Furthermore, the presence of organic groups and water molecules has been detected, which were not successfully removed despite attempts through a drying process.

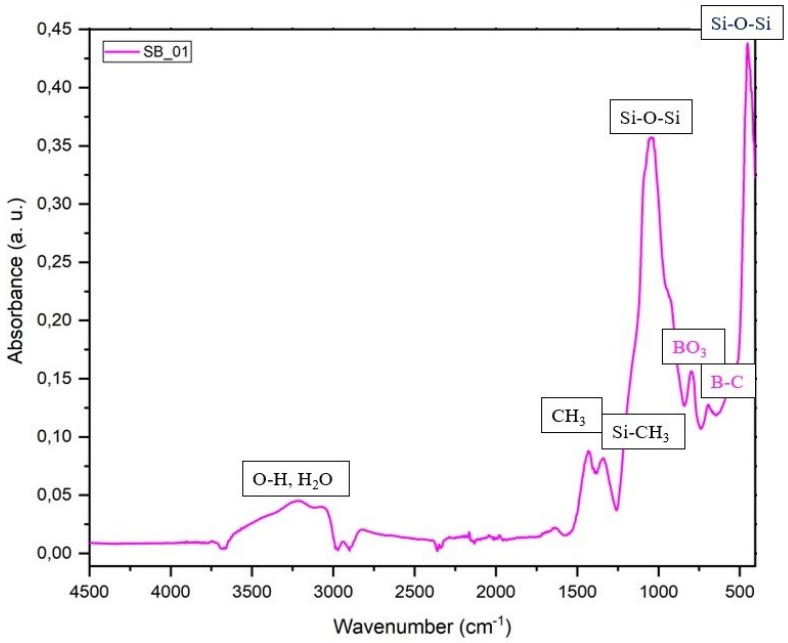

Figure 40 FTIR analysis for compositional evaluation of particle samples "SB_01"

Tab. 3 provides a detailed interpretation of the vibration bonds within the formed particles.

Table 17 Composition analysis through peak assignment indicating bond vibrations sample SB_01

SB_01			
Reference wavenumber [cm-1]	*Wavenumber [cm-1]*	*Abs [a. u]*	*Bond type*
440	428,1197	0,39539	C_3B
450	453,1897	0,43562	Si-O-Si
620	622,8948	0,0369	B-C
663	666,2853	0,11985	BO_3
1022	1033,6583	0,35484	CH_3
	1042,3364	0,3552	CH_3
1260	1255,432	0,02923	$Si-CH_3$
1362	1338,3561	0,05804	CH_3
1075	1051,0145	0,35493	Si-O-Si
3333-3267	3391,209	0,02601	OH, H_2O
	3293,8215	0,02276	

Already from the tabulated representation of this sample, a distinct feature emerges that will be of particular interest throughout the experimental investigation: boron exhibits strong affinity to oxygen, thereby forming boric anhydride. At times, it also forms bonds with

carbon, which is part of the lattice structure and is introduced through the organic precursors used. However, in the case of this specific sample, boron does not form significant bonds with silicon. Instead, silicon attempts to create a lattice arrangement known as "Si-O-B." This arrangement is of utmost importance as it plays a fundamental role in reducing the glass transition temperature [*110*].

The interconnection bond between silicon and boron through an oxygen bridge is not formed by modifying the synthesis steps while keeping the precursor concentrations and molar ratios unchanged. As highlighted by Figure 11, in fact, the absorbance spectrum shown for the "SBNa_03" sample is like the one previously developed for the "FG63" sample.

Furthermore, Figure 15 and Tab. 4 illustrate how the absorbance spectrum of the "SBNa_03" sample aligns with that of the "FG63" sample, further supporting the absence of interconnection bond formation between silicon and boron through an oxygen bridge.

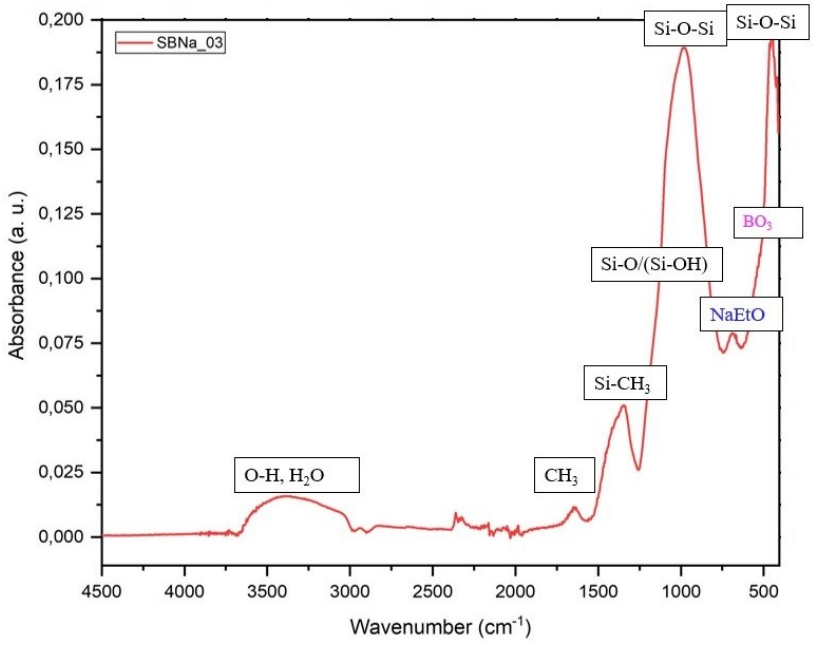

Figure 41 FTIR analysis for compositional evaluation of particle samples "SBNa_03"

Table 18 Composition analysis through peak assignment indicating bond vibrations sample SBNa_03

SBNa_03			
Reference wavenumber [cm-1]	*Wavenumber [cm-1]*	*Abs [a. u]*	*Bond type*
363	319,4416	0,17794	C_3B
440	437,762	0,18585	C_3B
	446,4401	0,19486	C_3B
450	452,2255	0,19503	Si-O-Si
620	616,1452	0,07516	B-C
663	655,6788	0,07493	BO_3
698	691,3554	0,07892	[*122*]
782	759,816	0,07299	[*122*]
800	762,7087	0,07281	Si-O-Si
960	990,2687	0,18905	Si-O-/(Si-OH)
970			CH_3
1050	1033,6583	0,17858	Si-O-Si
1338	1338,3561	0,17625	[*122*]
1362	1347,0342	0,17251	CH_3
1385	1384,6393	0,04572	CH_2
1429	1415,4948	0,04233	[*122*]
3400	3812,5791	0,01546	OH, H_2O
	3625,7178	0,00702	

The absorbance curve does not undergo significant changes for the "SBNa_04" sample, which was obtained using the same synthesis process as the previous sample, with the variation of precursor dilution. As evidenced by Fig. 16, and even more notably by Tab. 5, the bonding vibrations occur at the same wavenumbers as observed in the previous sample. Any differences are solely present in the intensity of the absorbance, and these minimal variations can be neglected.

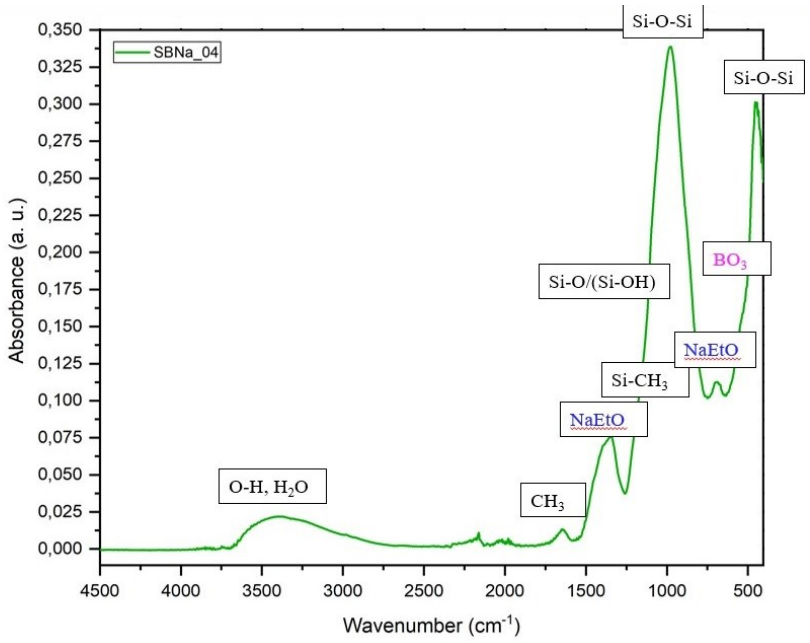

Figure 42 FTIR analysis for compositional evaluation of particle samples "SBNa_04"

Table 19 Composition analysis through peak assignment indicating bond vibrations sample SBNa_04

SBNa_04			
Reference wavenumber [cm-1]	*Wavenumber [cm-1]*	*Abs [a. u]*	*Bond type*
363	412,6919	0,26382	C_3B
440	434,8693	0,29594	C_3B
	444,5116	0,30118	C_3B
450	454,154	0,30142	Si-O-Si
663	642,1795	0,10416	[*122*]
620	623,8591	0,10549	B-C
663	670,1423	0,11061	BO_3
698	691,3554	0,0,11241	[*122*]
782	759,816	0,10292	[*122*]
800	762,7087	0,10301	Si-O-Si
970	976,7087	0,33883	CH_3
1050	1053,9072	0,2764	Si-O-Si
1338	1338,3561	0,07498	[*122*]
1362	1347,0342	0,07567	CH_3
1385	1384,6393	0,07069	CH_2
1429	1417,4948	0,06155	[*122*]
3400	3812,5791	0,002292	OH, H_2O
	3625,7178	0,00814	

However, a comparable scenario arises in relation to the "SBNa_05" sample: increasing the dilution of the precursors does not seem to facilitate the development of interatomic bonds that could lead to a reduction in the glass transition temperature. As illustrated in Fig. 17, analogous to the findings for the preceding samples, the presence of boron and silicon individually bonded to oxygen, clearly defined organic groups, and water becomes apparent.

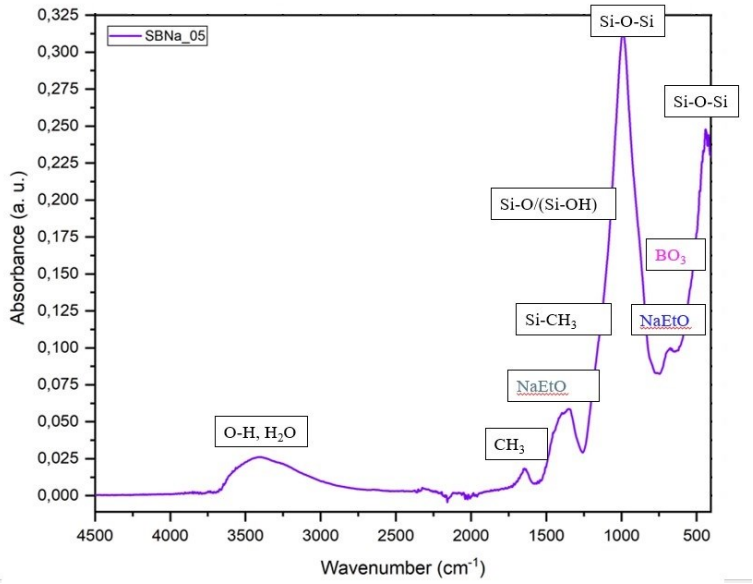

Figure 43 FTIR analysis for compositional evaluation of particle samples "SBNa_05"

Even by subjecting the produced powder to a higher temperature of 120°C for 30 minutes, complete removal of water is not achieved. This is evident from Fig. 18 and Tab. 6, which present a comparison between the absorbance curves obtained for the powder dried at 60°C and 120°C. Remarkably, there are no significant differences in terms of elimination of hydroxyl and organic groups. The curve's behaviour and the types of bonds appear almost unchanged compared to the FG63 sample.

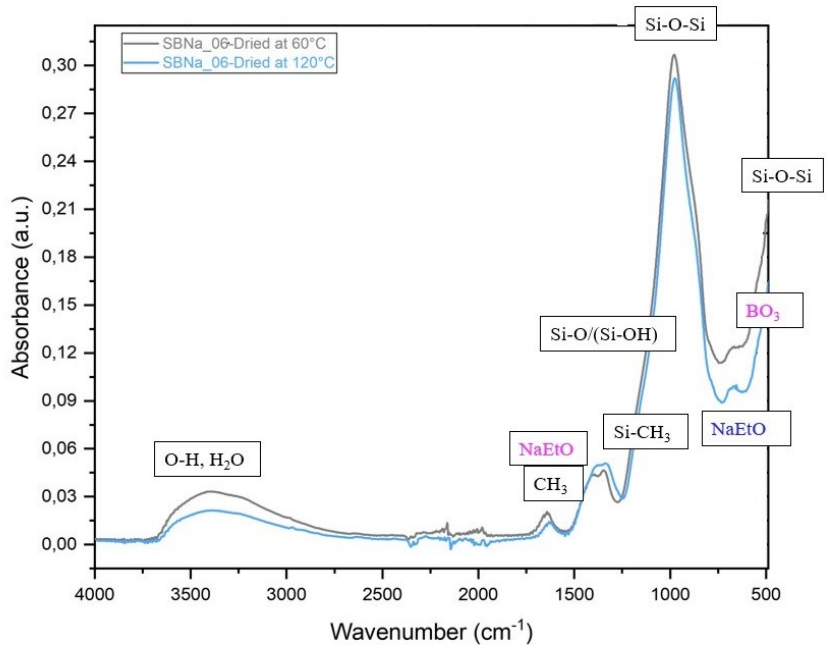

Figure 44 FTIR analysis for compositional evaluation of particle samples "SBNa_06"

Table 6 Composition analysis through peak assignment indicating bond vibrations sample SBNa_06 dried at 120°C.

SBNa_06 dried at 120°C			
Reference wavenumber [cm^{-1}]	*Wavenumber [cm^{-1}]*	*Abs [a. u]*	*Bond type*
363	419,4416	0,24203	C_3B
620	622,8948	0,09909	B-C
663	666,2853	0,10288	BO_3
698	695,2123	0,10093	NaEtO FTIR diagram
800	810,9203	0,10683	Si-O-Si
1050	986,4108	0,29497	Si-O-Si
1338	1350,8911	0,05083	NaEtO FTIR diagram
1385	1382,7108	0,04979	CH_2
3400	3818,3645	0,00241	OH, H_2O
	3625,7178	0,0111	

A distinct situation, however, emerges for the "SSrCa_01" sample, whose FTIR analysis was conducted before and after calcination at 600°C at temperature higher than those used in the previous synthesis processes. Fig. 19 illustrates the resulting graphs in comparison, while Table 7 provides correlation between wavenumbers and bonding vibrations.

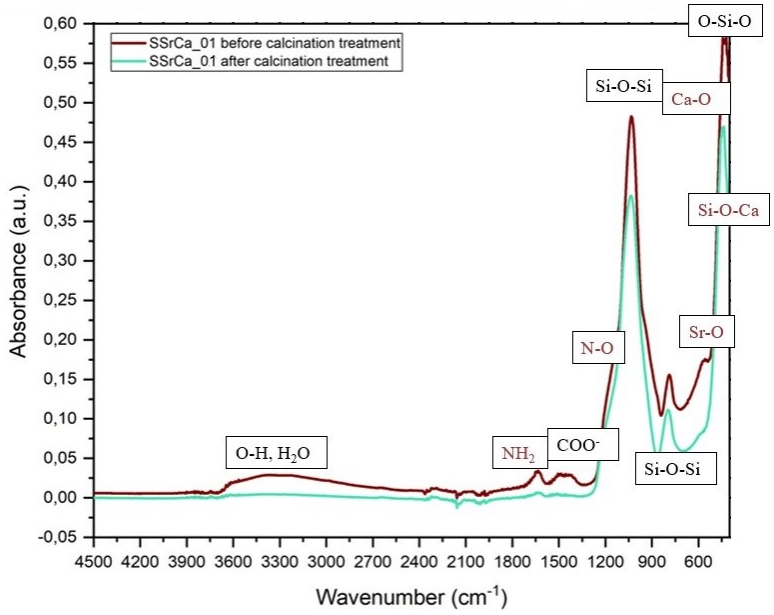

Figure 45 Composition analysis through peak assignment indicating bond vibrations sample SSrCa_01

Table 7 Composition analysis through peak assignment indicating bond vibrations sample SSrCa_01 pre- and post-calcination.

SSrCa_01				
		Before TT	*After TT*	
Reference wavenumber [cm-1]	*Wavenumber [cm-1]*	*Abs [a. u]*	*Abs [a. u]*	*Bond type*
450	450,297	0,54739	0,46294	O-Si-O
550	554,4343	0,1744	0,0886	Ca-O
597	598,786	0,15809	0,07895	Sr-O
800	785,8503	0,1557	0,10783	Si-O-Si
930	931,4495	0,20381	0,13591	Si-O-Ca
950	949,77	0,22398	/	Si-OH
1180	1218,7911	0,0835	0,07144	N-O
1398	1397,77	0,02478	/	NO_3^-
1407	1402,9567	0,02516	/	COO-
1500	1490,705	0,02952	/	COO-

1520	1520,5962	0,02656	0,0048	NH_3
1595	1597,7349	0,02093	/	NH_2
1600-1640	1600-164	0,00424	/	O-H
1650	1643,0538	0,03283	0,00578	NH_3
1706	1715,3713	0,01726	/	COOH
300-3500	300-3501	0,2884	/	O-H

The graphs and the table clearly demonstrate the removal of hydroxyl groups upon calcination, making it evident that drying at 70°C (as indicated by the brown curve) is insufficient for water elimination. The principal bonding vibrations persist: Si-O-Si, as well as those characteristics of strontium oxide and calcium oxide, referenced respectively in [*124, 125*]. The bonding vibration associated with the amine group [*126*] is also noticeable, along with the presence of carbonate groups, which are only partially removed through the calcination step. The Sr-O-Ca bond is also observed, albeit as a peak of weak intensity. However, once again, the bridging oxygen bond between silicon, strontium, and/or calcium is absent. This bond is crucial for the formation of the lattice that leads to the reduction in glass transition temperature.

From the analyses conducted on all the samples, the following fundamental characteristics can be outlined in conclusion:

- The performed syntheses have resulted in the formation of particles characterized by the presence of silica and oxides, generated through the introduction of precursors. However, the formation of a lattice involving the interconnection of silicon atoms with atoms from the precursors did not occur. Such a lattice could have potentially facilitated a reduction in the glass transition temperature (Tg).
- The syntheses exhibit a clear presence of organic material introduced by the precursors themselves. However, the drying steps were not directly aimed at the elimination of this material; rather, they were targeted at the removal of the hydroxyl group associated with water. Notably, a more effective removal of water was demonstrated through calcination treatment at 400°C.

6.2.2.2 SEM

Fig. 16, 17, 18 presents images obtained from scanning electron microscopy analysis; this analysis is carried out for “FG63”, “SBNa_04”, “SBNa_05”, the three samples, which can be compared in terms of synthesis development and precursor dilution.

The SEM analysis enabled the assessment of the particle sizes of the obtained powder. The initial examination of the acquired dimensions revealed conspicuous particle aggregation, prompting the evaluation of the diameter on a limited number of particles. However, this constraint did not compromise the ultimate result.

The study, primarily conducted through the "ImageJ" analysis software, represents a statistical evaluation pertaining to the selected particles for analysis. The obtained values for each sample are presented below.

- FG63

Fig. 20 depicts the appearance of particles for the "FG63" sample, while the Tab. 8 presents the conducted statistical investigation on these particles.

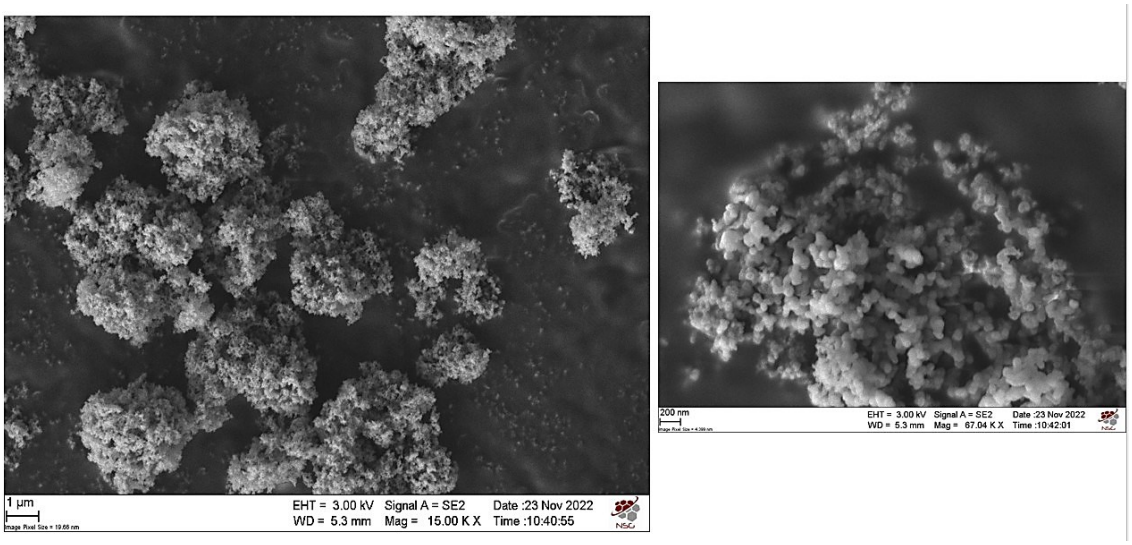

Figure 46 SEM image sample "FG63"

Table 8 Statistical analysis sample "FG63"; UCL and LCL represent "Upper control limit" and "Lower control limit" respectively.

Mean Diameter [nm]	***Standard Deviation***	***Minimum***	***Maximum***	***UCL***	***LCL***
115,58	13	91,442	131,86	76	154,8906

- SBNa_04

Fig. 21 depicts the appearance of particles for the "SBNa_04" sample, while the Tab. 9 presents the conducted statistical investigation on these particles.

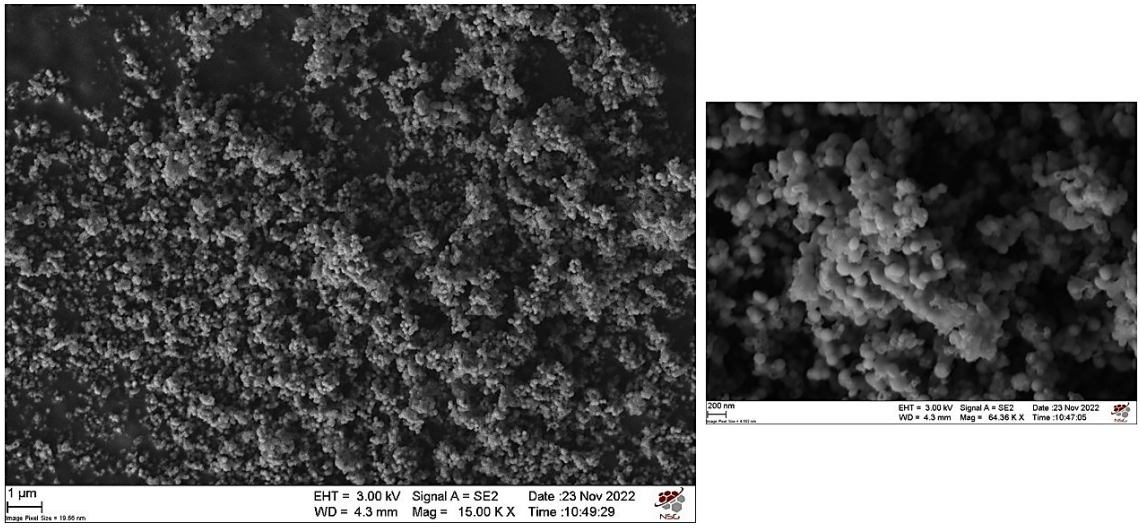

Figure 47 SEM image sample SBNa_04

Table 9 Statistical analysis sample "SBNa_04"; UCL and LCL represent "Upper control limit" and "Lower control limit" respectively.

Mean Diameter [nm]	***Standard Deviation***	***Minimum***	***Maximum***	***UCL***	***LCL***
146,816	45	94,505	241,999	12	282,0905

- SBNa_05

Fig. 22 depicts the appearance of particles for the "SBNa_05" sample, while the Tab. 10 presents the conducted statistical investigation on these particles.

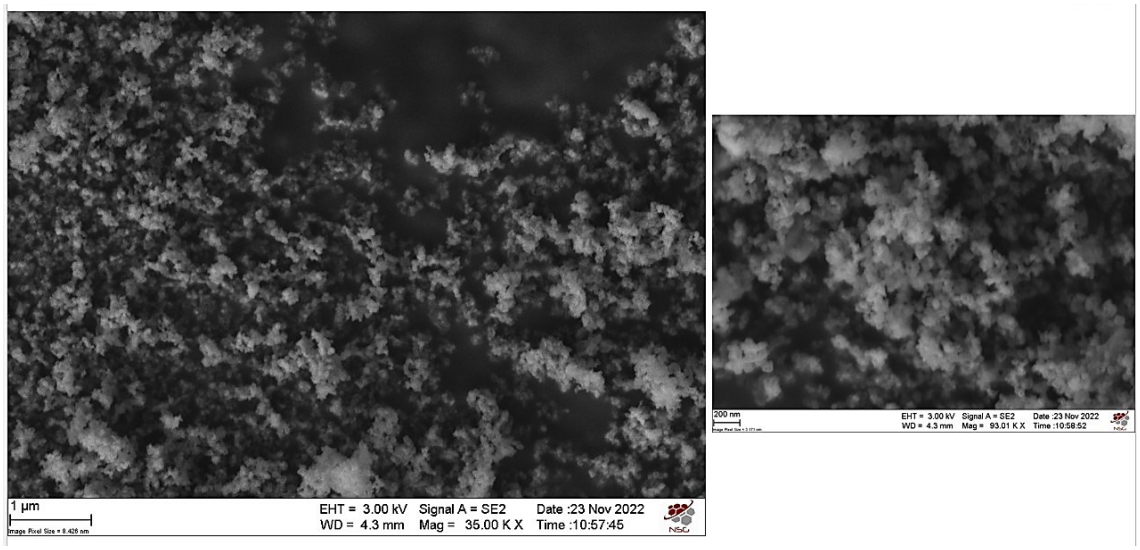

Figure 48 SEM image sample SBNa_05

Table 10 Statistical analysis sample "SBNa_05"; UCL and LCL represent "Upper control limit" and "Lower control limit" respectively.

Mean Diameter [nm]	***Standard Deviation***	***Minimum***	***Maximum***	***UCL***	***LCL***
113,42	18	57,226	145,255	60	166,665

The examination of the obtained values yields a significant insight: the resulting powder particles exhibit dimensions at the nanometric scale, with diameters hovering around 110nm. This dimension aligns harmoniously with the dimensions outlined in the pertinent thesis project. It's noteworthy that the standard deviation inherently encapsulates the repercussions of particle aggregation. From these results, it can confidently assert that the achieved results show a characteristic of notable dispersion. This dispersion, in turn, can be deemed quite acceptable, particularly in the case of the "FG63" and "SBNa_05" samples, where the standard deviation ranges between 13 and 18.

6.2.2.3 Drop-casting

The organic material present in the synthesized particles, as discovered through SEM analysis (Section 6.2.2.1), is examined in detail using Drop-Casting analysis, carried out as described in Chapter 3, Section PP. Figures 23, 24, and 25 respectively depict how the "FG63," "SBNa_03," and "SBNa_04" samples appear in Phase A and Phase B. Phase A represents the particles immediately after being placed on the cut silica glass substrate, while Phase B represents them right after undergoing thermal treatment at 700°C for 10 minutes.

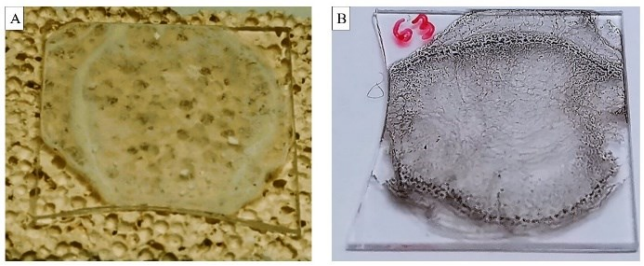

Figure 49 Drop casting analysis before (A) and after (B) thermal treatment _sample "FG63"

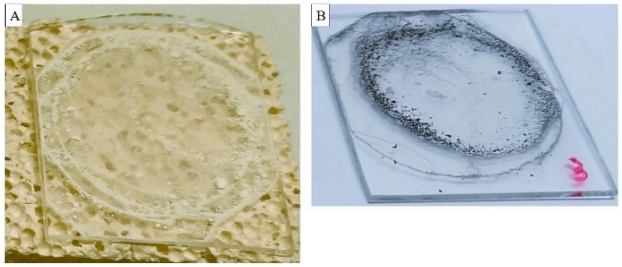

Figure 50 Drop casting analysis before (A) and after (B) thermal treatment _sample "SBNa_03"

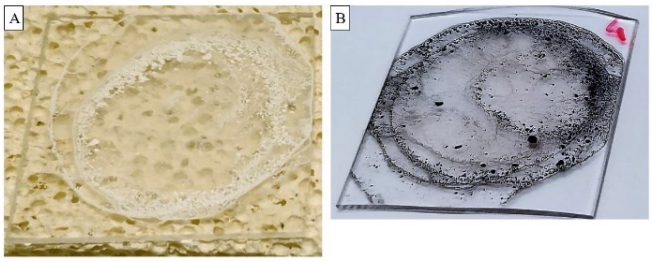

Figure 51 Drop casting analysis before (A) and after (B) thermal treatment _sample "SBNa_04"

Initially, the particles exhibit a white appearance when placed on the silica substrate at room temperature. The white colour appears even more vivid along the edges of the glass slide; this significant accumulation of particles at the edge of a droplet is attributed to the phenomenon known as the "coffee ring effect," commonly observed in the drop casting process. Consequently, the necessity of the thermal treatment in the furnace at T=700°C becomes even more pronounced. However, after the thermal treatment, they adopt a dark, black colour. This alteration suggests that the black colour results from the combustion of the organic component. At the operating temperature, the organic portion of the particles has undergone combustion, leading to the development of the black hue. Remarkably, this organic matter persists even when subjected to high-temperature treatment (700°C), as shown in the analysis.

6.2.2.4 DLS

The Dynamic Light Scattering (DLS) analysis, briefly mentioned in Chapter 3, involved four samples: "FG63", "SBNa_03", "SBNa_04", and "SBNa_05". The DLS analysis entails an initial step of powder dispersion, crucial for evaluating particle diameter using the appropriate instrument. However, achieving dispersion was not straightforward for any of the four samples. Therefore, prior to presenting the final analysis results, the steps taken to achieve dispersion are detailed below.

Initially, an attempt was made to disperse particles by placing 2mg of powder per ml of ethanol, with a total volume of 5ml. Despite using a high-speed agitator for dispersion, the powder remained visible in the solution for each sample, and precipitates formed shortly after agitation ceased.

A second dispersion attempt was conducted, involving the use of ultrasonic systems. Each sample in the previously prepared solution ("powder ethanol" system) was subjected to ultrasonic treatment in separate baths for 10 minutes each. This process was repeated up to 4 times per sample, totalling 40 minutes, with evaluations conducted at the end of each 10-minute interval to determine if a dispersed phase had formed.

The processing steps are outlined in the following Table (Tab. 11).

Table 11 Analysis of each sample in terms of improvements in the dispersion phase with respect to each operational stage.

	Step			
Sample	*1*	*2*	*3*	*4*
FG63	No discernible	Slight		
SBNa_03	No discernible	No discernible	No discernible	No discernible
SBNa_04	Slight	Significant		
SBNa_05	No discernible	No discernible	No discernible	No discernible

It indicates that the ultrasonic bath led to complete dispersion only for the "SBNa_04" sample and a slight improvement for the "FG63" sample. These conditions were achieved after the second immersion, thus totalling 20 minutes. However, the other samples did not show improvements even after the fourth immersion step. Even subsequent immersion in the ultrasonic tip for 3 minutes did not mitigate the absence of precipitation. Concurrent immersion of the samples in the ultrasonic bath for the instrument's maximum time of 100 minutes, as the final ultrasonic operation, did not yield improvements.

Therefore, at the end of the second step, the following observations were made:

- SBNa_04: Complete dispersion achieved.
- FG63: Slight dispersion, but not complete.
- SBNa_03, SBNa_05: Dispersion did not occur.

Considering the obtained conditions, a third dispersion attempt was carried out, with the focus on the presence of a counterion solution. A 0.1 M aqueous solution of KNO3 was prepared with a volume of 35ml. Since the necessary quantity of counterion solution for the dispersion of each sample was unknown, the solution was added gradually to each sample, promoting dispersion using a high-speed agitator. The amounts of counterion solution added to each sample are shown in the following Tab. 12; note that the "SBNa_04" sample is not included as dispersion had already been achieved earlier.

Table 12 Additions of counterion solution (µl), referenced to the number of additions for each sample.

	Step								
Sample	*1*	*2*	*3*	*4*	*5*	*6*	*7*	*8*	*Total*
FG63	15	15	15	15	20	/	/	/	80
SBNa_03	40	40	40	30	50	/	/	/	200
SBNa_05	20	20	20	30	30	30	40	20	210

During the execution of this procedure, the following observations were made:

- The "FG63" sample reached complete dispersion after adding VT=80 µl of counterion solution.
- The "SBNa_03" sample showed slight improvements, but they weren't significant enough to warrant further addition of counterion solution. This led to the decision to halt the addition at a total volume of 200 µl.
- The "SBNa_05" sample indicated the potential for dispersion after the initial attempts. Similar to "SBNa_03," it formed precipitates, yet the rate of particle sedimentation was much slower than the previous sample. Adding defined quantities of counterion solution showed slight improvements, but precipitation still occurred.

At the end of the procedure, all analysed samples were subjected to ultrasonic treatment for t=20 minutes, resulting in complete dispersion for the "SBNa_05" sample as well. However, the "SBNa_03" sample still exhibited precipitates.

The fourth and final attempt focused solely on the "SBNa_03" sample. Due to doubts about the correctness of the grinding process (post-synthesis), the powder was re-ground, and then 10 mg of powder were added to the 0.1 M solution. Despite the notably high volume of solution, the use of a high-speed agitator quickly achieved the absence of precipitates at the bottom.

The DLS analysis was conducted following the successful dispersion of powders. As detailed in Chapter 3, this analysis provided the hydrodynamic radius of particles. The upcoming evaluations will particularly consider the values of the "Z-Ave" and "PdI" parameters. Three

measurements were taken for each sample, and the intensity vs. particle diameter trends will be represented (Fig. 26,27,28,29), along with the obtained parameter values (Table 13, 14,15, 16).

- “FG63”

The specifics of the analysis conducted on the "FG63" sample are presented in Fig. 26 and in Tab. 13.

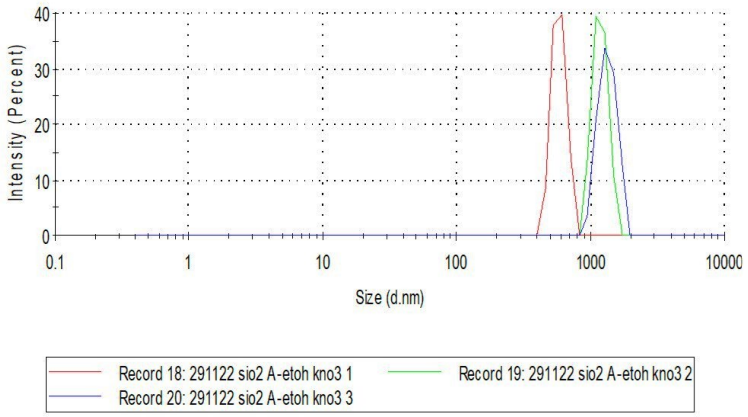

Figure 52 Size distribution by intensity-sample "FG63"

Table 13 DLS results-sample "FG63"

Type	Sample Name	Measurement Date	T	Z-Ave	PdI	Attenuator
			°C	*d.nm*		
Size	291122 sio2 A-etoh kno3 1	Tuesday 29th November 2022	20	1516	1	9
Size	291122 sio2 A-etoh kno3 2	Tuesday 29th November 2022	20	2231	1	9
Size	291122 sio2 A-etoh kno3 3	Tuesday 29th November 2022	20	3079	0,524	9

From the initial measurement within the series of three performed, it becomes readily apparent that the powder manifests a diameter at the micrometre scale. In contrast, the results of the third measurement present diminished values. This outcome stems from the assessment

of the smallest particles persisting in solution precisely at the juncture when the precipitation of the larger constituents is deemed to have transpired.

- “SBNa_03”

The specifics of the analysis conducted on the "SBNa_03" sample are presented in Fig. 27 and Tab. 14.

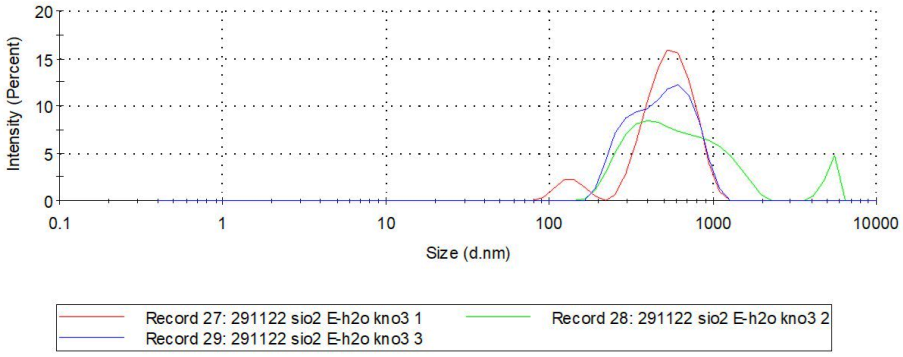

Figure 53 Figure 21 Size distribution by intensity-sample "SBNa_03"

Table 204 DLS results-sample "SBNa_03"

Type	Sample Name	Measurement Date	T	Z-Ave	PdI	Attenuator
			°C	*d.nm*		
Size	291122 sio2 E-h2o kno3 1	tuesday 29th November 2022	20	661,1	0,587	10
Size	291122 sio2 E-h2o kno3 2	tuesday 29th November 2022	20	694,1	0,481	10
Size	291122 sio2 E-h2o kno3 3	tuesday 29th November 2022	20	693,7	0,575	10

The solution reveals a submicron-scale radius value (approximately 690nm); however, it's imperative to approach this value with caution. The attained dispersion was made possible through the incorporation of a counterion solution, which, in the case of this study, comprises KNO3. This counterion solution functions by neutralizing the charged particles within the

dispersion. Consequently, the mutual repulsion among particles is diminished, facilitating their more uniform distribution.

This transformation leads to a shift in how particles interact with the solvent molecules, thereby influencing their effective size during analysis. Consequently, the system evaluates the hydrodynamic radius of particles rather than their actual physical radius.

- “SBNa_04”

The specifics of the analysis conducted on the "SBNa_04" sample are presented in Fig. 28 and Tab. 15.

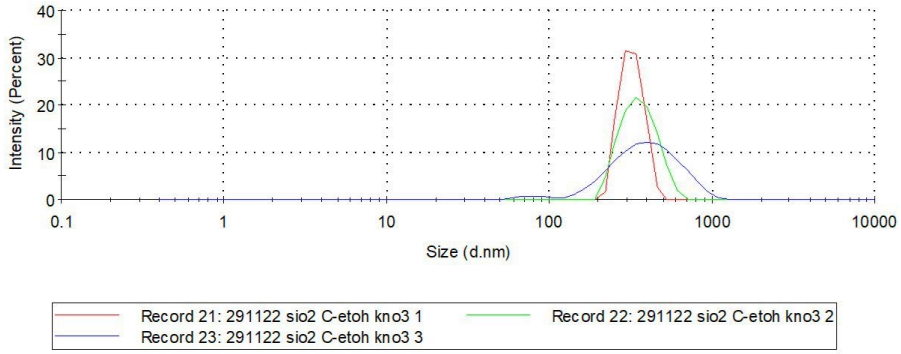

Figure 54 Size distribution by intensity-sample "SBNa_04"

Table 15 DLS results-sample "SBNa_04"

Type	Sample Name	Measurement Date	T	Z-Ave	PdI	Attenuator
			°C	*d.nm*		
Size	291122 sio2 C-etoh kno3 1	tuesday 29th November 2022	20	304,5	0,09	8
Size	291122 sio2 C-etoh kno3 2	tuesday 29th November 2022	20	346,1	0,011	8
Size	291122 sio2 C-etoh kno3 3	Tuesday 29th November 2022	20	337,6	0,198	8

The value of PDI is notably lower, in fact, it's the lowest among all the solutions, in comparison to sample “FG63”. It can be reasonably inferred that a few particles might

undergo precipitation during the measurement process. However, their scarcity is such that the system is able to accurately measure their diameters. This outcome reaffirms the observation stated earlier.

- "SBNa_05"

The specifics of the analysis conducted on the "SBNa_05" sample are presented in Fig. 29 and in Tab. 16.

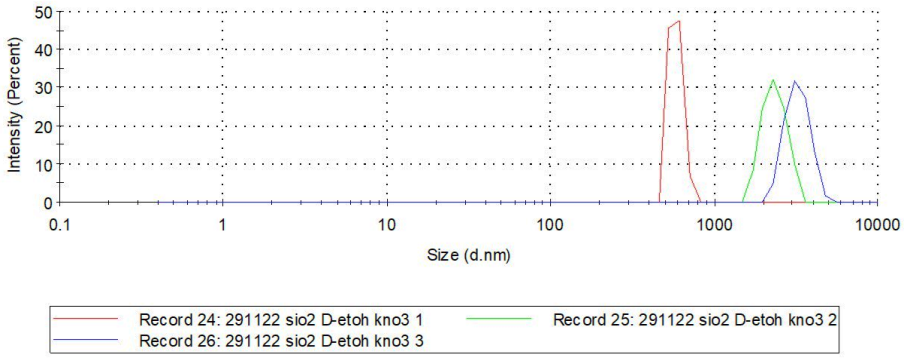

Figure 55 Size distribution by intensity-sample "SBNa_05"

Table 16 DLS results-sample "SBNa_05"

Type	Sample Name	Measurement Date	T	Z-Ave	PdI	Attenuator
			°C	*d.nm*		
Size	291122 sio2 D-etoh kno3 1	tuesday 29th November 2022	20	1005	0,715	9
Size	291122 sio2 D-etoh kno3 2	tuesday 29th November 2022	20	2356	0,044	9
Size	291122 sio2 D-etoh kno3 3	tuesday 29th November 2022	20	3003	0,326	9

The DLS analysis for the "SBNa_05" sample yields outcomes like those obtained for the "SBNa_03" sample. However, due to the application of a larger quantity of counterion solution (totalling 210 ml), the measured hydrodynamic diameter value emerges as the highest among the preceding samples, approximately 2 µm.

In summary, a slight comparison between the results obtained through DLS analysis and SEM analysis is possible, despite the intrinsic differences between the two measurements. As understood, DLS analysis involves a prior step of particle dispersion with the addition of a counterion solution, thereby evaluating the hydrodynamic diameter, which takes into account the layer of solvation molecules and counterions.

However, for the "SBNa_04" sample, dispersion was achieved without the addition of the counterion solution, and consequently, the results of the DLS analysis are approximately similar to those of the SEM analysis. In particular, the diameter value was measured at around 330 nm.

6.2.2.5 TGA/DSC

In the context of the DSC-TGA analysis conducted within the scope of this research, the results have been presented in Fig. 30.

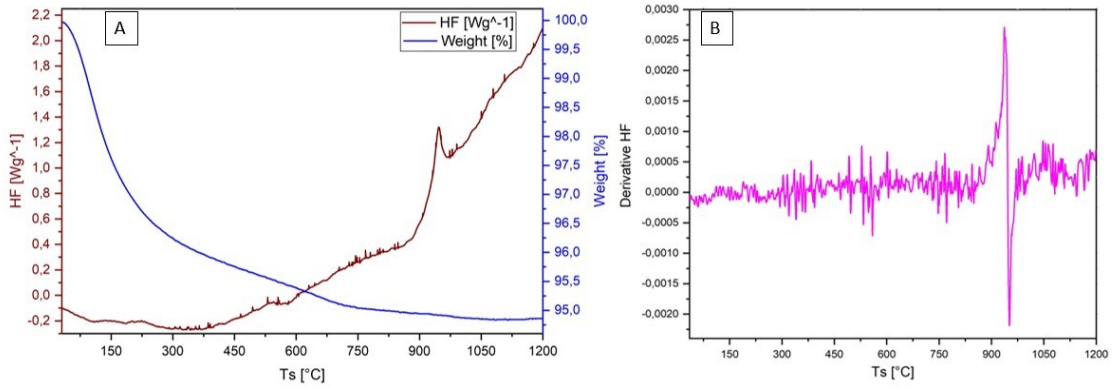

Figure 56 DSC-TGA analysis; (A)DSC/TGA curve, (B) Derivative HF curve-sample "SSrCa_01"

This figure (A) clearly illustrates the TGA curves in green and DSC curves in purple, showing a significant correlation between them. The TGA curve highlights two notable changes in slope: the first occurring at around 150°C, followed by a second at 750°C. It is highly likely

that these changes in slope are related to the removal of water and organic compounds present in the analysed powders.

However, the DSC analysis reveals a distinctive endothermic peak at approximately 980°C, indicating energy absorption associated with a chemical reaction that requires further investigation for precise characterization. To delve deeper into the nature of this peak, Fig. 30 (B) presents the derivative of the DSC with respect to temperature. It is important to note that despite the lack of a clear pattern in the data points on the graph, a significant peak persists at 980°C.

Considering that peaks in the DSC derivative correspond to temperatures where significant thermal transitions occur, it is reasonable to suggest that the temperature of 980°C represents the glass transition temperature of the analysed powders. However, it should be emphasized that this transition temperature is considerably high, suggesting that the powders may have a glass transition temperature lower than that of common silicate glass but still too high to enable a cold sintering process that would result in the formation of a transparent glass. This observation is of paramount importance for the design of future manufacturing processes and applications related to the studied powders in the field of engineering.

6.3 Production of compacted powder pellets

A fundamental phase of this research involves the investigation into the fabrication of pellets using select particle types produced earlier. This section will outline the manufacturing methodology employed for pellet production, detailing the procedures followed. Subsequently, a series of thermal treatments will be administered to the pellets, aimed at elucidating the impact of these processes on their composition and structure. The thermal treatments will be meticulously executed, and their effects will be rigorously monitored. Following the thermal treatments, a visual evaluation of the resulting pellets will be conducted to garner qualitative insights. This visual analysis will encompass observations of colour, surface texture, and potential alterations in physical integrity. The observations from this visual assessment, coupled with the data collected from the

characterizations and thermal treatments, will collectively contribute to a comprehensive understanding of the interplay between particle properties, pellet manufacturing, and thermal processing. The conclusions drawn from this phase of the research will provide valuable insights into the optimization and design of particle-based pellets for various applications.

6.3.1 Experimental work

The process of compacted pellets formation involved the following steps:

- Preparation of press and mould: the "WP-1 Pressing die set, Across International" press was set up for pellet formation. The mould's characteristics, as well as those of the press, were in accordance with the details outlined in Chapter 3, Section 3.1.1.1 of the thesis.
- Weighing and loading: a fixed mass of powder, measuring 0.3550g, was accurately weighed and loaded into the mould cavity.
- Application of force: a pressing force of 10 tons (approximately 200 MPa) was applied to the powder within the mould cavity. This force was generated by the press's mechanical system and was designed to compact the powder particles into a solid pellet.
- Dwell time: the pressing force was maintained for a dwell time of 20 seconds. During this period, the particles were subjected to the applied pressure, allowing for particle rearrangement and compaction.
- Pressure release and pellet extraction: after the dwell time elapsed, the applied pressure was released. The pellet, now formed and compacted, was gently extracted from the mould.
- Storage: The extracted pellet was placed in a container at atmospheric pressure, ensuring that no external forces were acting on it.

It's important to emphasize that this pellet formation process did not involve the use of a heating ring or a temperature control system. The primary focus was on the mechanical compaction of the powder to create a pellet of the desired shape and size. This process aligns

with the specifics provided in the mentioned section of the thesis and contributes to the overall understanding of pellet manufacturing for the studied materials.

6.3.2 Thermal treatments

The decision was made to create compacted powder pellets using the following samples: "SiO2," "SB_01," and "SBNa_06," both in their dried state at 120°C and calcined state at 400°C. Following the pellet formation process mentioned earlier, the pellets were subjected to a thermal treatment under the following conditions: temperature T = 700°C, dwell time t = 1 hour, and a heating rate of 5°C/min.

The purpose of this thermal treatment was to induce changes in the pellets' microstructure, crystallinity, and other physical and chemical properties. The chosen conditions of temperature, dwell time, and heating rate were based on previous knowledge of the materials and the desired effects of the thermal treatment.

Subsequently, the effect of the thermal treatment on the pellet formed from nanostructured silica powder is presented in Fig. 31. The nanostructured silica powder was produced using the well-established Stöber synthesis process.

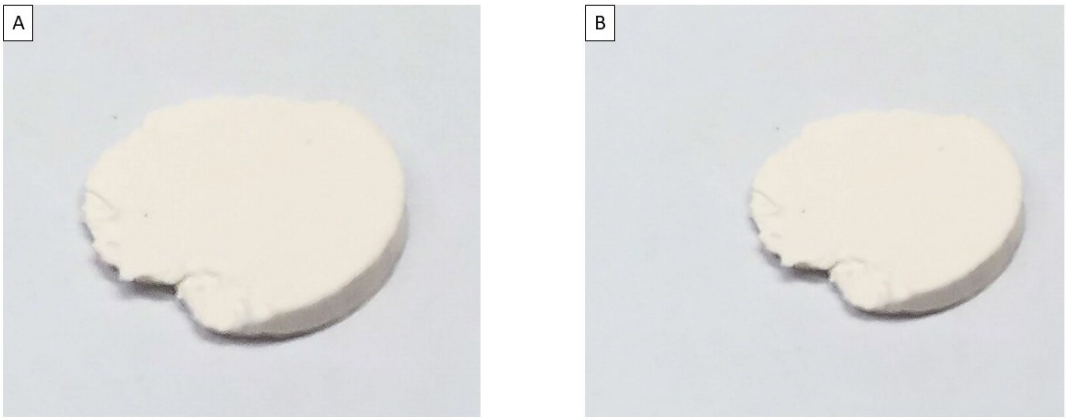

Figure 57 "SiO2" pellets before (A) and after (B) thermal treatment

The pure silica pellet, developed as a reference, exhibits no discernible variation before and after the thermal treatment. This result is expected given that the pellet does not contain any

organic components. As a result, the pellet retains its white colour, corresponding to the colour of the initially produced silica powder. Furthermore, no structural changes, such as phase transitions, were observed as initially hypothesized. This can be attributed to the fact that the temperature at which the thermal treatment was conducted is below the glass transition temperature of silica.

The sample "SB_01," composed of white powder, undergoes a notable change in colour following the described procedures, resulting in a pellet with a pink-brown hue. This colour transformation is likely due to the presence of organic compounds originating from the triethyl borate precursor used in the synthesis process. As illustrated in Fig. 32, the thermal treatment brings about a change in the pellet's colour. However, it's important to note that the pellet itself remains physically intact, and no alteration in shape or form is observed.

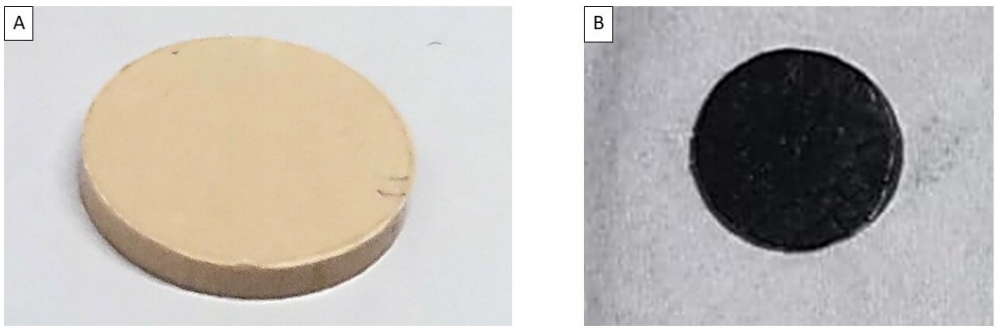

Figure 58 "SB_01" pellets before (A) and after (B) thermal treatment

The colour change can be attributed to the interaction between the organic compounds present in the sample and the elevated temperature during the treatment. The thermal energy might trigger reactions or decomposition of these compounds, leading to the observed change in colour. Otherwise, the observed change in colour is likely attributed not only to the interaction of organic compounds but also to the phenomenon of carbonization. The operating temperature may have induced the carbonization of organic molecules present in the "SB_01" sample. The elevated temperature could promote chemical reactions that result in the formation of carbonaceous structures, leading to the change in colour from white to the distinct pink-brown shade.

It's worth noting that despite the pronounced alteration in colour, the pellet's shape remains unchanged, and there is no discernible transformation of the material's phase. This outcome is likely since the operating temperature is below the glass transition temperature (Tg) of a borosilicate, a class to which the powders of this sample belong. The relatively low temperature applied during the thermal treatment appears to be insufficient to induce significant structural rearrangements or phase transitions in the material.

Distinctive changes are observed with the "SBNa_06" sample powders. As outlined in Section LL of the current chapter, a portion of the particles underwent drying at 120°C for 30 minutes, while another portion was first dried at 60°C for 48 hours and subsequently calcined at 400°C for 10 minutes. The pellet formed from the powder subjected to drying only, as illustrated in Fig.33 , exhibits an amber colour. This tint closely resembles the colour of the sodium precursor (sodium ethoxide) used. This suggests that despite the white colour of the powder, the compaction process accentuates the presence of organic components, leading to the observed coloration.

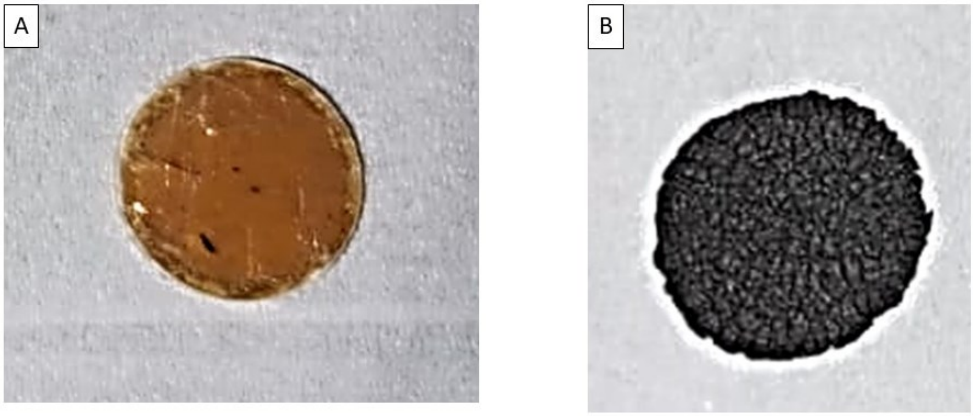

Figure 59 "SBNa_06" dried at T=120°C pellets before (A) and after (B) thermal treatment

Following the thermal treatment, the pellet not only exhibits a black colour, indicative of evident organic carbonization, but it also displays a peculiar bloating phenomenon. This swelling is of uncertain interpretation and raises questions about the underlying mechanisms at play.

The contrasting behaviour of the "SBNa_06" samples before and after the thermal treatment provides an insight into the interaction between organic components and temperature. The initial colour change upon compaction highlights the sensitivity of organic materials to mechanical stress during pellet formation, influencing the visual appearance of the material. Subsequently, the carbonization observed after the thermal treatment further underscores the reactivity of the organic compounds to elevated temperatures. The bloating phenomenon within the pellet following the thermal treatment requires careful consideration and investigation. It could be attributed to the release of gases or volatile compounds due to the organic decomposition, or it might involve structural changes resulting from the thermal stresses introduced during the treatment.

Slightly different behaviour is exhibited by the pellet formed from the "SBNa_06" powder subjected to calcination at 400°C. As illustrated in Fig. 34, the pellet before the thermal treatment displays the same characteristics as the corresponding dried powder. However, a notable change occurs as the pellet transforms into a grey-green colour after the treatment.

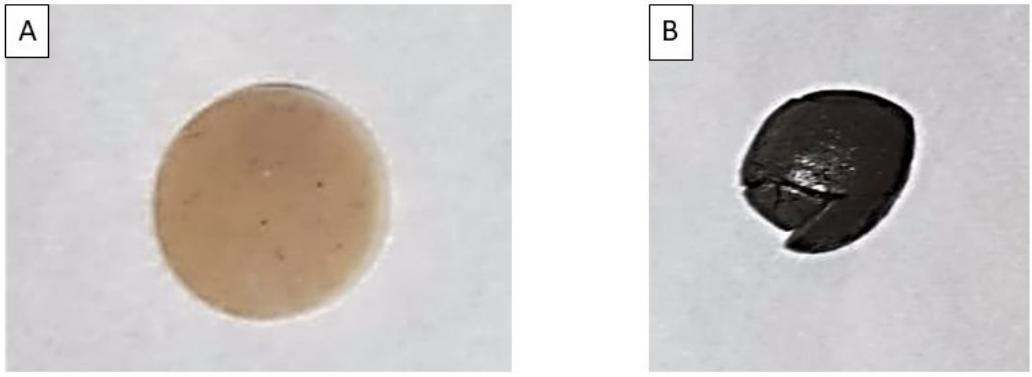

Figure 60 "SBNa_06" calcinated at T=400°C pellets before (A) and after (B) thermal treatment

The pretreatment of the powder at 400°C resulted in a removal of the organic content. The presence of the dark colour, however, indicates that the removal of organic material is not complete, suggesting that the applied calcination treatment was insufficient to eliminate all organics.

Interestingly, despite the incomplete removal of organic material, the dark coloration suggests that some carbonaceous compounds remain. This phenomenon underscores the intricate nature of thermal processes and the various chemical interactions occurring during treatment. A particularly striking aspect is the pronounced swelling or bloating effect observed, surpassing the degree observed in the previous sample. This swelling is accompanied by the formation of fractures within the pellet structure. This outcome might indicate that the thermal treatment caused significant gas evolution from the organic components, leading to internal pressures that exceeded the pellet's structural integrity. The points of fracture likely represent regions where this pressure was concentrated, resulting in visible ruptures.

6.3 Conclusions

In conclusion, this chapter has provided a detailed overview of the synthesis of low glass transition temperature (Tg) glassy nanoparticles through a sol-gel process based on the Stober method, with some specific modifications aimed at lowering the glass transition temperature. However, the detailed analysis has revealed significant challenges in obtaining ideal glassy nanoparticles for cold sintering.

The modifications made to the synthesis process, including the addition of oxide precursors to lower the glass transition temperature, did not result in the formation of a well-defined network between the oxides, which could have further reduced the glass transition temperature. Furthermore, despite the particle sizes being in the range of hundreds of nanometres, the removal of residual organic material proved to be problematic, as evidenced by the formation of dark powder pellets after calcination.

In summary, this research phase has highlighted two main challenges that require further investigation and development: the need to create a stronger connection between the oxides within the nanoparticles to achieve a sufficiently low glass transition temperature and the

need to develop a more effective organic removal process. These obstacles must be overcome before considering the practical application of low Tg glassy nanoparticles in cold sintering.

CHAPTER 7

Conclusions

The research conducted led to the development of new glass production methodologies by unconventional sintering approaches. Specifically, three different strategies were explored: cold sintering of commercial borosilicate glass particles, Spark Plasma Sintering on nanostructured silica, and the chemical synthesis nanoparticles at low glass transition temperature.

The examined commercial glass particles have a glass transition temperature of 480°C and tend to form agglomerates with sizes around 1260 nm, with flakes having an average diameter of 530 nm. The cold sintering process was systematically tested to assess key parameters, including powder mass, liquid phase molarity, liquid-to-mass ratio, pressure, temperature, and powder dwell time in the mould. Characterization of the samples provided insights into the effects of temperature and liquid-to-solid ratio. SEM analysis on samples with relative density closest to the theoretical density of borosilicate glass revealed that sample produced using a solution with a molarity of 2M, with a liquid phase representing 28% of the total powder mass, temperature of 200°C for a duration of 15 minutes exhibited the lowest porosity and the best compaction. In contrast, the sample produced using a solution with a molarity of 15M, with a liquid phase representing 14% of the total powder mass, temperature of 200°C for a duration of 120 minutes achieved the lowest densification, resulting in a layered structure with horizontal cracks, likely due to a reduced liquid-to-solid ratio. This provided enough liquid for sintering between particles but not for complete compaction. Crack formation might also relate to pellet compaction or extraction methods.

Temperature played a crucial role in the sintering process. The sample sintered at 250°C (with a solution molarity of 15M, liquid phase representing 14% of the total powder mass) potentially led to bubble formation due to increased exothermic reactions and the release of trapped vapor within the matrix. In conclusion, from the development of the cold sintering

process, well-defined considerations emerge regarding various parameters, but the need for further in-depth studies on the influence of temperature is evident. As observed, even a variation of only 50°C has a significant impact on the internal structure of the produced pellet, emphasizing the need for a more detailed analysis to determine the best combination of parameters and the optimal temperature value.

The development of the Spark Plasma process conducted on borosilicate glass particles has revealed another critical influence to consider, namely, pressure. This process was conducted while keeping the dwell time constant (3 minutes) and at a temperature slightly below the glass transition temperature (450°C). It was observed that an increase in pressure promotes greater densification and the formation of translucent pellets. For instance, by increasing the pressure from 1 GPa to 1.5 GPa, a relative density of 96.23% was achieved. However, it's important to note that density measurements and process' in-situ measurements indicated an incomplete densification. Since sintering is the result of a complex interplay of parameters, the results obtained through the Spark Plasma process provide a solid foundation for further research aimed at better understanding the influence of temperature and dwell time. These factors are clearly crucial for refining the sintering process and represent a critical area of study for future developments.

Silica particles, with a diameter of 7 nm at room temperature (25°C), underwent a heat treatment at 900°C, resulting in a 23.05% weight loss due to the removal of adsorbed water and carbon dioxide from the surface, along with an increase in particle size. Characterization analysis conducted immediately after the calcination process revealed that a heat treatment of 1000°C on particles would lead to a phase change with the formation of quartz, losing the characteristic amorphous structure of glassy materials. Silica particles, so pre-treated at 900°C, were subjected to Spark Plasma Sintering (SPS), with constant pressure and dwell time at 2 GPa and 3 minutes, respectively. By varying the process temperature from 1000°C to 800°C, transparent areas began to be observed; The sintering process wasn't fully completed for both samples. While the Archimedes test yielded a relative density of 99.39%, its accuracy may be compromised due to the difficulty of completely removing graphite along the pellet's cylindrical walls, given its extreme fragility.

Another significant observation to emphasize is that increasing the temperature to 1000°C not only failed to achieve transparent areas but also induced the formation of surface crystallites. These crystallites were identified as alpha-cristobalite through spectroscopic analysis.

The discussion highlights two key points: Crystallization occurs at lower temperatures due to the combined effect of pressure and the smaller particle size (as confirmed in [*127*]), and the potential to attain transparency at temperatures about 300°C lower than traditional silica glass production temperatures is a significant discovery. This result confirms the potential for developing unconventional sintering processes for glass production, contributing to a more efficient use of energy and resources. Particle size has proven to be an extremely key factor in the context of the Spark Plasma Sintering process, highlighting distinct results between borosilicate glass and silica glass, which differ not only in chemical composition but also in the particle sizes constituting the powder subjected to treatment. Since the densification process is based on diffusive mechanisms, it becomes clear that they are more efficient when particle sizes are reduced to a few nanometres, as observed in the case of treated silica, rather than when dealing with particle sizes of hundreds of nanometres, as in the examined borosilicate glass. Consequently, keeping this fundamental consideration in mind for unconventional sintering mechanisms, the next objective is to initially produce nanostructured glass particles, with particular attention to achieving the lowest possible glass transition temperature.

In this context, the research has developed chemical synthesis strategies. Starting from the Stober process model, modifications were made to the chemical synthesis to allow the addition of oxide precursors capable of lowering the glass transition temperature. However, the particles thus produced, while characterized for their composition, chemical structure, and dimensions, showed a lack of internal connectivity between the oxides, that is essential for reducing the glass transition temperature. At the same time, challenges were encountered in removing the organic agents present in the particles. Therefore, in the future, it will be necessary to address the challenges related to these aspects, attempting to overcome the

problem of the lack of an internal network structure between the oxides and developing an effective process for the removal of organic agents.

In conclusion, the experimental work conducted has laid a solid foundation for glass production through unconventional sintering approaches, demonstrating not only the feasibility of such processes but also outlining some of their fundamental characteristics. However, this work also presents important challenges, including overcoming obstacles in the chemical synthesis of low glass transition temperature glass nanoparticles and identifying the optimal combination of parameters for cold sintering and Spark Plasma processes, with a particular emphasis on temperature control, an aspect that requires further optimization.

BIBLIOGRAPHY

[1]. S. Funahashi, J. Guo et al. – J. Am. Ceramic Society 100 (2017), 546-553

[2]. M. Kindelmann, J. N. Ebert et al.; Scripta Materialia 224 (2023), 115147

[3]. H. Guo, A. Baker et al. – ACS Nano 10 (2016), 10606-10614

[4]. L. Karacasulu, E. Ogur, et al. - Scripta Materialia 192 (2021), 111–114

[5]. B. Santhosh, A. Galotta et al. - Ceramic International 48 (2022), 35627–35632

[6]. TsujiKe WangSun Hwi BangClive et al. - Journal of the European Ceramic Society 39 (2019), 4743-4751

[7]. Z. Lin, X. Zhao et al. - Small 18 (2018) , 2107951

[8]. E. D. Zanotto – Am. H. Phys. 66 (1998)

[9]. U. R. Sumanasekara – PhD thesis "Effect of cation symmetry on probe rotational diffusion in ionic liquid studied by fluorescence recovery after photobleaching".

[10]. W. H. Zachariasen - J. Am. Chemical Society 54 (1932), 3841–3851

[11]. Kingery, W. D., Bowen et al. – D. R. (1976), "Introduction to Ceramics"

[12]. Deschamps T. – PhD thesis "Etude des déformations élastique et plastique des verres de silice et sodo-calcique sous hautes pressions hydrostatiques et indentation par spectrométrie Raman", University of Lyon I (2009)

[13]. Deschamps T. – PhD thesis "Etude des déformations élastique et plastique des verres de silice et sodo-calcique sous hautes pressions hydrostatiques et indentation par spectrométrie Raman", University of Lyon I (2009)

[14]. G. Shao, X. Hu et al. - Surface and Coatings Technology 270 (2015), 154-163

[15]. C. Lonergan, J. Neeway, Environmental Science (2017)

[16]. B. Champagnon, C. Martinet et al. – J. Non-Crystalline Solids 354 (2008), 569

[17]. V. Martinez, C. Martinet et al. - J. Am. Ceram. Soc., 89 (2006), 596–601

[18]. C. Sonneville, A. Mermet et al. – J. Non-Crystalline Solids 382 (2013), 133–136

[19]. G. N. Greaves, A. L. Greer et al. - Nature Materials (2011) 10, 823–837

[20]. G.E.Walrafen, P. N. Krishnan - J. Chem. Phys. 74 (1981), 5328 (1981)

[21]. A. Polian A, M. Grimsditch - Phys. Rev. B 41 (1990) , 6086

[22]. R. G. Della Valle, E. Venuti - Phys. Rev. B 54 (1996), 3809
[23]. Bridgman P. and I. Simon - J Appl Phys 24 (1953), 405
[24]. R. J. Hemley, H. K. Mao et al. - Phys. Rev. Lett. 57 (1986), 747
[25]. J. S. Tse, D. Kug et al. - Phys. Rev. B 46 (1992), 5933
[26]. T. Rouxel, T. Hammouda et al. - Phys. Rev. Lett. 100 (2008), 225501
[27]. T. Deschamps, C. Martinet et al. - J. Non-Cryst. Solids 355 (2009), 2422 (2009)
[28]. T. Deschamps., C. Martinet et al. - J. Non-Cryst. Solids 355 (2009), 1095
[29]. H. Sugiura, R. Ikeda et al. - J. Appl. Phys. 81 (1997), 1651
[30]. W. J. Chan, T. Huser et al. - Optics Letters 26, 1726 (2001).
[31]. T. J. Rouxel, C. Moysan et al. - J. Non-Cryst. Solids, 344, 26 (2004)
[32]. T. Rouxel, H. Ji et al. - Phys. Rev. Lett. 100, 225501 (2008).
[33]. B. Champagnon, C. Martinet et al. - J. of Non-Cryst. Solids 354, 569 (2008).
[34]. M. Grimsditch - Phys. Rev. Lett. 52, 2397 (1984).
[35]. A. Polian, M. Grimsditch - Phys. Rev. B 41, 6086 (1990)
[36]. J. Neely, J. Mackenzie - J. Mater Sci, 6, 603 (1968).
[37]. K. Peter - J. Non-Cryst Solids, 5, 103 (1970)
[38]. A. Arora, D. Marshall et al. - J. Non-Cryst Solids, 31, 415 (1979).
[39]. University of Rome “La Sapienza” – “Complementi di Fisica Generale: XXI Lezione”
[40]. University of Rome “La Sapienza” - Complementi di Fisica Generale: XXII Lezione
[41]. P. Colombo - Glass science and technology, University of Padua
[42]. P. Colombo - Glass science and technology, University of Padua
[43]. C.L. Cramer – PhD thesis “Applications and advanced sintering techniques of functionally graded ZnO-based thermoelectric material”.
[44]. Exner H E Freund Publishing House, Israel 1 (1979), 1–4
[45]. Exner H E Freund Publishing House, Israel 1 (1979), 1–4
[46]. Johnson D L - Processing of Crystalline Ceramics. Plenum Press 1978
[47]. M.N. Rahaman - Sintering of Advanced Materials (2010), 33-64
[48]. M. Randall et al. – J. Mater. Sci. 4(2009),1–39
[49]. Johnson JL, German RM (2001) Metall Mater Trans 32A:605

[50]. M. Randall et al. - J Mater. Sci. 44 (2009), 1–39
[51]. C. Guyard, C.H. Allibert et al. - Sci Sin (1981), 13-149
[52]. F.J. Puckert, W.A. Kaysser - Metallkd (1983), 74-737
[53]. Ceramic – Unie, Ceramic roadmap to 2050
[54]. M. Biesuz, S. Grasso et al. - Current Opinion in Solid State and Materials Science 24 (2020), 100868
[55]. C. A. Randall, J. Guo et al. - Patent Application Publication (2018),US 2017/0088471 A1
[56]. C. A. Randall, J. Guo et al. - Patent Application Publication (2018),US 2017/0088471 A1
[57]. J. Maria, X. Kang et al. - J. Mater. Res. 32 (2017) 3205–3218
[58]. J. Guo, A.L. Baker et al. - J. Am. Ceram. Soc. 100 (2017), 669–677
[59]. J. Guo, R. Floyd et al. - Annu. Rev. Mater. Res. 49 (2019), 275–295
[60]. A. Galotta, V.M. Sglavo - Journal of the European Ceramic Society 41 (2021),, 1–17
[61]. A. Ndayishimiye, M.Y. Sengul et al. - Open Ceramics 2 (2020), 100019
[62]. J. P. Maria, X. Kang – Journal of Materials Research 32 (2018), 3205 - 3218
[63]. L.C. Zhu Jianga, T. Lu et al. - Appl. Energy 237 (2019), 367–377
[64]. T. Charoonsuk, U. Sukkha, T et al. - Ceram. Int. 44 (2018), S54–S5
[65]. S. Funahashi, J. Guo et al. - J Am Ceram Soc. 100 (2017), 546–553
[66]. H. Guo, A. Baker, J. Guo, C. A. Randall - ACS Nano 2016, 10, 10606−10614
[67]. L. Karacasulu, E. Ogur et al. - Scripta Materialia 192 (2021) 111–114
[68]. B. Santhosh, A. Galotta, et al. - Ceramic International (2022)
[69]. M. Cologna, B. Rashkova et al. - J. Am. Ceram. Soc. 93 (2010), 3556–3559.
[70]. S. Grasso - Advances In Applied Ceramics 116 (2017), 24–60
[71]. S. Grasso - Advances In Applied Ceramics 116 (2017), 24–60
[72]. S. Grasso, Y. Sakka et al. – Sci. Technol. Adv Mater 10 (2009); 053001
[73]. J. Park, I. Chen – J. Am. Ceram. Soc. 96 (2013), 697–700
[74]. JSC Francis - University of Colorado at Boulder (2013)
[75]. RA Thomas - Coxmoor Publishing (1999)
[76]. S. Grasso - Advances In Applied Ceramics 116 (2017), 24–60

[77]. M. Hirokazu, K. Hiromi - Scientific Reports 12 (2022), 14761
[78]. Y. Le Godec, S. Le Floch – Materials 16 (2023), 997
[79]. D. Vallauri et al - Int. J. Refract. Met. Hard Mater. 27 (2009), 996–1003
[80]. M. Tokita- Proc. NEDO Int. Symp. Functionally Graded Materials, Kyoto, Japan, (1999)
[81]. Y.C. Wang et al., Key Engineering Materials 249 (2003), 471
[82]. G. Bernard-Granger et al.; Acta Mater. 58 (2010), 3390-3399
[83]. Institut Carnot-Chimie Balard Cirimat
[84]. S. Grasso et al. – Advanced Materials 17 (2005), 1261
[85]. J. Zhang, R. Tou et al.- Ceramics International 38 (2021) 2673-2678
[86]. H. Masai, Scientifc Reports (2022) 1214761
[87]. T. G. Mayerhofer, Z. Shen et al.- Journal of Solid State Chemistry 181 (2008) 2442-2447
[88]. Y. Le Godec, S. Le Floch – Materials 16 (2023), 997
[89]. Deschamps T. – PhD thesis "Etude des déformations élastique et plastique des verres de silice et sodo-calcique sous hautes pressions hydrostatiques et indentation par spectrométrie Raman", University of Lyon I (2009)
[90]. C. Coussa-Simon – PhD thesis "Etude du verre d'oxydes LBG : des propriétés optiques non linéaires au comportement sous haute pression", University of Lyon 1 (2008).
[91]. J. G. Piermarini, S. Block et al. J. Appl. Phys. 46 (1975), 2774
[92]. C.V. Raman - Indian. J. Phys. 2 (1928), 387
[93]. Y. Zhang. D Li, Richard et al. – Electrochemistry communications 121 (2020), 106867
[94]. A. A. Vertegel et al. – Langmuir 20 (2004), 6800
[95]. H. T. Rana et al. - Materials, Interfaces and Electrochemical Phenomena (2005)
[96]. C. Coussa-Simon – PhD thesis "Etude du verre d'oxydes LBG : des propriétés optiques non linéaires au comportement sous haute pression", University of Lyon 1 (2008).
[97]. M. Chai, J. M. Brown - Geophysical research letters 23 (1996), 3539-3542

[98]. C. Sonneville, T. Deschamps et al. - Journal of Non-Crystalline Solids 382 (2013) 133–136

[99]. G. Gibbs; V. Boisen – Materials Research Society Symposia Proceedings 121, 155-165

[100]. C. Sonneville, T. Deschamps et al. - Journal of Non-Crystalline Solids 382 (2013) 133–136

[101]. K. Sehegal, S. ito - Journal of Non-Crystalline Solids 253 (1999), 126-132

[102]. P. Richet, A. Whittington et al. - Contrib Mineral Petrol 138 (2000), 337 - 347

[103]. B. Bates - J. Chem. Phys. 57, 4042–4047 (1972)

[104]. H. Aguiar, J. Serra et al. - Journal of Non-Crystalline Solids 355 (2009) 475–480

[105]. F. Angeli, Olivier Villain, Phys. Rev. B 85 (2012), 054110

[106]. H. Manghnani, A. Hushur et al. – J. Applied Physics 109 (2011), 11350

[107]. Y Zhou, J Zhang et al. - Journal of Non-Crystalline Solids (2021)

[108]. G. Gouadec et al. – Journal of the European Ceramic Society 25 (2005), 1447-1453

[109]. KS Rao, K El-Hami, T Kodaki et al. - Journal of colloid and Interface Synthesis 289 (2005), 125-131

[110]. D. V. Arole,. S. V. Munde - Materials Science (2014)

[111]. W. Stober, A. Fink - Journal Of Colloid And Interface Science 26 (1968), 62-69

[112]. E. Comini, G. Faglia et al. - Dordrecht (2008)

[113]. W. Stober, A. Fink - Journal Of Colloid And Interface Science 26 (1968), 62-69

[114]. K. Deshmukh, T. Kovariket al. - RCS Advanced, 2020

[115]. D. Paramelle et al. - Analyst, 2014, 139, 4855

[116]. X. Kesse, C. Vichery et al. - ACS Appl. Bio Mater. 3 (2020), 1312−1320

[117]. X. Kesse, C. Vichery et al. - ACS Appl. Bio Mater. 3 (2020), 1312−1320

[118]. R. M. Almeida et al. - The American Ceramic Society, (2021)

[119]. Francesco Grani – Master thesis “Nanoparticelle vetrose a bassa Tg”, University of Padua

[120]. E. Piatti, E. Vernè, M. Miola - Ceramics International 48 (2023) 13706–13718

[121]. C. Potremoli, I. Izquiedo Journal of Colloid and Interface Science 563 (2020) 92-103

[122]. Chemical Book - Sodium ethoxide(141-52-6) IR1

[123]. NIST – Borane, Ethyl

[124]. K. K. Ilavenil et al. - RASAYAN Journal of Chemistry 16 (2023),596-603

[125]. M. Khachani et al. - Journal of Materials and Environmental Sciences (2014), 615-624

[126]. L.R. Reva, E. Nugraha - Journal of Chemical and Pharmaceutical Research 7 (2015),85-89

[127]. S. Zhang, S. Tie et al - Micro & Nano Letters 13 (2018), 1465-1468

ACKNOWLEDGEMENTS

I would like to extend my heartfelt gratitude to Professor A. Martucci, my thesis supervisor, for his unwavering support throughout my academic journey. I am particularly grateful for his permission to conduct the experimentation in France and for his unwavering belief in the project.

My sincere appreciation goes to Dr. E. Colusso, whose indispensable guidance and exceptional availability were instrumental in the development and execution of the experimental work underlying this thesis.

I am also deeply indebted to Professor S. Le Floch for her invaluable mentorship during my time at the University of Lyon. Her assistance in accessing specific equipment and her insightful guidance were crucial in achieving promising results.

I wish to express my gratitude to the research team at the University of Lyon, namely Professors C. Martinet, A. Berthelot, V. Pischedda, T. Deschamps, and A. Diaf, for their dedicated efforts in facilitating the experimentation and for their warm hospitality and support during my stay in France.

I dedicate this work to my parents, as they have been my unwavering pillars of support. Their belief in me, even during challenging times, has been an invaluable source of inspiration and motivation.

A special acknowledgment goes to my "sister" Ilaria, whose presence has consistently been a source of joy and learning, contributing significantly to my personal growth and self-confidence.

I am grateful to all my friends who have supported me throughout this journey. To Ilaria V, Francesco, Federico, Olimpia, Maddy, Laura, Chiara C., Letizia, Alberto, Francesca, and Camilla, your unwavering support, especially during the recent period, has been invaluable. I also extend my thanks to my friends from Abruzzo, including Chiara D., Valeria, Domenico, Ilenia, and Enzo, for making me feel connected even when physically distant.

A special thank you goes to the friends I made in France, including the colleagues at the office on the 4th floor of the Brillouin building and Sana and Alessia, whose friendship was instrumental in making my time there not only culturally enriching but also personally fulfilling. I hope to see you all again soon.

Lastly, I am grateful to the scientific community for providing me with the opportunity to delve into the world of research and for instilling in me a passion for discovery. I sincerely hope that the research outlined in this thesis will contribute to a better understanding of glass materials and pave the way for future developments, as the saying goes, "Science is progress."

Best Regards,

Benedetta Matani